Università degli studi di Genova

Facoltà di Scienze M.F.N.

Istituto Italiano di Tecnologia

Nanoscopy & NIC@IIT

PhD Thesis

Study of Chromatin Organization by Circular Intensity Differential Scattering (CIDS)

Candidate: Riccardo Marongiu

Tutor:

Prof. Alberto Diaspro

Supervisor:

Dr. Aymeric Le Gratiet

Table of Contents

General Introduction

Light is an electromagnetic wave that is composed by electric and magnetic fields propagating through space and time. Light spectroscopy and microscopy are techniques that use the interaction of light with matter to probe a sample's properties. The main characteristics of the light wave that are used for this purpose are its intensity, direction, wavelength, phase and polarization. The main advantage of light probing in samples is its ability to obtain information from long distances and its mostly non-destructive properties, allowing to preserve a sample even after observation.

In the field of biophysics, the most widely diffused light-related technique to study samples at the microscopic level are based on fluorescence methods. In these techniques, the sample is marked with fluorophores, molecules specifically tailored to bind to the structures of interest. Light of an appropriate wavelength is then shined on the sample, stimulating the fluorescent emission of the markers at a wavelength higher than the one of absorption. Since the wavelength is different from the one shined on the sample, it can be separated thanks to specific dichroic filters, allowing to reconstruct the signal coming only from the structures of interest. The high specificity of fluorescence microscopy is thus one of the reasons for its prevalent use in biophysics.

Recently though, there has been a rising interest in the field of label-free imaging, which includes all techniques used to probe samples without the help of fluorescent markers. The reasons leading to this are:

- The preparation step required for fluorescence imaging, meaning specific fluorophores are needed to view the desired structures;
- the requirement of a space and trained person to perform the marking process;
- the possibility of human error or generally dependence on the operator's skill on the reproducibility of the marking process;
- The possibility that the presence of the markers will change the in-situ organization of the structures of interest;
- High light dose for generating the fluorescence optical signal, which can potentially damage the sample and create photobleaching.

Simple transmitted light intensity does not offer enough contrast to compete with the ability of fluorescence imaging to study structures in biological samples. For this reason, ways to enhance the label-free contrast are needed. In particular, polarization is a promising avenue in this respect. Polarization control can help in enhancing the contrast and information present in the sample and in particular can be sensitive to the physical structure of samples. For example, as

will be explained in the pages of this thesis, chiral objects can produce an important circular dichroism signal.

To describe polarization two main formalisms are used: Jones and Stokes-Mueller. The first one is older and is ideal to describe light in function of its physical characteristics, like the electric field, but works only in the case of purely deterministic polarization states, being unable to describe depolarization. For this reason, it's not the most suitable formalism to describe most biophysical system, which present strong depolarization properties. Stokes-Mueller formalism, on the other hand, is a more operative formalism, allowing to work on more easily measured quantities such as the light intensity to determine the polarization interaction.

Circular dichroism is the polarization phenomenon that we have chosen to use to study the chromatin system. Circular dichroism is the differential interaction of light polarized circular left or circular right with a sample. While usually the main component of the signal is due to absorption, it has been proven that a part of the signal is due to the differential scattering of the two polarization states. The scattering part of the signal is named Circular Intensity Differential Scattering (CIDS) and it has been proven to be sensitive to chiral structures like the ones present in chromatin. It is therefore a perfect candidate for the label-free study of chromatin organization and has in fact been used for this end in the past.

This thesis is divided in three chapters.

In chapter 1, the theory and state of the art for light and polarization will be presented. First of all an account of the physical description of light and its mathematical treatment with Maxwell's equations will be shown, followed by the description of polarization and the two main formalisms used to describe it: Jones formalism and Mueller-Stokes formalism. In the final part, a description of relevant applications of polarization spectroscopy and imaging will be presented, including biological applications.

In chapter 2, the focus will be put on the Circular Intensity Differential Scattering signal and in particular on its spectroscopic abilities in the single-point mode. The chapter will start with a description of CIDS theory and a discussion about its sensitivity to chiral structures and the optical resolution this methos is able to provide. To follow, our own homemade single-point CIDS setup will be presented, consisting in a mechanical rotation arm of the polarization analyzer block and we will characterize its optical performance. Dedicated applications for measuring the spectroscopic angular CIDS signature will be shown, ranging from the study of the effects of the concentration of the samples on the polarization rotation with known chiral carbohydrate aqueous solutions to chromatin inside isolated HEK cell nuclei. The final part of the chapter will be dedicated to Fourier imaging, which we have proposed as an alternative to obtain the spectroscopic angular information of CIDS without moving mechanical parts.

Chapter 3 will be dedicated to the imaging modality of CIDS study. We will first present an overview of CIDS imaging, including the state of the art of setups and applications. After this, the custom CIDS/confocal fluorescence multimodal microscope that I have built and utilized during

my thesis will be presented, along with the alignment and data treatment utilized. A description of our findings on chromatin organization in isolated fixed HEK cells will follow, demonstrating the potential of this technique and our implementation. In the last part, the union of CIDS imaging with expansion microscopy (ExM) in an approach we have named ExCIDS will be the focus. ExCIDS allows to obtain information on the sample at higher resolutions and most of all to isolate the nuclei with a less traumatic procedure than the centrifuge method previously utilized, possibly conserving the structure of chromatin more completely.

Chapter 1: Polarized light formalism and applications

Introduction

Light is an electromagnetic wave that has been studied for centuries by illustrious scientists such as I. Newton (1642-1726) and J. C. Maxwell (1831-1879). It can be modeled as an electric and magnetic field oscillating perpendicularly to each other in time and in space. Among the properties of a light wave, such as its intensity, frequency and direction of propagation, there is polarization, which describes the change of orientation of $\vec{E}$ in a plane perpendicular to the propagation of the wave over time. If $\vec{E}$ changes without a fixed pattern in time, in a non-deterministic way, then the wave will be defined as unpolarized, otherwise it will be considered polarized. The type of polarization is dependent on the exact way $\vec{E}$ changes over time and space: a fixed orientation in these two dimensions for example will mean a linearly polarized beam. When light interacts with a sample, it can change its polarization state due to the structure and characteristics of the interacting medium. From the effect of the interaction, linear and circular birefringence and dichroism of the object can be extracted. The part of light science that studies this kind of interaction is called polarimetry.

This chapter is divided in three parts. In the first part, a description of the basics of light formalism will be given, followed by a deeper description of polarization and the formalism needed to describe it. Matrix approaches to polarization modeling like Jones (for completely polarized light and ideal optical components) and Mueller-Stokes formalisms will be described. In particular, the ability of Mueller-Stokes formalism to describe depolarization makes it a powerful tool in biomedical studies as this effect is not negligible for organic samples.

In the second part, a description of polarimetric Mueller-Stokes measurement setups will be given, with all their components including the Polarization States Generator (PSG) and the Polarization States Analyzer (PSA).

Finally, in the third and final part of the chapter, a list of some of the different fields and some applications of polarimetry is presented, including polarimeters utilized for atmospheric sensing of particles, target detection, astronomy and the most relevant use for this thesis, biomedical imaging. Thanks to the ability of polarization to enhance contrast in samples of any kind, the applications of polarimetry are ever expanding.

Part 1: Light and polarization theory

1. Light propagation

Light can be described as an electromagnetic wave that is composed by an oscillating electric field and magnetic field whose vectors are reciprocally perpendicular and they are also perpendicular to the direction of propagation of the wave.

James C. Maxwell developed the formalism that is used to describe light waves [1]. In particular, the differential form of Maxwell's equations is as follows:

$$\nabla \times \vec{E}(\vec{r},t) = -\frac{\partial \vec{B}(\vec{r},t)}{\partial t}; \quad (1)$$

$$\nabla \times \vec{H}(\vec{r},t) = J(\vec{r},t) + \frac{\partial \vec{D}(\vec{r},t)}{\partial t}; \quad (2)$$

$$\nabla \times \vec{D}(\vec{r},t) = \rho(\vec{r},t); \quad (3)$$

$$\nabla \times \vec{B}(\vec{r},t) = 0; \quad (4)$$

Where $\vec{E}$ is the electric field, $\vec{D}$ is the electric displacement, $\vec{H}$ is the magnetic field, $\vec{B}$ is the magnetic flux density, J is the current density and ρ is the free charge density.
To solve these equations the so called constitutive relations, which take into account the properties of the propagating medium, are needed. In particular, for a vacuum the constitutive relations are as follows:

$$\vec{D} = \varepsilon_0 \vec{E}; \quad (5)$$

$$\vec{B} = \mu_0 \vec{H}; \quad (6)$$

Where ε_0 is the vacuum permittivity (8.85×10^{-12} Fm^{-1}) and μ_0 is the vacuum permeability (1.25×10^{-6} Hm^{-1}).
When considering a region of space filled with matter, the constitutive relations become then:

$$\vec{D} = \varepsilon_0 \vec{E} + \vec{P}; \tag{7}$$

$$\vec{B} = \mu_0 (\vec{H} + \vec{M}); \tag{8}$$

Where $\vec{P}$ is the polarization and $\vec{M}$ the magnetization of the material, representing the average electric and magnetic dipole moment inside the medium.
In a homogeneous linear medium the following equations are valid:

$$\vec{P} = \varepsilon_0 \chi_e \vec{E}; \tag{9}$$

$$\vec{M} = \chi_m \vec{H}; \tag{10}$$

Where χ_e and χ_m are the electric and magnetic susceptibility. χ_e is always positive, while χ_m can be both positive and negative. Utilizing these relations, we obtain

$$\vec{D} = \varepsilon_0 (1 + \chi_e) \vec{E} = \varepsilon \vec{E}; \tag{11}$$

$$\vec{B} = \mu_0 (1 + \chi_m) \vec{H} = \mu \vec{H}; \tag{12}$$

In these conditions and without any sources, Maxwell's equations become

$$\nabla \times \vec{E}(\vec{r}, t) = -\mu \frac{\partial \vec{H}(\vec{r}, t)}{\partial t}; \tag{13}$$

$$\nabla \times \vec{H}(\vec{r}, t) = \varepsilon \frac{\partial \vec{E}(\vec{r}, t)}{\partial t}; \tag{14}$$

$$\nabla \cdot \vec{E}(\vec{r}, t) = 0; \tag{15}$$

$$\nabla \cdot \vec{H}(\vec{r}, t) = 0; \tag{16}$$

With opportune substitutions, the following wave equation can be determined

$$\nabla^2 \times \vec{E} - \frac{1}{u^2}\frac{\partial^2 \vec{E}}{\partial t^2} = 0; \tag{17}$$

Where $u = (\mu\varepsilon)^{-1/2}$ is the speed of light in the medium that is being considered.
Plane waves are a solution to Maxwell's equations, which also dictate that the electric and magnetic fields have to be perpendicular to each other and they both have to be perpendicular to the direction of propagation of the wave. For this reason, when discussing polarization it's a convention to only consider the electric field, as the magnetic field's behavior is strictly connected to the first.

2. Light polarization

Polarization is the property of light that describes the temporal and spatial evolution of the electric field as the light wave propagates in the plane xy perpendicular to the propagation axis z. Considering a wave propagating in a vacuum along the z axis, the evolution of its electric field will be given by the following equations:

$$E = \begin{bmatrix} E_x(z,t) \\ E_y(z,t) \\ E_z(z,t) \end{bmatrix} = \begin{bmatrix} E_{0x}\cos\left(\omega t - \vec{k}z + \Phi_x\right) \\ E_{0y}\cos\left(\omega t - \vec{k}z + \Phi_y\right) \\ 0 \end{bmatrix}; \tag{18}$$

Where E_{0x} and E_{0y} are the amplitudes of the electric field in x and y, ω is the frequency, $\vec{k}$ is the wave vector (such that $\left|\vec{k}\right| = \frac{2\pi}{\lambda}$, where λ is the wavelength of light) and ϕ_x and ϕ_y are respectively the x and y phases.
By setting $z = 0$ (which corresponds to observing one plane along the z axis), eliminating the temporal dependence and combining the x and y components of $\vec{E}$, we obtain the following formula

$$\frac{E_x^2}{E_{0y}^2} + \frac{E_y^2}{E_{0y}^2} - \frac{2E_xE_y}{E_{0x}E_{0y}}cos\Phi = \sin^2\Phi\,; \tag{19}$$

here $\Phi = \Phi_x - \Phi_y$. This formula corresponds to the mathematical representation of an ellipse. In the general case, the projection of the electric field in the O_{xy} plane will take this form as shown in Figure 1.

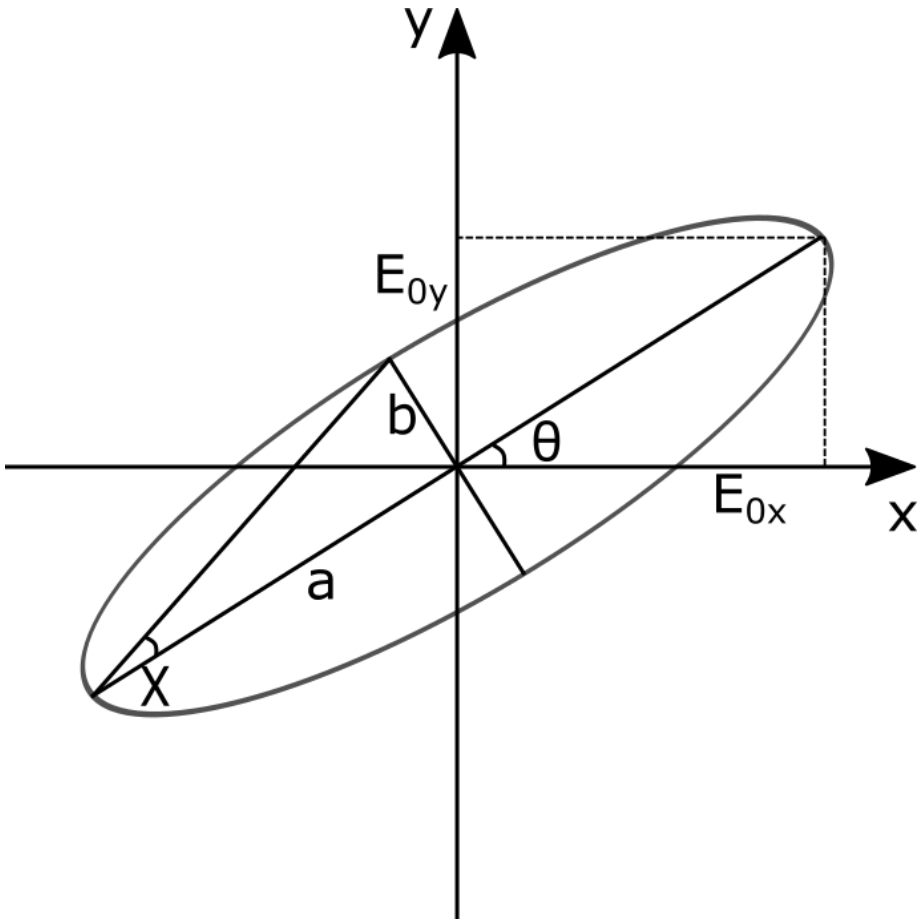

Figure 1 - The polarization ellipse, with the Azimuth ϑ, the ellipticity χ, the major (a) and minor (b) semiaxes and the components of the Electric field E_{0x} and E_{0y} on the respective axes.

This figure is called the polarization ellipse and depending on its parameters we can obtain the particular cases of all notable polarization states.
The ellipse can be described by 4 different parameters. a and b represent the length of the semi major and semi minor axis respectively. ψ is the angle of the semi major axis a with the horizontal axis, measured counterclockwise, and is called the orientation angle. Its values can vary between 0 and π. The angle between the x axis and a corresponds to θ and is named the azimuth. Finally, $\chi = \arctan(a/b)$ ($-\pi/4 \leq \chi \leq +\pi/4$) is called the ellipticity and describes the degree of the elliptical shape. The orientation angle and the ellipticity are related to the electric field parameters by the following equations:

$$tan2\psi = \frac{2E_{0x}E_{0y}}{E_{0x}^2 - E_{0y}^2} cos\Phi; \qquad (Eq.20)$$

$$sin2\chi = \frac{2E_{0x}E_{0y}sin\Phi}{E_{0x}^2 + E_{0y}^2}; \qquad (Eq.21)$$

More particular cases can be derived from the general one by selecting appropriate values of E_{0x}, E_{0y} and ϕ. The different states of polarization take their name from the geometrical figures traced by the electric field in the O_{xy} plane. In particular the most notable cases are:

- Elliptical polarization: the general case, where there is no special relationship between E_{0x}, E_{0y} and ϕ;
- Linear polarization: when ϕ = 0, the projection of $\vec{E}$ on O_{xy} is a straight line. Its orientation depends on the relative intensity of $E_{0x}$and E_{0y};
- Circular polarization: when ϕ = ± π/2 and $E_{0x} = E_{0y}$ s, the resulting projection of $\vec{E}$ is a circle. Depending on the sign of ϕ the polarization will be called circular right or circular left.

If E_{0x}, E_{0y} and ϕ do not depend from the time variable, we say that the light is completely polarized and it will be included in one of the previously described statuses. Linear and circular polarization are of particular interest because using these special cases allows to greatly simplify measurements and calculations for polarimetric measurements. This combination of properties allows us to model complex optical setups, including multiple polarizing elements, by simply multiplying the matrix of each optical element by a vector associated to the light, as we will see in the next paragraph.
One last note needs to be made about unpolarized light. When E_{0x}, E_{0y} and ϕ do depend on time, the light will be in an unpolarized state. In this case, $\vec{E}$ will change with time in a random (or at least not describable) way and its projection on O_{xy} will not form any precise geometrical figure. This is indeed the most common status of light in nature, but thankfully polarized light can be easily obtained from unpolarized light by utilizing simple polarizing elements.

3. Jones formalism

From 1941 to 1947, Robert Clark Jones introduced a new formalism to describe and calculate the behavior of polarized light and its interaction with polarizing elements [2]. In particular, he introduced the Jones vector $\vec{J}$ which corresponds to

$$\vec{J} = \begin{bmatrix} E_x \\ E_y \end{bmatrix} = \begin{bmatrix} \mathrm{E_{0x}} e^{j\Phi_x} \\ E_{0y} e^{j\Phi_y} \end{bmatrix}; \tag{22}$$

where j is a complex number such that $j^2 = -1$. By remembering that $\Phi = \Phi_x - \Phi_y$, we can simplify this equation to

$$\vec{J} = \begin{bmatrix} \mathrm{E_{0x}} \\ E_{0y} e^{j\Phi} \end{bmatrix}; \tag{23}$$

Which can be written in normalized form as

$$\vec{J} = \frac{1}{\sqrt{E_{0x}^2 + E_{0y}^2}} \begin{bmatrix} \mathrm{E_{0x}} \\ E_{0y} e^{j\Phi} \end{bmatrix}; \tag{24}$$

The vector can also be written in function of the polarization ellipse parameters as follows:

$$\vec{J} = \begin{bmatrix} \cos(\theta)\cos(\chi) - j\sin(\theta)\sin(\chi) \\ \sin(\theta)\cos(\chi) + j\cos(\theta)\sin(\chi) \end{bmatrix}; \tag{25}$$

Intensity of light can be found from $\vec{J}$ by multiplying its Hermitian adjoint (the complex conjugate of the transposed vector) $\vec{J}^{\dagger}$:

$$I = \vec{J}^{\dagger}\vec{J}; \tag{26}$$

We also introduce the Jones Matrix [J], a 4 elements (2x2) matrix that describes the polarization properties of an optical device or medium.

$$[J] = \begin{bmatrix} J_{ii} & J_{ij} \\ J_{ji} & J_{jj} \end{bmatrix}; \tag{27}$$

All J_{xx} elements of [J] are complex numbers. The interaction of a particular polarized light wave with a particular optical medium can be calculated with the simple relation

$$\vec{J}_{out} = [J] \cdot \vec{J}_{in}; \tag{28}$$

where $\vec{J}_{in}$ is the Jones vector of light before interaction and $\vec{J}_{out}$ is the Jones vector after the interaction. This convenient mathematical relation can be extended to the case where multiple optical devices are in the path of the incident light, allowing the modeling of complex optical setups presenting multiple objects in the light's path.

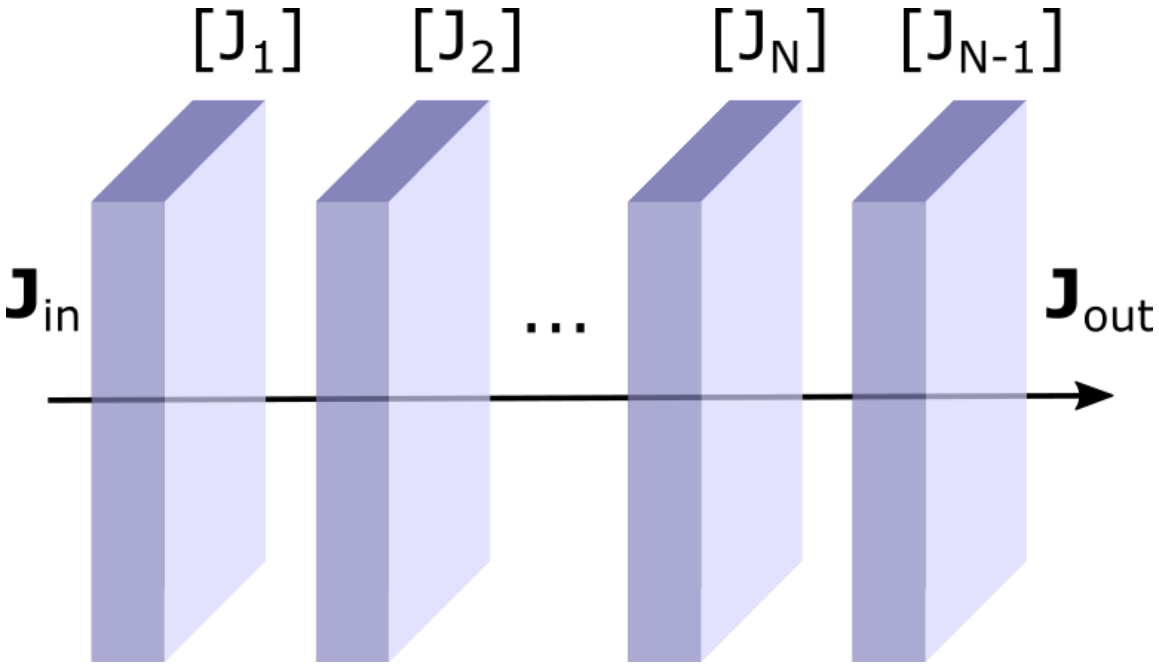

Figure 2 – Schematics of the model of light interaction with N elements with their own Jones matrix, where the incident light Jones vector $\mathbf{J}_{in}$ is transformed in the vector $\mathbf{J}_{out}$

For an N elements setup, the result will be the multiplication of N M_J elements as shown in Figure 2:

$$\vec{J}_{out} = [J_N] \cdot [J_{N-1}] \cdots [J_2] \cdot [J_1] \cdot \vec{J}_{in}; \tag{29}$$

The main limitation of Jones formalism is that it only works in the case of a purely deterministic state of polarization (i.e. not depolarized). It is therefore an ideal formalism to describe high precision optical devices such as metamaterials and engineered materials in the field of material science [3], but is not suitable to describe biological systems such as cells, lipids etc. because of the complex optical properties and high degree of depolarization (the loss of temporal coherency in the propagation of $\vec{E}$) present therein [4]. Another drawback is that the Jones matrix uses complex numbers, which results in a higher sensitivity to noise propagation [5].

4. Mueller-Stokes formalism

Mueller-Stokes formalism is another way to model polarized light interaction with matter. It is very similar to Jones formalism in many aspects, but it can be used even when the depolarization is strong and we are not working with purely deterministic optical media. Furthermore, Mueller-Stokes formalism works with directly measurable quantities (light intensity) and only utilizes real coefficients, making it much more practical in a laboratory setting. The Stokes vector $\vec{S}$ was introduced by Sir George Gabriel Stokes in 1852 [6]. It represents polarized light in function of light intensities, which makes it particularly easy to utilize in an experimental configuration as

the light intensity is the easiest quantity to measure. $\vec{S}$ is a 4x1 vector and can be written as follows:

$$\vec{S} = \begin{bmatrix} S_0 \\ S_1 \\ S_2 \\ S_3 \end{bmatrix} = \begin{bmatrix} I \\ Q \\ U \\ V \end{bmatrix} = \begin{bmatrix} < E_x^* E_x + E_y^* E_y > \\ < E_x^* E_x - E_y^* E_y > \\ < E_y^* E_x + E_x^* E_y > \\ < i(E_x^* E_x - E_y^* E_y) > \end{bmatrix}; \quad (30)$$

All $\vec{S}$ elements are real. The < > symbols denote the spatial and temporal averaging of the intensities. The S_0, S_1, S_2, S_3 and I, Q, U, V notations are equivalent and used interchangeably in polarization literature, depending on the field: the first notation is more utilized in the field of target detection and remote sensing [7] as well as biological applications [8], while the second is used in the fields of astronomy and atmospheric studies [7]. In our case, we will keep the first notation for the rest of this work.
All the elements of the vector are related to the intensity of the light. In particular:

- S_0 corresponds to the total light intensity;
- S_1 corresponds to the difference between the light linearly polarized at 0° and 90°;
- S_2 corresponds to the difference between the light linearly polarized at +45° and -45°;
- S_3 corresponds to the difference between the light circularly polarized left and right;

It's a common practice to normalize the Stokes vector by the S_0 element to obtain comparable data on the polarization regardless of the total light intensity measured in experiments. When this is performed, $\vec{S}$ can be written as a function of the parameters of the polarization ellipse as follows:

$$\vec{S} = \begin{bmatrix} 1 \\ S_1 S_0 \\ S_2 S_0 \\ S_3/S_0 \end{bmatrix} = \begin{bmatrix} 1 \\ cos2\chi cos2\psi \\ cos2\chi sin2\psi \\ sin2\chi \end{bmatrix}; \quad (31)$$

To have a Stokes vector with a physical realizability, the following relationship between its components is always true:

$$S_0^2 \geq S_1^2 + S_2^2 + S_3^2; \quad (32)$$

This is because S_0 represents the total light and can't therefore be smaller than the sum of each polarized light state. When the identity is true, the light is completely polarized. In this case, $\vec{S}$ can be written in this form:

$$\vec{S} = \begin{bmatrix} I_0 \\ I_x - I_y \\ I_{+45^\circ} - I_{-45^\circ} \\ I_R - I_L \end{bmatrix}; \tag{33}$$

Where I_0 represents the total light intensity; $I_x - I_y$ represents the different between the light intensities at 0° and 90°; $I_{+45^\circ} - I_{-45^\circ}$ represents the difference between the light intensities at +45° and -45°; $I_R - I_L$ represents the difference between the light intensities for circular right and circular left polarized light.

When light is not partially polarized, it can be described as the sum of a completely polarized component and a completely unpolarized component:

$$\vec{S} = \begin{bmatrix} S_0 \\ S_1 \\ S_2 \\ S_3 \end{bmatrix} = \begin{bmatrix} \sqrt{S_1^2 + S_2^2 + S_3^2} \\ S_1 \\ S_2 \\ S_3 \end{bmatrix} + \begin{bmatrix} 1 - \sqrt{S_1^2 + S_2^2 + S_3^2} \\ 0 \\ 0 \\ 0 \end{bmatrix}; \tag{34}$$

Where the first term represents the completely polarized light and the second one the completely unpolarized one. From these two extreme cases, we can extract the Degree of Polarization (DOP) of a wave as:

$$DOP = \frac{\sqrt{S_1^2 + S_2^2 + S_3^2}}{S_0}; \tag{35}$$

The DOP will vary between 0 for a completely unpolarized light wave to 1 for a completely polarized one and partially polarized light will fall between these two cases.

Despite the Stokes vector being introduced in the middle of the XIX century, the mathematical model to utilize it for polarization calculus was not developed until much later by Hans Mueller [9]. The formalism of Mueller is similar to Jones formalism in many aspects. Firstly, optical elements are assigned a matrix [M], named the Mueller matrix, that describes all possible optical properties of the medium. The Mueller Matrix is a 4x4 matrix where all coefficients are real numbers:

$$[M] = \begin{bmatrix} m_{00} & m_{01} & m_{02} & m_{03} \\ m_{10} & m_{11} & m_{12} & m_{13} \\ m_{20} & m_{21} & m_{22} & m_{23} \\ m_{30} & m_{31} & m_{32} & m_{33} \end{bmatrix}; \tag{36}$$

In the same way as Jones calculus, the Stokes vector resulting from an interaction with an object having Mueller matrix [M] can be easily calculated by multiplying [M] by the incident Stokes vector:

$$\vec{S}_{out} = [M] \cdot \vec{S}_{in}$$

As previously noted, since this formalism utilizes light intensities rather than the electric fields of light, it is much easier to implement experimentally. For this reason, the possibility to model a series of optical devices by simply multiplying their Mueller matrices is of great interest to model optical setups. In the case of a series of N optical elements, we will have:

$$\vec{S}_{out} = [M_N] \cdot [M_{N-1}] \cdots [M_2] \cdot [M_1] \cdot \vec{S}_{in}$$

5. Mueller matrix information

There are 3 main physical interactions that can change the polarization state of light:

- Dichroism (linear and circular)
- Birefringence (linear and circular)
- Depolarization (due to temporal and spatial averaging effects)

Each one can be connected to a simple ideal optical element that presents only that one effect. In the case of Dichroism it will be called a diattenuator, for birefringence a retarder and for depolarization a depolarizer.

6. Diattenuators

Diattenuators are optical devices that present dichroism. Dichroism is defined as a difference in transmission (or reflection) between two orthogonal polarization states. In the case of scalar dichroism for transmission, the diattenuation can be defined as

$$D = \frac{T_{max} - T_{min}}{T_{max} + T_{min}}; \quad (37)$$

Where T_{max} is the maximum transmitted light intensity and T_{min} is the minimum transmitted light intensity. The quantities are analogous for the case of reflection.
The transmittance for an unpolarized light wave will be:

$$T_0 = \frac{1}{2}(T_{max} - T_{min}); \quad (38)$$

D will be a number that is comprised between 0 and 1.

- If D = 0, the transmittance (or reflectance) will not depend on the incident light polarization;
- If 0 < D < 1, the diattenuator will be partial;
- If D = 1, the optical element will be a perfect polarizer

In particular, if the polarization states taken in consideration are linear, we will talk about Linear Dichroism (LD), while if the polarization states are circular left and right we will talk about Circular Dichroism (CD). The more general case will be that of an elliptical partial polarizer, where the diattenuation of each component will be dependent on the incident wave's polarization. The resulting vector diattenuation $\vec{D}$ will be:

$$\vec{D} = \begin{bmatrix} D_H \\ D_{45°} \\ D_C \end{bmatrix}; \tag{39}$$

Where

- D_H is the horizontal linear diattenuation ($-1 \leq D_H \leq 1$);
- $D_{45°}$ is the linear diattenuation at 45°($-1 \leq D_{45°} \leq 1$);
- D_C is the circular diattenuation ($-1 \leq D_C \leq 1$).

If $D_C = 0$ the element will be a linear diattenuator.
$\vec{D}$ can also be described in function of the parameters of the polarization ellipse as

$$\vec{D} = D \begin{bmatrix} \cos(2\chi_D)\cos(2\theta_D) \\ \cos(2\chi_D)\sin(2\theta_D) \\ \sin(2\chi_D) \end{bmatrix}; \tag{40}$$

By using $\vec{D}$ and T_0 a diattenuator can then be completely characterized. The matrix of such an element was defined by Lu and Chipman [10] as follows:

$$[M_D] = \begin{bmatrix} m_{D_{00}} & m_{D_{01}} & m_{D_{02}} & m_{D_{03}} \\ m_{D_{10}} & m_{D_{11}} & m_{D_{12}} & m_{D_{13}} \\ m_{D_{20}} & m_{D_{21}} & m_{D_{22}} & m_{D_{23}} \\ m_{D_{30}} & m_{D_{31}} & m_{D_{32}} & m_{D_{33}} \end{bmatrix} = T_0 \begin{bmatrix} 1 & \vec{D}^T \\ \vec{D} & [m_D] \end{bmatrix}; \tag{41}$$

Where $[m_D]$ is the reduced matrice of diattenuation

$$[m_D] = \sqrt{1 - D^2}[I_3] + \left(1 - \sqrt{1 - D^2}\right)\hat{D}\hat{D}^T; \tag{42}$$

$\widehat{D}$ is the unity vector representing the direction of the dichroic axis and $[I_3]$ is the 3x3 identity matrix.

7. Retarders

Retarders are optical elements that present birefringence. Birefringence is the property of an object to change the phase of light traversing it. A birefringent material for example can present a different refractive index depending on its axis:

- Refractive index n_o on the ordinary axis
- Refractive index n_e on the extraordinary axis

This difference in refractive index n_e-n_o will then cause a difference in travel speed of light that's polarized along the ordinary or extraordinary axis. This in turn will lead to a change in the difference of the phase of the two components. In the general case we define retardance in the following way:

$$R = |\Phi_2 - \Phi_1| = \frac{2\pi}{\lambda}\Delta ne; \tag{43}$$

Where Φ_1 and Φ_2 are the phases of light polarized along the different retarder axes and Δne is the difference in refractive indexes along the two axes. The value of R defined as such will be $0° \leq R \leq 180°$.
As with dichroic materials, retarders can present both Linear (0°/90° and 45°/-45°) and circular (left and right) birefringence. A typical ideal birefringent device in optics is a waveplate. For example a λ/4 waveplate will change the phase of the wave by $\frac{1}{4}\lambda$ of the incident light.

8. Depolarizers

Finally, it's worth mentioning the effect of depolarization. When an optical element turns completely polarized light in partially or completely unpolarized light, it will be called a depolarizer. Depolarization can be isotropic in space or anisotropic if it depends on the axis along which the light travels. The main cause of depolarization is the averaging of the of the degree of error of the interacting polarization states.
The normalized Mueller Matrix of a generic depolarizer [M_Δ] will be:

$$[M\Delta] = \begin{bmatrix} 1 & 0 & 0 & 0 \\ 0 & a & 0 & 0 \\ 0 & 0 & b & 0 \\ 0 & 0 & 0 & c \end{bmatrix}; \tag{44}$$

Where a, b and c are comprised between 0 and 1 and in the case of a depolarizer that acts in the same way on all polarization states $a = b = c$. The general depolarization coefficient will be:

$$\Delta = 1 - \frac{|a| + |b| + |c|}{3}; \tag{45}$$

In this case then:

- $\Delta = 0$ will mean a perfectly non-depolarizing element;
- $0 < \Delta < 1$ will mean a partial depolarizer;
- $\Delta = 1$ will mean a complete depolarizer, turning polarized light in completely unpolarized light.

Most optical devices will present some degree of depolarization due to defects and wear.

Part 2: Mueller/Stokes measurement

1. Mueller setups

To measure the Mueller Matrix of an unknown sample multiple polarization states are generated to be shined on the sample and its response is then analyzed.

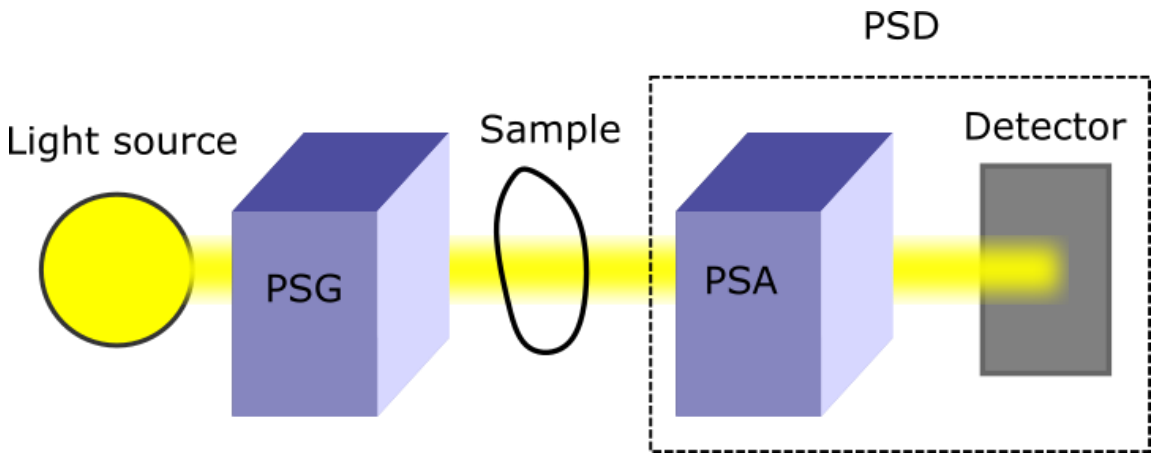

Figure 3 – The block diagram of a generic Mueller matrix polarimeter. PSG: Polarization States Generator. PSA: Polarization States Analyzer. PSD: Polarization States Detector.

Operationally, the typical setup is shown in Figure 3 and is composed of the following elements (in order) [11]:

- A light source;
- A Polarization States Generation (PSG): the conjunction of all optical devices (polarizers, waveplates, etc.) used to generate the desired polarization states;
- The sample of which the Mueller matrix has to be measured;
- A Polarization States Analyzer (PSA): the conjunction of all optical devices used to analyze the desired polarization states;
- A polarization insensitive detector.

The conjunction of the PSA and detector can also be named Polarization States Detection (PSD). Depending on the optical devices utilized and their relative orientations in space and time, such a setup can allow to retrieve all elements of the unknown sample's Mueller Matrix or only part of them. In the first case the setup will be called a complete Mueller Polarimeter, while in the second case it will be incomplete [12]. Since the full Mueller Matrix is a 16 element matrix, mathematically a minimum of 16 measurements is required to recover the full Mueller Matrix of the sample. More measurements are not necessarily required, but can reduce the error in the elements by obtaining an overdetermined linear system (number of equations > number of

Different approaches can be used to obtain the necessary measurements. In particular, different techniques can be used to divide each polarization state for generation/analysis:

- Temporal encoding
- Spatial encoding
- Spectral Encoding

2. Temporal encoding

In the case of temporal encoding, the polarization states are generated and analyzed sequentially in time.

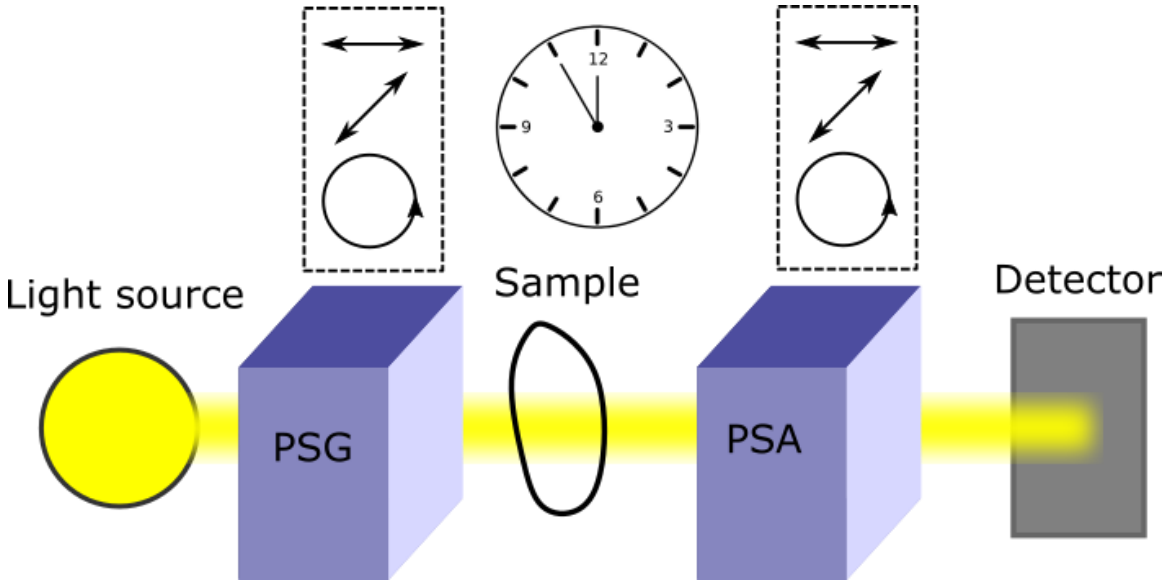

Figure 4 – Schematics of a temporal domain setup. Polarization states are generated and analyzed sequentially over time.

The simplest form of this kind of setups utilizes simple waveplates and linear polarizers that are mechanically rotated. As can be expected, since at least 16 measurements need to be taken and physical motors require time for the rotation, this methodology is slow (up to a few minutes for a 180° measurement). In exchange, it is probably the simplest one to implement and doesn't require complex engineering solutions or advanced devices. The acquisition speed can be improved by utilizing electronic devices like Photoelastic Modulators (PEMs), Pockels cells and liquid crystals [13] [14] [15] which generate periodically all possible polarization states of light at frequencies that go from ~50kHz for PEMs to ~MHz for Pockels cells [16].This clearly improves acquisition speed, at the cost of increasing the complexity of the system and requiring a strict temperature control of the devices to avoid instability (especially in the case of Pockels Cells). These devices work by inducing a time-varying periodic birefringence in a crystal thanks to periodical stress in what is called the photoelastic effect [17] [18]. Multiple devices can be utilized at the same time to increase the speed of acquisition and number of Mueller matrix elements that can be measured without moving parts. Adding a second PEM, this time in the PSA, and

synchronizing its phase with the one in the PSG allows to have a complete Mueller polarimeter without moving parts [19]. By choosing two PEMs with different resonant frequencies, the independent Fourier harmonics will be increased, which in turn leads to a higher number of possible Mueller matrix elements to measure without moving physical parts of the setup. In this way, all elements of the Mueller matrix can be obtained in just 1ms [20] [21]. Information on LD, LB, CD and CB can be extracted at the same time [22] [23]. Finally, the setup can be upgraded once more by adding a third [24] and even fourth PEM [25] [26] [27]. In the four PEM setup, two will be positioned in the PSG and two in the PSA. In this kind of setup, all Mueller matrix elements can be obtained in a snapshot without any moving parts and the use of an FPGA card allows real-time acquisition. For this reason, the approach is highly suited to studying fast events like conformational changes in in biopolymers [28] [29] [30].

3. Spatial and Spectral encoding

Temporal encoding has been the technique that was chosen for the work developed during the course of this thesis. Nevertheless, we will proceed to describe briefly the two other main encoding techniques in Mueller matrix studies: spatial encoding and spectral encoding.
In the case of spatial encoding, the total information is retrieved by spatially separating the information relative to different polarization states. Different approaches exist for this encoding methodology:

- Division of Amplitude (DoA), in which multiple detectors and beam splitters are utilized to divide the generation and/or detection of different polarization states [31] [32]. In this case measurement time will decrease due to parallelization, but the setup could be bulky;
- Division of Aperture (DoAP), in which the detector is constituted by a camera in which each pixel is subdivided in various subpixels, each selective of one particular polarization state [33]. Again acquisition speed will be faster, but in this case we will have a loss in resolution due to the subpixel division of the camera.

Spectral encoding works by utilizing a broad enough light source. Different polarization states are encoded at different wavelength intervals and a spectrometer allows to analyze them separately. Again, this technique improves the acquisition speed of the setup, but the main limitation is having the required light source and the fact that the polarimetric signature of the sample needs to be stable with the change of wavelength to not cause artifacts in the measurement results.
Finally, it's worth noting that Mueller Matrix measurements can be done both in a 1 point spectroscopic mode and in an imaging mode. In this last case, the necessary polarization control devices need only be implemented in the microscope's light path.

4. Single-PEM Mueller setup

The single PEM setup will now be described in more depth. In particular, the mathematical process leading to the extraction of specific Mueller matrix elements will be described, as will all the relations between angles of the optical devices needed to do so. We note that the extraction can happen both by raw calculus and by utilizing a lock-in amplifier to obtain directly the intensity at each harmonic of the demodulated signal. In Figure 5 the setup is shown with all its components.

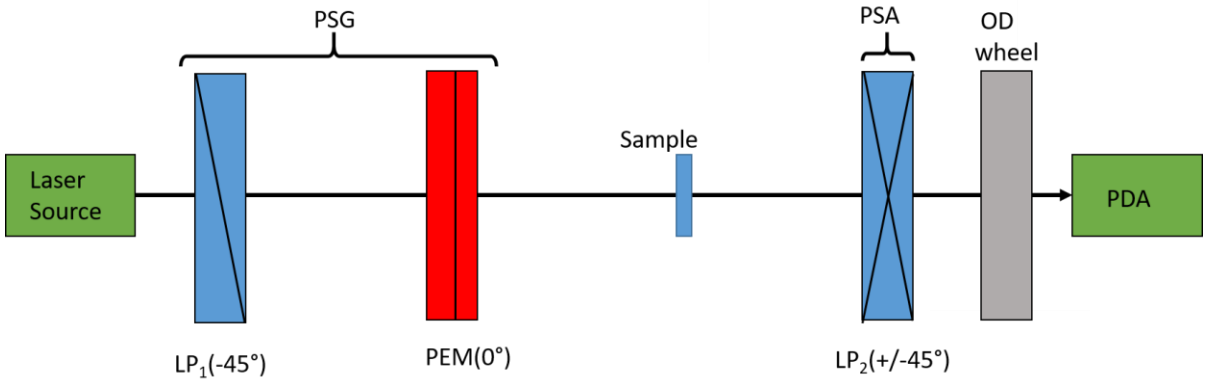

Figure 5 – The block diagram of a single PEM setup that can measure the m_{03} element of the Mueller matrix. The objective and condenser are optional and only needed in the microscopy configuration. PSG: Polarization States Generation; LP: Linear Polarizer; PEM: Photoelastic Modulator; PSA: Polarization States Analyzer; PDA: Light Detector. The angles represent the angle of the optical axis of the optical element relative to the reference angle.

As can be seen, the PSG is composed of a linear polarizer and the PEM, while the PSA is composed by a polarized beam splitter separating the light in two orthogonal polarization states that are detected by two APDs. By taking the angle of orientation of the PEM as a reference, the angles will be θ_{LP1}=-45°, θ_{PEM}=0° and θ_{LP2}= ±45°. The resulting stokes vector of the light after interaction with the whole setup, as incident on the detector can then be calculated by Mueller matrix calculus with the following formula:

$$\vec{S}_{out} = [M_{LP_2}] \cdot [M_S] \cdot [M_{PEM}] \cdot [M_{LP_1}] \cdot \vec{S}_{in}$$

Where the specific matrices for each optical element will be as follows:

$$M_{LP_1}(-45°) = \begin{bmatrix} 1 & 0 & -1 & 0 \\ 0 & 0 & 0 & 0 \\ -1 & 0 & 1 & 0 \\ 0 & 0 & 0 & 0 \end{bmatrix} \quad M_{PEM}(0°) = \begin{bmatrix} 1 & 0 & 0 & 0 \\ 0 & 1 & 0 & 0 \\ 0 & 0 & \cos(\delta) & \sin(\delta) \\ 0 & 0 & -\sin(\delta) & \cos(\delta) \end{bmatrix}$$

$$M_{LP_1}(-45°) = \begin{bmatrix} 1 & 0 & -1 & 0 \\ 0 & 0 & 0 & 0 \\ -1 & 0 & 1 & 0 \\ 0 & 0 & 0 & 0 \end{bmatrix} \quad M_{LP_1}(+45°) = \begin{bmatrix} 1 & 0 & 1 & 0 \\ 0 & 0 & 0 & 0 \\ 1 & 0 & 1 & 0 \\ 0 & 0 & 0 & 0 \end{bmatrix}$$

Where δ is the time-dependant retardance of the PEM.

Taking the case where $\theta_{LP_2} = +45°$, the result of these simple matrix-vector multiplications will lead to

$$\vec{S}_{out} = \begin{bmatrix} m_{00} - m_{02}\cos(\delta) + m_{20} - m_{22}\cos(\delta) + m_{23}\sin(\delta) \\ 0 \\ m_{00} - m_{02}\cos(\delta) + m_{20} - m_{22}\cos(\delta) + m_{23}\sin(\delta) \\ 0 \end{bmatrix}; \tag{46}$$

Analyzing the light intensity with a polarization insensitive detector is the equivalent of multiplying the Stokes vector by an horizontal [1 0 0 0] vector, which results in a measured intensity of:

$$I = m_{00} - m_{02}\cos(\delta) + m_{03}\sin(\delta) + m_{20} - m_{22}\cos(\delta) + m_{23}\sin(\delta)\,; \tag{47}$$

It must be reminded that the retardance δ of the PEM is a function of time:

$$\delta(t) = Asin(\omega t); \tag{48}$$

Assuming the static retardance and phase of the PEM to be zero. Thus, the measured intensity can be divided in a component depending on time for elements that depend on δ and one independent of time:

$$I(t) = I_{DC} + I_C \cos\big(\delta(t)\big) + I_S \sin\big(\delta(t)\big); \qquad (Eq.49)$$

Where $I_{DC} = m_{00} + m_{20}$, $I_C = m_{02} - m_{22}$ and $I_S = m_{03} + m_{23}$.

To calculate the sinus or cosinus function of a sinus function for I_C and I_S, the Bessel development is used:

$$\begin{cases} \sin\big(\delta(t)\big) = 2\sum_{k=1}^{\infty} J_{2k-1}(A)\sin\big((2k-1)\omega t\big) \\ \cos\big(\delta(t)\big) = J_0(A) + 2\sum_{k=1}^{\infty} J_{2k-1}(A)\cos\big((2k-1)\omega t\big) \end{cases}; \qquad (Eq.50)$$

Where A is the amplitude of the Bessel funtions and J_x are the Bessel coefficients, which are fixed tabled numbers in function of A.

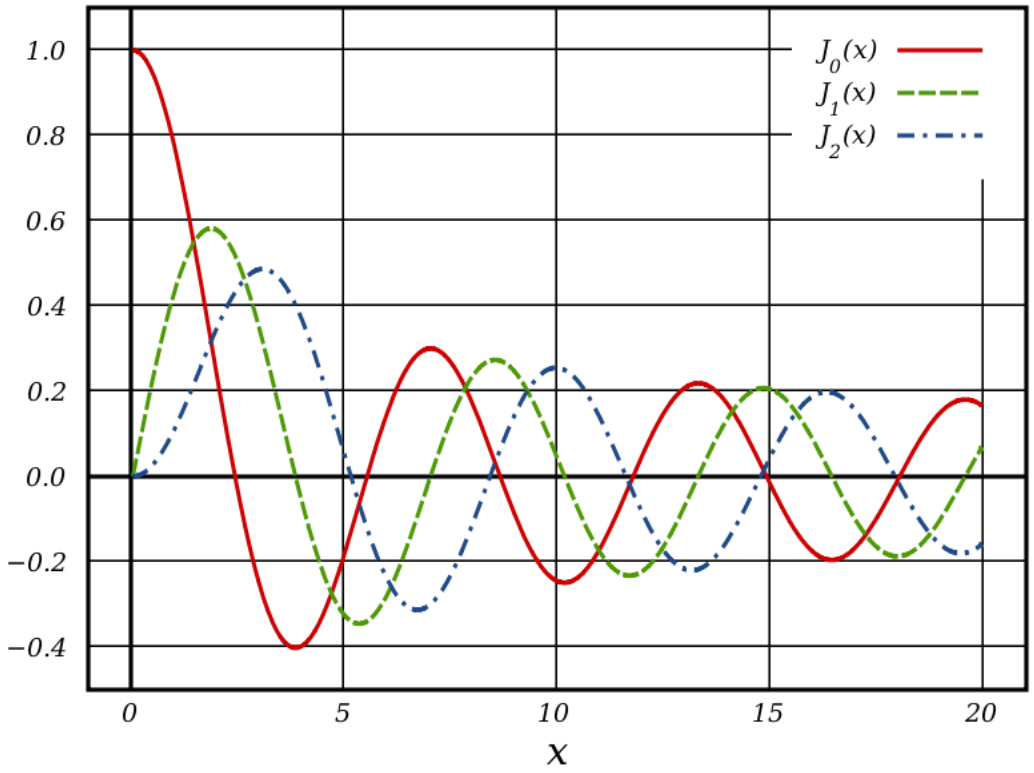

Figure 6 – The representation of the first two orders of the Bessel functions. The y axis represents the value of the Bessel coefficients, normalized to 1, as a function of their argument x, denoted as A in our calculations. As can be noticed, as the order increases, the amplitude lowers.

Approximating to the second order leads to

$$\begin{cases} \sin\big(\delta(t)\big) \approx 2J_1 \sin(\omega t) \\ \cos\big(\delta(t)\big) \approx J_0 + 2J_2 \cos(2\omega t) \end{cases}; \tag{51}$$

From this equation we can see that information can be extracted at ω (the driving frequency of the PEM) and 2ω. By continuing the Bessel development at higher orders, information at higher frequencies can be accessed, but the drawback is that the signal to noise ratio will be lower and lower the higher the analyzed frequency. The signal can be extracted by way of a spectral domain analysis or by utilizing a Lock-In amplifier locked in at the frequency of the PEM. By applying the Bessel development to the I(t) equation, we then obtain

$$\begin{aligned} I(t) = m_{00} + m_{20} + J_0(-m_{02} - m_{22}) + 2J_1(m_{03} + m_{23}) \cos(\omega t) \\ +2J_2(-m_{02} - m_{22}) \sin(2\omega t)\,; \end{aligned} \tag{52}$$

By remaking the same calculations for $\theta_{LP_2} = +45°$, we will obtain a different equation for the measured light intensity:

$$\begin{aligned} I(t) = m_{00} - m_{20} + J_0(m_{22} - m_{02}) + 2J_1(m_{03} - m_{23}) \cos(\omega t) \\ +2J_2(-m_{22} - m_{02}) \sin(2\omega t)\,; \end{aligned} \tag{53}$$

The J_0 element of the equations can be eliminated by choosing the proper value of A=2.4048. In this way $J_0 = 0$ and the term depending on it can be eliminated from the equation, leading to a significant simplification [34].

Each equation can be divided in terms that do not depend on the PEM frequency, terms that depend on ω and terms that depend on 2ω. The relations are summarized in the following table:

Frequency	Θ(LP$_2$)=-45°	Θ(LP$_2$)=-45°
0 (DC)	$m_{00} + m_{20}$	$m_{00} - m_{20}$
ω	$2J_1(m_{03} + m_{23})$	$2J_1(m_{03} - m_{23})$
2ω	$2J_2(-m_{02} - m_{22})$	$2J_2(-m_{22} - m_{02})$

Table 1 – The Mueller matrix elements that can be extracted with the Linear Polarizer in the PSA rotated at -45° (second column) and +45° (third column) in the continuous component, at the PEM driving frequency ω and at 2ω.

As can be seen, each part of the equation contains two different elements of the Mueller matrix, for a total of six elements that can be retrieved from these two measurements. Due to the weakening of signal at higher orders, which leads to a signal lower than the noise threshold, we stopped at the second order. If one is able to reduce noise enough to measure higher orders, then the information on the same elements at multiples of ω and 2ω is available, but at higher frequencies and thus at faster speeds.

Simply by subtracting and adding both results, the single elements will be extracted.

Frequency	$I_{-45°} - I_{45°}$	$I_{-45°} + I_{45°}$
0 (DC)	$2m_{20}$	$2m_{00}$
ω	$4J_1 m_{23}$	$4J_1 m_{03}$
2ω	$-4J_2 m_{22}$	$-4J_2 m_{02}$

Table 2 – The Mueller matrix elements resulting from the sum and difference of the measurements with the Linear Polarizer in the PSA at +45° and -45°.

5. Complete Single-PEM Mueller polarimeter

Being able to only extract 6 elements of the Mueller matrix makes the previously described setup an incomplete polarimeter, with missing information about some of the optical properties of the sample. It's worth noting that by changing some of the angles in the setup, information on more elements can be calculated. Despite this, the last row of the Mueller matrix (m_{30}, m_{31}, m_{32} and m_{33}) cannot be obtained with this kind of setup simply by rotation of the optical elements. To obtain them, the addition of at least another optical element in the PSA is required. In particular, a QWP before the LP would allow to obtain all elements of the matrix, making this setup a complete polarimeter. Below is summarized the list of obtainable elements at all possible configurations of the setup:

$\Theta(LP_1)$	Θ(PEM)	Θ(QWP)	$\Theta(LP_2)$	MM elements
-45°	0°	/	+/-45°	m_{00}, m_{02}, m_{03}, m_{20}, m_{22}, m_{23}
-45°	0°	/	0°/90°	m_{00}, m_{02}, m_{03}, m_{10}, m_{12}, m_{13}
-45°	0°	0°/90°	45°	m_{00}, m_{02}, m_{03}, m_{30}, m_{32}, m_{33}
0°	45°	/	0°/90°	m_{00}, m_{01}, m_{03}, m_{10}, m_{11}, m_{13}
0°	45°	/	+/-45°	m_{00}, m_{01}, m_{03}, m_{20}, m_{21}, m_{23}
0°	45°	0°/90°	45°	m_{00}, m_{01}, m_{03}, m_{30}, m_{31}, m_{33}

Table 3 – The Mueller matrix elements that can be measured in the single-PEM setup by changing the angle of each optical element.

Part 3: Applications of polarimetry

1. Atmospheric sensing

Remote sensing and specifically the characterization of aerosol particles is one of the most apt applications for polarimetry [35]. The optical thickness of the aerosol, as well as the size distribution and particle shape can be retrieved by measuring scattered sunlight with a combination of polarimetric techniques sensitive to the spectral and angular signal. The final objective of such measurements is to determine the health hazard posed by aerosols and probe natural phenomenons like volcanic gas clouds which could disrupt human activities, as well as helping in creating and perfecting climate modeling. The measurements can be done both by ground [36] and satellite instruments [37] [38] [39] [40] [41]. The second category is particularly interesting for it capacity of observing vast portions of the atmosphere. In particular in this field, a few instruments can be cited.

POLDER [37] is the pioneering instrument for remote polarimetric sensing, leading the way to improved implementations after its success. POLDER itself is an imaging system with a fisheye lens that utilizes a rotating wheel to employ multi wavelength and multi polarization capabilities. The wheels in the filters contain three wavelength (433nm, 670nm and 865nm) filters and three polarization filters (at 60° between each other). By combining all of them, the linear polarization information at all three wavelengths can be recovered, resulting in a 2% polarization accuracy after corrections due to movement of the satellite and due to the fisheye lens.

This kind of precision is too low for chemical composition detection of aerosols [35], where a 10^{-3} precision is needed, which led to the development of other instruments:

The Research Scanning Polarimeter [38] allows parallel measurement of the linear polarization states thanks to a system of boresights and dichroic beam splitters, with Wollaston prisms separating the polarized components at 0/90° and +45/-45°. The system can achieve an accuracy of 0.2%. Another instrument is the Multi angle SpectroPolarimeter Imager MSPI13, which can achieve a 0.5% accuracy by utilizing a dual PEM setup at three different wavelengths. The beat signal of the two PEMs at 12.5Hz modulates the signal for the detector in a fast enough way to suppress polarization artifacts. This setup allows the simultaneous setup of linear stokes vector parameters by using a grid of polarizers at 0° and 45° over the field of view.

Finally, the SPEX [41] is an instrument that is based on the spectral modulation approach for polarization and allows for both spectral and polarization information in a single shot, eliminating some of the temporal errors due to other approaches and reaching an accuracy of 0.2%.

2. Target detection

Target detection is the application of polarization to the imaging of faraway object to enhance the contrast and distinguish information otherwise hidden. Some examples of use are machine vision and military application, where the polarization information can be combined with optical and thermic information to obtain a more complete and fast identification of distant targets. As the interest is to detect objects at a distance, the apparatus required for the measurement must work by measuring the reflected light from the objects in the environment [35]. The measuring

apparatus can be of two kinds. The first, most simple one, utilizes ambient light and only includes a PSA and detector to decode usually the linear polarization parameters of the incident stokes vector from the ambient scenery. The second is to shine a polarized light from a distance that is polarized by a PSG and then analyze the rays that are reflected back with a PSA and detector. Since these approaches need fast and simple decoding of the information, the usual approach utilized is that of division of amplitude or division of aperture, to obtain the desired elements of the stokes vector in a faster way than temporal measurements.

3. Astronomy

Another field of application for Mueller-Stokes measurements is astronomy, where the technique is utilized in two different configurations [35]:

- Imaging of celestial bodies like stars and exoplanets [42], shown for example in Figure 7;
- Line spectropolarimetry, used to probe the composition in the interstellar environment.

The instruments work by applying the same principles of Mueller-Stokes measurement already proposed: telescopes are fitted with polarization devices to analyze the incoming polarization state of light and deduce its creation. Considering the astronomical distances, an approach where light is sent to the target and the reflection is analyzed is out of the question because of the enormous distances and time scales, so the approach is limited to naturally incoming light.

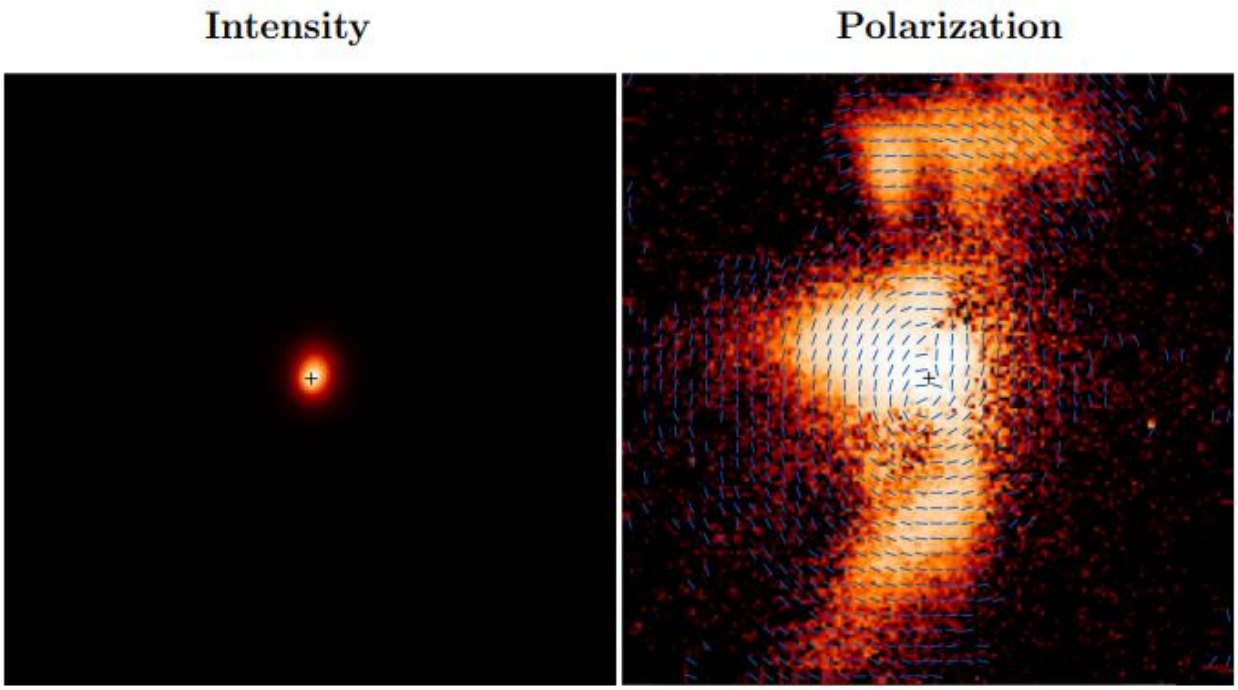

Figure 7 – Intensity (left) and polarization(right) imaging by ExPo of the star T Tauri [35].

In the case of spectopolarimetry, the circular dichroism arising from the Zeeman effect is usually utilized to study the incoming light [43]. The Zeeman effect consists in the circular polarization of light due to magnetic field interaction and it has been used for over a century to study, in conjunction with other phenomena like the Doppler effect, the map of magnetic fields around stars [35]. In general, polarization changes in the light can arise when an object deviates from the ideal spherical shape, which is the case in most real scenarios, even for stars.

One of the main challenge in astronomical polarization study is the twinkling effect due to atmosphere movement during measurements, which causes errors and disturbance in consecutive polarization measurements to reconstruct the incoming stokes vector, limiting the accuracy to 10^{-3}. To solve this problem, an approach is to use a temporal approach and to modulate the polarization actively at speeds faster than the twinkling phenomenon (around 1kHz), coupled with special CCD detectors to keep up with the modulation speed [44] consisting of a CCD detector coupled with a stripe mask synchronized with the polarization modulation. Thousands of polarization cycles allow to read the image by interlacing the images at the detector, allowing for greatly increased polarization sensitivity, only limited by the photon collection. For this reason, the larger the telescope, the more the polarization can be accurate. Other methods to improve the polarization accuracy include the binning of pixels and the combination of multiple similar polarization lines [45]. In general, particular care needs to be put in the calibration of the setup and its stability over time as the polarization accuracy is limited by the great quantity of required mirrors and optical elements required to operate a telescope before the polarization optics that can change the polarization itself, as well as problems like the dirtying and aging of components.

One of the direct applications of polarization imaging in astronomy is the observation of exoplanets around faraway stars. The contrast in light intensity between the light coming from the star and the light reflected by the planet has a difference of the order of $10^{-7}/10^{-10}$. Despite this, the light reflected from the planets is highly polarized, while direct light from the star is unpolarized and therefore polarization imaging can help increase the contrast during observation. By measuring in function of the wavelength and phase angle of the planet, polarization detection can allow to obtain information on the presence of liquid water and atmospheric oxygen, giving insight on the possible habitability of the planet. Further information on the presence of life on exoplanets can also be extracted from the circular polarization signal arising from homochirality in biological structures (DNA, chlorophyll, sugars etc) [46].

4. Biomedical imaging

A very important application of polarization measurement is biomedical diagnostics [47] [48] [49] [50] [51] [52], since polarization imaging allows for a fast, label-free way to image human tissues, enhancing the contrast of modifications due to illness. For example, by measuring light linearly polarized parallel and perpendicular to the generated polarization, separation of the information coming from different depths of the sample can be achieved [48]. This is because light coming from interaction at a greater depth will be more likely to be the object of multiple scattering interactions, which change the polarization more than the single scattering events that happen at the surface. By making a differential measurement of the two states, information on the

depolarization and degree of polarization can be obtained, which is a useful tool for cancer diagnosis as the progression of the illness can lead to changes in the polarimetric signature of the sample. In particular, it was shown on skin cancer that the main parameters to check as markers for the progression of the illness are depolarization and retardance [53]. Setups of this kind follow the classic Mueller form: a PSG that generates some or all (depending on the approach and number of Mueller elements needed) polarization states of light, the sample and a PSA to decode the polarization states of interest.
Fiber structures that present a great degree of orientation such as collagen or neural axons present a big retardance that can be detected with Mueller imaging Figure 8.

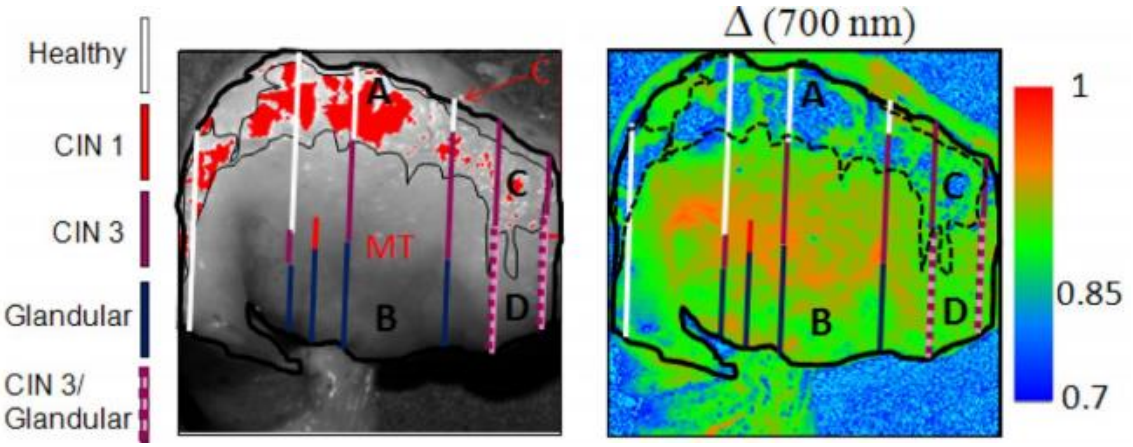

Figure 8 – Images of the light intensity (left) and of the depolarization Δ (right) for a biopsy of uterine cancer. The area contoured by the light black line represents the pathologic part of the sample. Image adapted from [54].

In-vivo measurements can be done on internal organs, but such measurements require appropriate devices. An optical fiber to reach the organ is needed [55] and some effects need to be taken into account. In particular, the optical fibers do not generally induce depolarization but do act as retarders, and this effect needs to be taken into account during the measurements if the PSG and PSA are at the external end of the fiber. It is still difficult to have PSG and PSA at the measuring end of the fiber and thus these effects are of great importance.

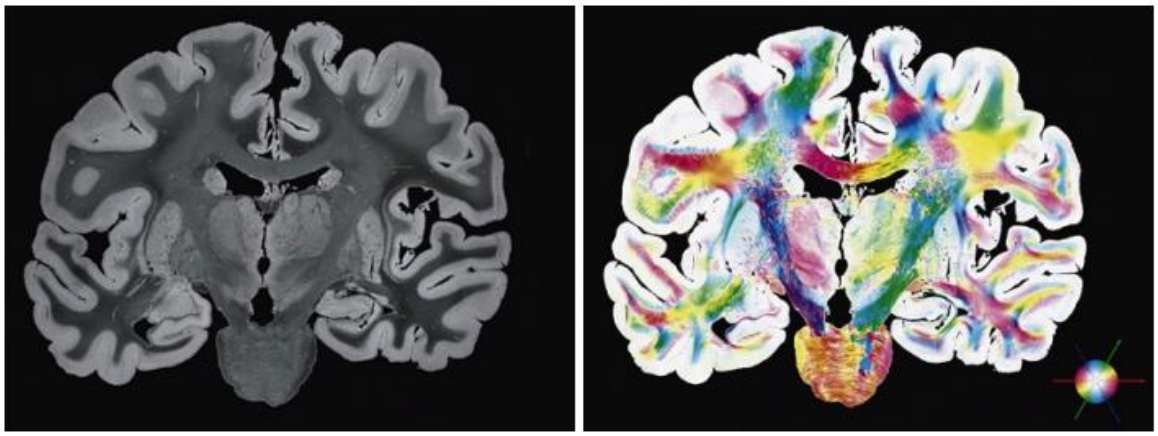

Figure 9 – Images of brain slices in intensity (left) and reconstructed fiber geometry (right) from polarization measurements (adapted from [54]*).*

Finally, samples can be imaged with Mueller polarization contrast as an enhancement mechanism. An example is reported in Figure 9 where the structure of the neural fibers is revealed by polarization imaging.

Another application of imaging has been on the study of glaucoma [56], where it was shown that, unlike in cancer detection, diattenuation in the cornea is the best indicator of development of the illness, as shown in Figure 10.

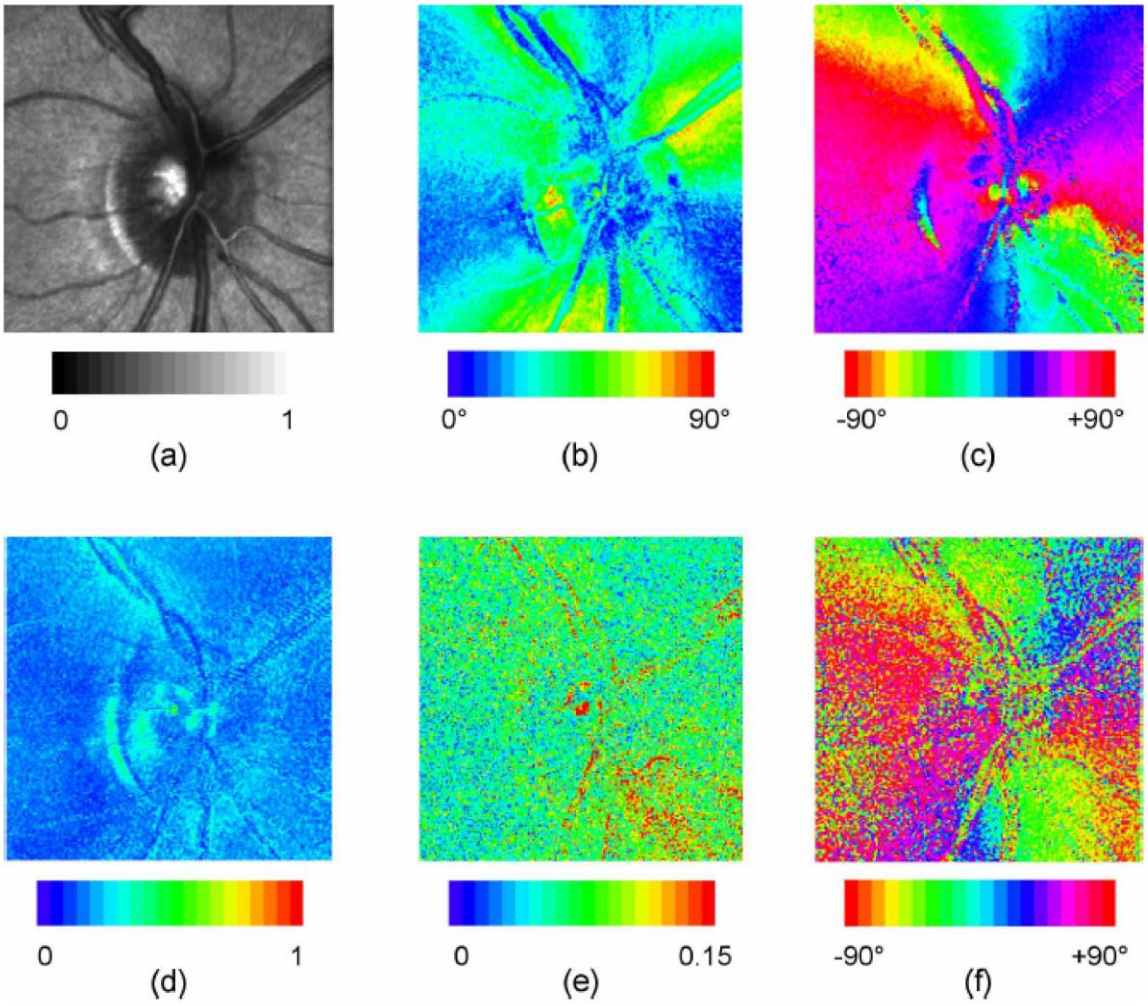

Figure 10 – Images of the optical nerve. (a) Imageof intensity; (b) Image of the linear retardance; (c) Image of the orientation of retardance; (d) Image of the depolarization index; (e) Image of the linear diattenuation; (f) Image of the linear diattenuation orientation; Picture from [56]

Conclusions

In this first chapter we have introduced light and its mathematical treatment in the form of Maxwell formalism and explained some of its consequences like the derivation of the speed of light in a medium. We have then proceeded to talk about the polarization of light and how it can be described mathematically using Jones formalism. This approach describes light as a two elements complex vector and each object as a 2x2 complex matrix. Jones formalism only holds in particular cases: when light is completely polarized and the optical elements considered are perfect. Such an approach is not fitting for samples that present a non-negligible depolarization effect, such as biological samples. For this reason, the Mueller-Stokes formalism has been introduced. It presents a similar approach to the Jones formalism, but has a 4 elements vector and 4x4 matrix, both of real coefficients, to describe polarized light in function of measurements of light intensity. We provided a description of the elementary polarization effects (dichroism, birefringence, depolarization) and of the basic ideal optical elements that present them (diattenuators, retarders and depolarizers).

The general form of a Mueller polarimeter has been presented, showing the general structure of a light source, a Polarization States Generation (PSG), with the role of creating the desired polarization states; the sample; a Polarization States Analyzer (PSA), with the role of separating and measuring the polarization states of the outgoing light; and a detector to measure the light intensity. Such setups allow to extract information on the Mueller matrix of a sample in the light's path, and thus on its optical properties. These setups are divided in complete Mueller setups, if the measurements allow to retrieve the whole matrix, or incomplete Mueller setups if they only allow the determination of some of the elements. Different approaches to obtaining complete and fast Mueller polarimeters are explained and a comparison is shown between the different techniques (temporal encoding, spatial encoding and spectral encoding of the polarization states). The mathematics behind the modeling of such setups and the extraction of particular Mueller matrix elements are demonstrated for the case of a particular setup utilizing a photoelastic modulator (PEM) in the PSG to generate all possible polarization states with a temporal approach as this is the modality that has been used for this work.

Finally, in the last part of this chapter we have presented some of the many fields in which Mueller polarimetry is utilized: atmospheric sensing, target detection, astronomy and biological imaging. The versatility of the technique allows to have applications in the most diverse fields. In the next chapter, the focus will be shifted in particular on the m_{03} element of the Mueller matrix and how it can be used to study conformational states of biological samples via spectroscopy techniques.

Chapter 2: Spectroscopic Circular Intensity Differential Scattering (CIDS)

Introduction

Circular Dichroism has been introduced in the first chapter as the differential absorption of the circular left and right polarized light intensities through a medium. While the biggest part of CD is due to the difference in absorbance exclusively in the forward direction, a smaller component is due to their differential scattering [57] [58] [59]. This signal is called Circular Intensity Differential Scattering (CIDS) [60] and its intensity is of the order of 10^{-4} times smaller than the absorption component outside the absorption band.

This technique is of particular interest because it has the advantage of being simply implemented and cheap, needing only simple optical devices like linear polarizers and waveplates that can be inserted in the light's path, while allowing a label-free approach to study of chiral structures. Such structures are present in many different samples, ranging from metamaterials, chloroplasts, viruses, bacteria, all the way to biopolymers aggregates and chromatin. This last application is the one of greater interest for the scope of the work done during this thesis.

In this chapter, the basics of chiral structures and light scattering will be discussed first, including a mention of the Mie and Rayleigh regimes. The first is valid when the scattering particle's diameter is equal to or greater than the wavelength of the interacting light and the second one when the diameter is $1/10^{th}$ of the wavelength or smaller.

Next, the theory of CIDS will be explained. The models utilized to describe CIDS interaction will also be presented and their accordance with experimental measurements will be described. During my work I have studied two main areas of spectroscopic CIDS: spectral (when the wavelength is varied) and angular (when the information is studied in function of the angle of emission). A list of application in various fields of CIDS spectroscopy techniques, as well as different setups will be given.

Our own home made CIDS spectroscopy measurement setup will be described, including schematics, calibration and characterization procedures. The setup has been validated by utilizing at first simple chiral arabinose molecules and has then been utilized to study isolated HEK cell nuclei, to measure the signal coming from the chiral structures inside the chromatin.

Finally, the last part of the chapter will deal with a different approach to CIDS spectroscopy: Polarized Light Scattering Spectroscopy (pLSS). This technique aims at obtaining the angular information of CIDS without the need of a mechanical moving arm, thus greatly increasing the speed of acquisition from a few minutes for a complete measurement to a few seconds. The pLSS setup built by us will be described, as well as some preliminary results obtained on polypropylene microsphere solutions which show promise for future applications to cells and nuclei to study chromatin conformation.

Part 1: Chirality and CIDS theory

1. Chiral structures

Chirality is a symmetry property of physical structures. In particular, a chiral structure is one that cannot be superposed with its mirror image by simple rotations and translations. The origin of the word comes from the greek χειρ (kheir), which means hand. This is because hands are one of the most common examples of chiral object. By superposing the right and left hand, we can see that we will not be able to find an exact correspondence, even though they are the mirror image of each other. The same can be said from examples found everywhere in nature. A particular field of interest for this kind of information is organic chemistry and biophysics: the properties of molecules are highly dependent on the chirality of their bonds and for these reason many drugs are composed of a specific chiral molecule to be effective [61].

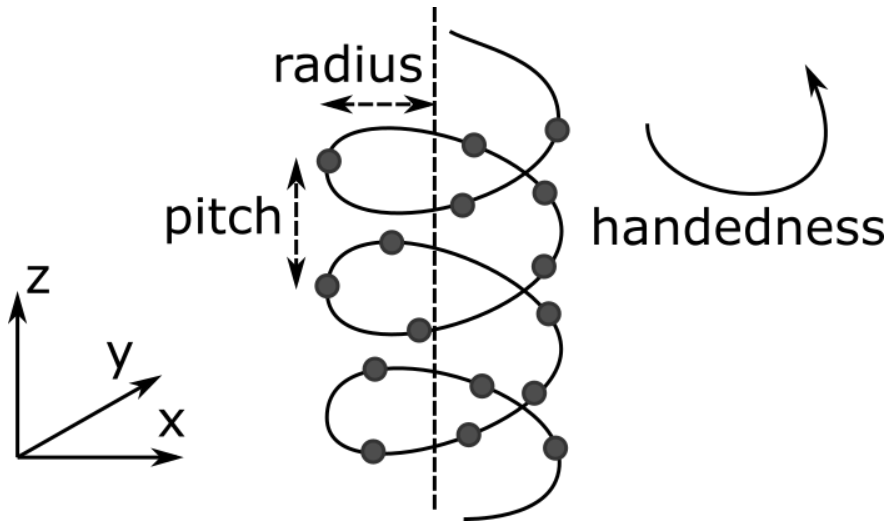

Figure 11 – Helical chiral structure and its main parameters. In this case the helix is right handed. Radius is measured as the distance between the helix and the central axis in the xy reference plane and pitch is the distance between superposing parts of the helix on the z axis.

A particular case of chirality, illustrated in Figure 11, is that present in helical structures like the ones present in chromatin. The object of our study is chromatin conformation and in particular the superstructures in its organization that give rise to scattering phenomena of circularly polarized light. Helical chirality is called an axial chirality since the difference in structure is based around the central axis of the helix and the different orientation the molecules follow around it.

The main parameters for the helix chirality able to influence the CIDS value in our results, both in magnitude and sign, are then:

- The Radius of the helix, indicating the furthest distance between the central axis and the helix structure;
- The Pitch of the helix, indicating the distance required for the helix to complete a revolution along the symmetry axis in a direction parallel to the axis itself;
- The handedness of the helix, indicating which of the two configurations (right or left) the structure has.

2. Chirality in Chromatin structures

Chromatin can be considered a negatively charged biopolymer [62] and is composed by the union of the genomic DNA and all associated proteins and RNA complexes [63]. As a consequence of its fundamental role in life and complex structure, it has been the object of study for a long time, particularly concerning its intricate structure [64]. Despite this, the debate is still ongoing on the exact structures and conformations that chromatin adopts in vivo, in situ or after extraction [65]. This is a consequence of its incredibly complex structure and function, leading to multiple levels of organization depending on the order of size examined. This is shown in Figure 12, which shows the different levels of organization. The smallest unit is the DNA, with a lateral size of about 2nm [66]. DNA is coiled around structures called nucleosomes, which are made of different histones in what is normally called the “beads on a string” model [67]. Histones are positively charged proteins and are subdivided in different categories depending on the function. In particular core histones form the core around which the DNA helix coils and the H1 histones are called linker histones and allow the coiling of DNA[63]. Nucleosomes have a scale of about 10nm and structures of this size have been identified in native samples by Small Angle X-ray Scattering (SAXS) measurements [68].

The next step in chromatin conformation is the 30nm chromatin fiber that has been the object of much debate among the scientific community. While some studies confirmed its presence inside unperturbed nuclei, others seem to not have confirmed its presence except after extraction of the chromatin from the nucleus. There are various structures proposed for the organization of the 30nm fiber, among which exist the solenoid and zigzag models, all of which present chiral conformations [62]. In solution, the state of the helix depends on the concentration of salts. The ideal technique to reveal these phenomena is electron microscopy, which has allowed to show the 30nm fibers of chromatin undergoing a passage in conformation [69]. The structure changes from a zigzag conformation of the linker nucleosomes in the middle of the fiber to a distinct contraction of the fiber, suggesting longitudinal folding, at ionic intensities exceeding 100mM [69].

It's evident thus that there are multiple levels of chirality involved in the structure of chromatin, ranging from the double helix scale of the DNA chain (2nm), to the 11nm coilings of the

nucleosomes, to at least the 30nm fiber size. In the following chapters we will explain how we can take advantage of such structures by studying the scattering part of the circular dichroism signal derived from their interaction with light.

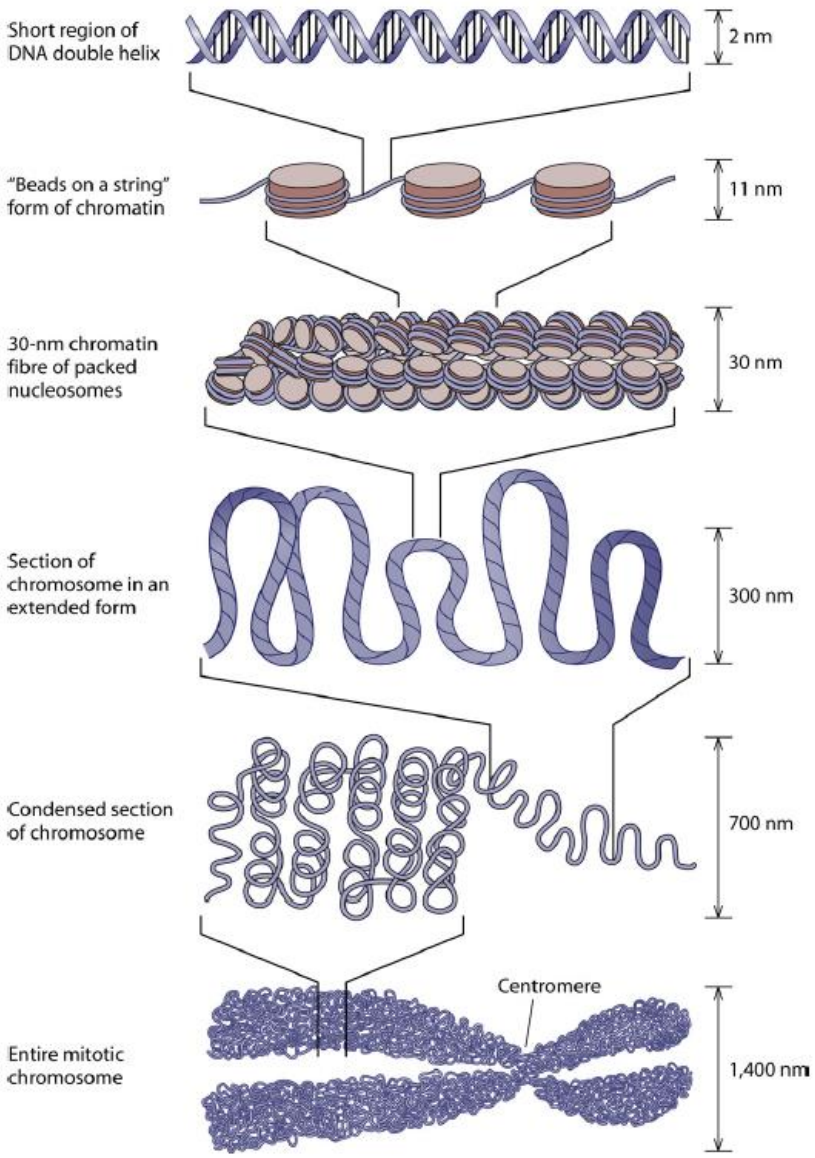

Figure 12 – The structure of chromatin across multiple scale sizes, ranging from the DNA double helix (2nm size) to an entire chromosome (1400nm size). Figure from [70]

3. Light Scattering

When light encounters a particle, it can interact elastically and be deviated by said particle in a direction different from the original one. This phenomenon is named scattering and the

probability of light to be scattered at any angle is dependent on various characteristics, including the particle's size [71] [72] [73] [74] [75] [76], shape [77] [78] and properties, like the difference of refractive index with the surrounding medium [72]. Light scattering techniques are noninvasive and able to measure isolated scatterers [79] [80], suspensions [73], aerosols [81] and impurities present in solid samples [82] [83]. For this reason, the characteristics of a sample can be studied by its scattering response, leading to many applications in the fields of nanoparticles [84], Lee et al 2017) or biological samples such as chromosomes [85] [86], spores [87], bacteria [87] [8] [78] [79] [80], red blood cells [87], the morphology of cells [88] [89] [90] [91].

Scattering signal is inherently angle dependent and this information can be retrieved either directly [74] [75] [91] or indirectly by use of Fourier transform analysis, by utilizing spatial and phase information to calculate the scattering pattern [92] [79] [80].

Two main regimens for light scattering can be determined depending on the size of the scattering particle compared with the wavelength of the incident light and are called:

1) Mie scattering, when the wavelength of the incident light is similar or greater in size than the scattering particle ($d \geq \lambda$);
2) Rayleigh scattering, where the particles are much smaller than the size of the incident wavelength ($d << \lambda$).

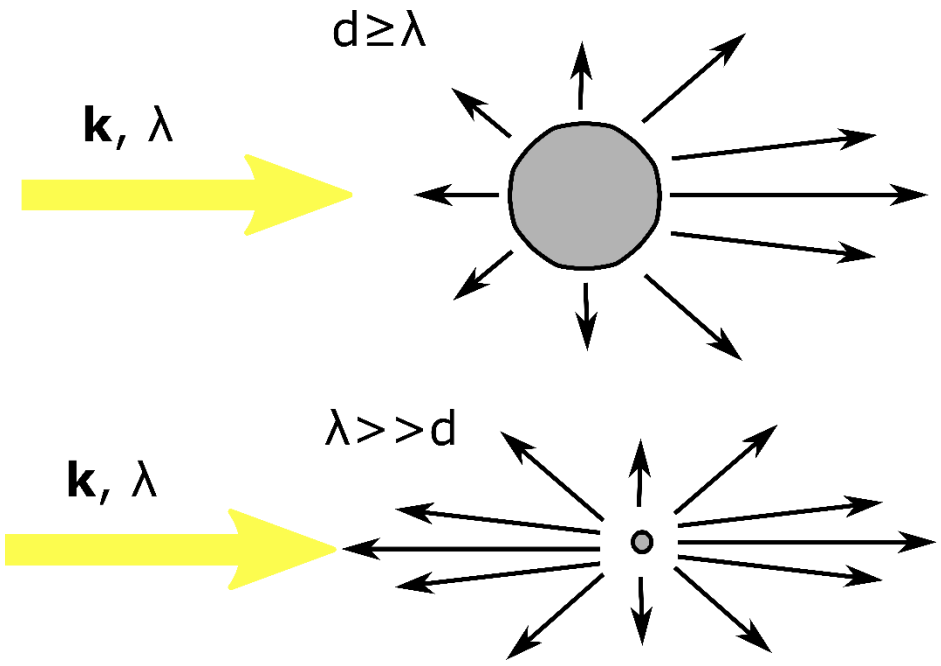

*Figure 13 – When light with wave vector **k** and wavelength λ hits a particle of diameter d≥λ (above), the Mie scattering limit is verified and scattering is mostly localized in the forward direction. When d<<λ (below), the Rayleigh scattering limit is verified and there is an important backscattering component.*

In Figure 13 both limits are illustrated. Mie scattering produces a higher intensity of forward scattered light compared to the relatively modest backscattering phenomenon (this property increases with the increase in size of the particle relative to the wavelength of light). On the other hand, Rayleigh scattering presents significant backscattering intensity.

Since biological structures like cells and nuclei have a size measured in tens of micrometers and the light utilized in microscopes is of the order a few hundreds of nanometers to a few micrometers, the Mie regimen is the one that is usually describing the interaction between the light and such samples.

4. Circular Intensity Differential Scattering (CIDS)

Circular Dichroism (CD) is the differential interaction of light that is polarized circular left and circular right with an object. This interaction can be of two kinds: the differential absorption, which corresponds to the classical CD and the differential scattering of the two polarization states, which is named Circular Intensity Differential Scattering (CIDS).

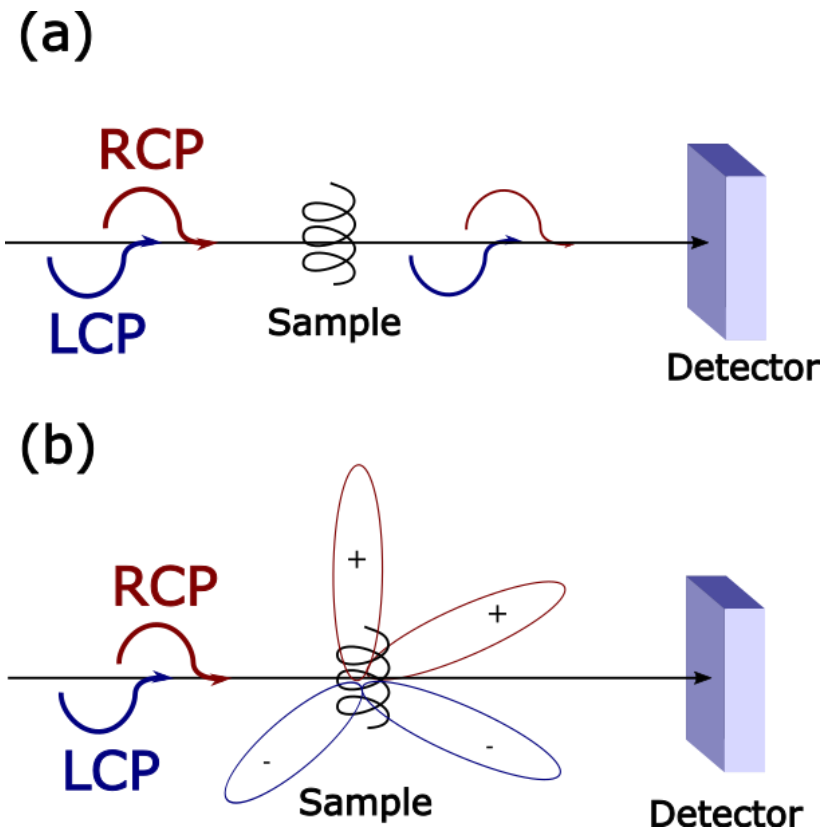

Figure 14 – The two main modalities of CD interaction with a sample: a) by differential absorption (normal CD) and b) by differential scattering (CIDS). RCP: Right Circularly Polarized light; LCP: Left Circularly Polarized light. In the first example, RCP and LCP light are absorbed in a different way in the forward direction, leading to a CD signal. In the second, the chiral sample produces a response whose sign and intensity dependent on the scattering angle.

The two effects are shown in Figure 14. In panel (a), the CD is shown: when light that is polarized circular left (LCP) and right (RCP) are incident on a sample presenting circular dichroism, they are absorbed with different intensity. In panel (b), the CIDS phenomenon is shown instead. This time, when the polarized light hits the sample, it is instead scattered at different angles depending on its polarization state. In general, both effects can be present at the same time, but CIDS presents a smaller intensity than CD and thus is better studied in opportune conditions, such as outside the absorption band of the sample or at angles different from the direct transmission. The first mentions of the CIDS signal appeared in the 1970s, where some studies proved that CD is not to be attributed solely to differential absorption effects, but also to a differential scattering component [93].

An interesting characteristic of the CIDS signal is that it has been shown to be sensitive to chiral structures of sizes down to $1/20^{th}$ the wavelength of the incident light [94], which allows it to obtain information normally hidden to conventional microscopy techniques [94]. Circular Dichroism has long been a known and solid technique to study chiral molecules and propositions and applications of CIDS analysis to biophysical chiral samples were quickly proposed from the start, in particular for structures like viruses [95] and chromatin [93] [96] [97]. The interest in chromatin applications has kept up through time, leading to more papers utilizing the CIDS technique in more recent times [98]. After the 2000s, a few works have been concerned with showing the dependence on wavelength of the polarimetric signal in the field of materials science and for chiral molecules in turbid media [99] [100] [101].

5. CIDS in solutions

The normalized circular dichroism of a sample can be defined by the following formula:

$$CD = \frac{I_L - I_R}{I_L + I_R}; \tag{54}$$

Where I_L and I_R are respectively the intensities measured for the left circular polarization and right circular polarization states. The term at the denominator is simply the sum of the total light, used as a normalization.

Following the previous equation, CIDS will then be described as:

$$CIDS(\theta) = \frac{I_L(\theta) - I_R(\theta)}{I_L(\theta) + I_R(\theta)}; \tag{55}$$

where all terms depend on the scattering angle θ.

A configuration of particular interest for CIDS, both because of its discovery from CD measurements in solutions and because it was how the first setups measured it, is the single-point spectroscopic measurement of solutions. We will see later in this chapter how we reproduced such a setup, but we will now focus on the theoretical description of the CIDS signal in this case, which was proposed by Bustamante et al. [94]. In particular, the focus is put on understanding the contributions of the absorption from the differential absorption coefficients a_L-a_R and the differential scattering coefficients s_L-s_R, separating thus the two contributions. To do this, the differential scattering cross section of the solute σ_L-σ_R will be utilized.

A description of the configuration for such a setup is given in Figure 15

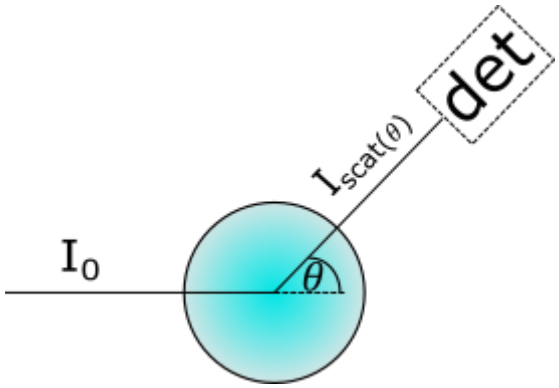

Figure 15 – The interaction of the incident light of intensity I_0 with a cylindrical cell containing a solution of the sample produces at each angle ϑ an intensity $I_{scat(\theta)}$ on the detector dependent on the angle ϑ and the distance r of the detector from the cell.

We start by defining the extinction coefficient for light passing through a solution. This is given by the Beer-Lambert law, which is as follows:

$$I = I_0 10^{-\varepsilon c l}; \tag{56}$$

Where I is the intensity of light after interaction with the sample, I_0 is the intensity before interaction, ε is the extinction coefficient, c is the concentration of the solution and l is the length the light has to travel inside the solution. The extinction coefficient is made of the contributions of both the absorption and the scattering of light. The intensity of scattered light on a detector

at a distance r from the sample will depend on the scattering cross section σ_R, a quantity only depending on the angle θ in the following way:

$$I_{sca}(\theta) = \sigma(\theta) I_0; \tag{57}$$

6. The directly transmitted beam

At this point, there are two main cases: the direct transmission, in which the signal will be determined by both the transmitted light and the light scattered at 0° and all other angles, in which the transmission contribution is eliminated and only scattered light is counted. This is the situation shown in Figure 15.

In the case of the transmitted beam, by combining the Beer-Lambert law with the previous equation, we obtain:

$$I = I_0 10^{-\varepsilon c l} + \frac{\sigma(0)}{r^2} I_0 10^{-\varepsilon c l}; \tag{58}$$

Where r is the distance of the detector from the cell. As previously stated, in CD (and consequently CIDS) measuring setups, the intensity I is measured in function of the difference of the left and right polarization states and is normalized by the sum of the total light. The previous equation can then be rewritten, after developing the terms on the right under the assumption that the CD is low, we obtain the formula:

$$\frac{I_L - I_R}{I_L + I_R} = -\frac{2.303}{2}(\varepsilon_L - \varepsilon_R) c l + \frac{\sigma_L(0) - \sigma_R(0)}{\sigma_L(0) + \sigma_R(0)}; \tag{59}$$

In this equation we have a separation in two terms. The first one is related to the attenuation of the light beam deriving from its extinction as it travels along the cell. It's important to remember that the extinction coefficient $(\varepsilon_L - \varepsilon_R)$ is dependent on both the differential absorption coefficient (a_L-a_R), but also on the differential scattering coefficient (s_L-s_R). This is because light is attenuated both by the absorption of the sample and the light scattered at angles different from the direct transmission.

$$(s_L - s_R) = \frac{N_0}{2.303}\int_0^{2\pi} d\varphi \int_0^{\pi} [\sigma_{sca,L}(\vartheta) - \sigma_{sca,L}(\vartheta)]\, sin\vartheta d\vartheta; \qquad (60)$$

The scattering coefficient in particular is connected to the integral over all angles of the angularly dependent scattering cross section.

The second part of the equation is related to light that is scattered at exactly 0° and will of course be dependent on the angular acceptance of the detector, and therefore in practical terms on its size and distance from the cell. A small and distant detector will reduce this coefficient as much as possible, but in other cases the sign of CIDS at 0° will be dependent on the experimental conditions.

7. The scattered beam

In the case of θ different from 0, the only contribution will be deriving from scattering, as the directly transmitted light is present only at 0°. While the light polarization will be circular only relative to the 0°/180° directions, the difference in absorption from the medium depending on polarization is considered negligible as it would be below 5% of difference [94]. In this approximation, the resulting equation describing the CIDS signal at any arbitrary angle will be:

$$\frac{I_L(\theta) - I_R(\theta)}{I_L(\theta) + I_R(\theta)} = -\frac{2.303}{2}(\varepsilon_L - \varepsilon_R)cl\left[\frac{(1 + cos\theta)^2}{2(1 + cos\theta)^2}\right] + \frac{\sigma_L(\theta) - \sigma_R(\theta)}{\sigma_L(\theta) + \sigma_R(\theta)}; \qquad (61)$$

Again two terms are present. The first one is related to the intensity attenuation of the beam due to the differential extinction (absorption + scattering) of the light travelling in the cell. The second one represents the differential scattering cross section at any angle. Since only the first term is dependent on the concentration c, by approaching c=0 the contribution of the second term can be isolated.

8. The effect of molecular parameters on CIDS

Following the calculations performed in [102] for randomly oriented scattering molecules, we can develop Eq. (60) by integrating analytically the scattering cross sections over all angles and we obtain that:

$$s_L - s_R = -\frac{4\pi^3 N_0}{2303\lambda^4}\sum_i\sum_j Re\left(\alpha_i\alpha_j^*\right)\left(\hat{e}_i \times \hat{e}_j \cdot \hat{R}_{ij}\right)\left[\left(\hat{e}_i \cdot \hat{e}_j f(a) - \left(\hat{e}_i\hat{R}_{ij}\right)\left(\hat{e}_j \cdot \hat{R}_{ij}\right)g(a)\right)\right]; (62)$$

Where a, f(a) and g(a) correspond to

$$a = -\frac{4\pi R_{ij}}{\lambda}; \quad (63)$$

$$f(a) = \frac{16 + 8(a^2 - 2)cosa + 2a(a^2 - 8)sina}{a^5}\ ; \quad (64)$$

$$g(a) = \frac{8(a^2 + 6) + 16(a^2 - 3)cosa + 2a(a^2 - 24)sina}{a^5}\ ; \quad (65)$$

In these equations:

- R_{ij} represents the distance between two polarizable groups i and j within the molecule and $\hat{R}_{ij}$ is the unit vector from i to j;
- λ is the wavelength of the incident light
- α_i and α_j are the polarizabilities of the two groups i and j, while $\hat{e}_i$ and $\hat{e}_j$ are the unit vectors of the axes of said groups;
- Re means that only the real part of the following expression is taken into account

From this expression we can see how the differential scattering coefficient is connected to the wavelength of incident light relative to the distance and position (chirality) of the molecular dipoles. The chirality plays a role in the function by the product of the unit vectors, while the distance is taken into account from the f(a) and g(a) functions. They approach zero as a approaches zero (meaning $\lambda >> R_{ij}$) or infinity (meaning $R_{ij} >> \lambda$), but can have positive or negative values for intermediate cases. Thus, the sign of the CIDS signal at a certain angle depends on these two factors, chirality [60] and distance of the structures.

The equation is very similar to the one found for the differential absorption coefficient [103]:

$$a_L - a_R = -\frac{16\pi^3 N_0}{6909\lambda^2}\sum_i\sum_j -Im\left(\alpha_i\alpha_j\right)\left(\hat{e}_i \times \hat{e}_j \cdot \hat{R}_{ij}\right)G_{ij}R_{ij}\ ; \quad (66)$$

Where $-Im(\alpha_i \alpha_j)$ is non-zero only when λ is within the absorption band. In this situation, from Eq. 62 and Eq. 66 the relationship between the scattering and absorption coefficients can be determined:

$$\frac{s_L - s_R}{a_L - a_R} = \frac{R_{ij}^3}{\lambda^3}; \tag{67}$$

This expression is valid only when $R_{ij} < \lambda$ and shows how when the distance between the chiral groups is too small, the absorption term is bigger, but as the distance increases up to close to the size of the wavelength, the scattering contribution quickly becomes more important.

Outside the absorption band, only the scattering contribution is present. For this reason, performing measurements outside the absorption band of the sample is a great way to measure the CIDS signal, but as it has been shown it's not a requirement as the CIDS signal is present at all wavelengths. CIDS signal will be low compared to absorption in this case though [104].

9. Modeling of CIDS signal from chromatin

As we have seen, theoretical studies on the origin of the CIDS signal arising from chiral scatterers were many across the years [102] [105]. Of particular interest for the scope of this thesis is the study of CIDS signal deriving from chromatin. In this context, the modeling of the structure was performed with two different methodologies: the Born approximation [102] [106] [107] and the discrete dipole approximation.

Many theoretical works have attempted to better define both the origin [105] of the CIDS signal and to give a quantification of the CIDS cross section [108]. In particular, various approximation methods were proposed to model the CIDS signal deriving from chromatin DNA, the first of which was the Born approximation [109]. This approximation does not take into consideration interactions inside the scatterers themselves and treats them as independent and ideal. The anisotropy is accounted for in a geometric way, for example by substituting the spherical scatterers with ellipsoidal ones.

Many theoretical works have attempted to better define both the origin [105] of the CIDS signal and to give a quantification of the CIDS cross section [108]. In particular, various approximation methods were proposed to model the CIDS signal deriving from chromatin DNA, the first of which was the Born approximation [109]. This approximation does not take into consideration interactions inside the scatterers themselves and treats them as independent and ideal. The anisotropy is accounted for in a geometric way, for example by substituting the spherical

scatterers with ellipsoidal ones. It is worth noting that for chromatin modeling, it is not possible to ignore the interactions between each nucleosome that are dependent on the different levels of compaction of the structure [110].

A second approach to theoretical modeling is the Discrete Dipole Approximation [111] [112] and the ADDA code [113]. Here, each scattering element is divided in a collection of discrete point dipoles that interact with each other. The minimum number of dipoles to correctly model an object is dependent on the refractive index. By utilizing the Lattice Dispersion Relation (LDR), the polarizability of each punctual dipole has been calculated [114] and measured with reasonable agreement in the X-Ray region [115]. Mueller matrix elements can be calculated in a set of scattering angles with the theory presented by Bohren [116], where an orientation averaging is done over Euler angles to take in consideration the random 3D distribution of scatterers inside the whole considered volume. DDA has been shown to be a numerically exact method [117] and has shown a great success in many fields, spacing from biophysics [118] [119] [119] to plasmonics [120].

10. Single-point CIDS setups

After explaining the theory of CIDS measurement, we will now illustrate the practical setups and applications that have been produced in literature. The first and most common CIDS application was the spectroscopic one-point measurement configuration, in which a certain portion of the sample is illuminated and the response from the whole volume is collected either spectrally (in function of the excitation wavelength) [121] or angularly (in function of the scattering angle) [122]. The first application of such setups was to study biological macromolecules aggregates [103]. As time passed, applications to numerous more systems like viruses [95], erythrocytes [123] and DNA aggregates [124] were developed. This led to the rise of commercial systems based on this principle [125].

This configuration is born from earlier CD measurement techniques, where particles of the sample of interest were suspended in an aqueous solution. This system was illuminated by a light source and the signal from the whole illuminated volume was collected.

Thus, due to its similarity to CD measurements, the first CIDS based experiments used similar setups to the commercial CD ones, simply trying to increase the signal to noise ratio to maximize the low scattering signal [28]. The main difference was the interest in the scattering signal, which required a detection capable of revealing it in function of the angle.

There are two main different one-point CIDS measurement modalities:

- Spectral measurement: the main information comes from the spectral response relative to the wavelength;

- Angular measurement: the response of the system is captured at different angles, giving a more complete information of the CIDS evolution in function of the angle.

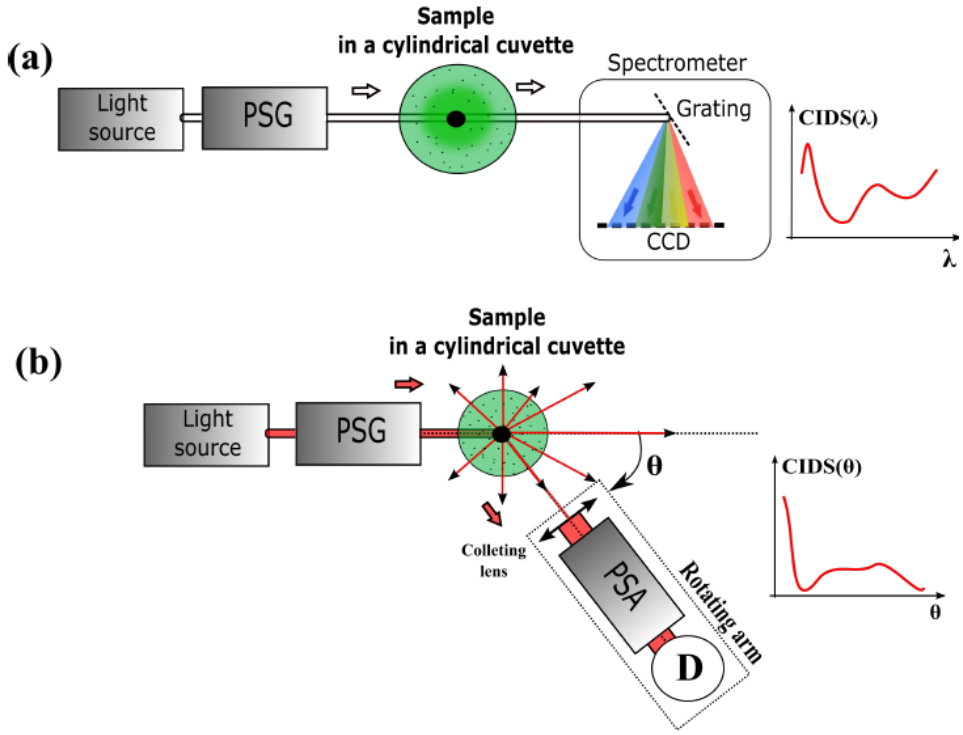

Figure 16 – The block diagrams of one point CIDS experimental setups, in particular a) spectral and b) angular measurements. PSG: Polarization States generator; PSA: Polarization States Analyzer; ϑ: scattering angle; LA: Lock-In Amplifier; D: Detector. Figure reproduced from [126].

As shown in Figure 16 (a) we have the general schematics of a spectral measurement setup. The signal is detected at or close to 0° of incidence, integrating only over a small angle. The information thus is about the CIDS limited to that angular aperture, visualized in function of the wavelength to obtain spectral information. This method was utilized for various biological applications thanks to the ability of CIDS to identify different conformations and structures in a fast way. For this reason it was utilized for example to identify different kinds of viruses and bacteria [127]. Another application was to analyze the diameter of microorganisms in a mixed suspension medium [128]. The sensitivity of CIDS to chromatin structures allowed it to be utilized also on complex systems like cells: as an example, it was used in the identification of the cell phase in Chinese Hamster Ovary cells [122] by comparing the CD and CIDS signal.

Another field where CD/CIDS excelled at was the study of photosynthesis and the pigmentation of plants, to allow to better understand the pigment protein complexes and their interactions [129]. Moreover, polymer and salt induced aggregates (called also psi-type aggregates) like the ones found in chlorophyll were studied in conjunction with DNA samples and showed the

presence of the CIDS signal outside the absorption bands [130] [131], which allowed to better comprehend the energy bonds inside the nucleus. In the field of pigmentation study, the spinach chloroplasts was used as a model to compare simulations and measurements of CIDS on a chiral object, to better understand the signal deriving from the radius and pitch of each structure [132]. More recently, CD was utilized on chloroplasts to as a way to remotely (up to a few kilometers) recognize such molecules [133].

Concerning the angular measurement modality for CIDS, a general setup scheme is shown in Figure 16 b). As can be seen, the setup is similar to the spectral one, with the addition of a rotating mechanical arm which allows the detection to be moved around the sample to collect data at different scattering angles. This modality was also utilized to great advantage in biophysical studies, in particular on chromatin conformation. The study of DNA is usually performed in the liquid-crystalline conformation in aqueous solution [134] after the creation of microscopic aggregates that change its compaction and structure, making it ideal for CIDS study. The DNA condensation can be induced in various ways, including alcoholic solutions [124] and dehydration [28]. Different DNA extraction protocols from rat hepatocytes were compared by angular CIDS analysis and to determine the method that better preserved the original DNA configuration [98] [8] and data was compared differential calorimetry [135]. The findings showed that the extraction method greatly influenced the CIDS signal, making interpretation of the compaction level of DNA difficult. For this reason, the main application of CIDS was in theoretical works, which have nonetheless helped in better understanding the organization of nucleic acids [105] [136].

Part 2: One-point spectroscopic CIDS of isolated nuclei

1. Single-point angular CIDS

During the work of my thesis I have contributed to the development and validation of an angular measurement single-point CIDS setup. The setup is pictured in Figure 17.

The light source is a green diode laser producing light at 550nm, which is consistent to the fact that our scattering samples exhibit an absorption inferior to this excitation wavelength. First, we have the PSG, constituted by a linear polarizer followed by a photoelastic modulator. The light then passes through the sample (contained in a round cuvette) and then the PSA, which is this time composed by a simple linear polarizer. After this a rotating wheel, controlled by a motor with both automated and manual controls, houses different Neutral Densities (NDs) that can be changed as needed by rotating the wheel. Finally, the beam reaches the PMT which serves as detector. The final part after the sample (PSA, OD wheel and PMT detector) is mounted on a motorized arm that can rotate around the sample's axis, performing a complete revolution around it. The actual angle of movement is limited by the presence of the optics in the setup but is still at least 180°, centered on the direct transmission from the laser to the sample.

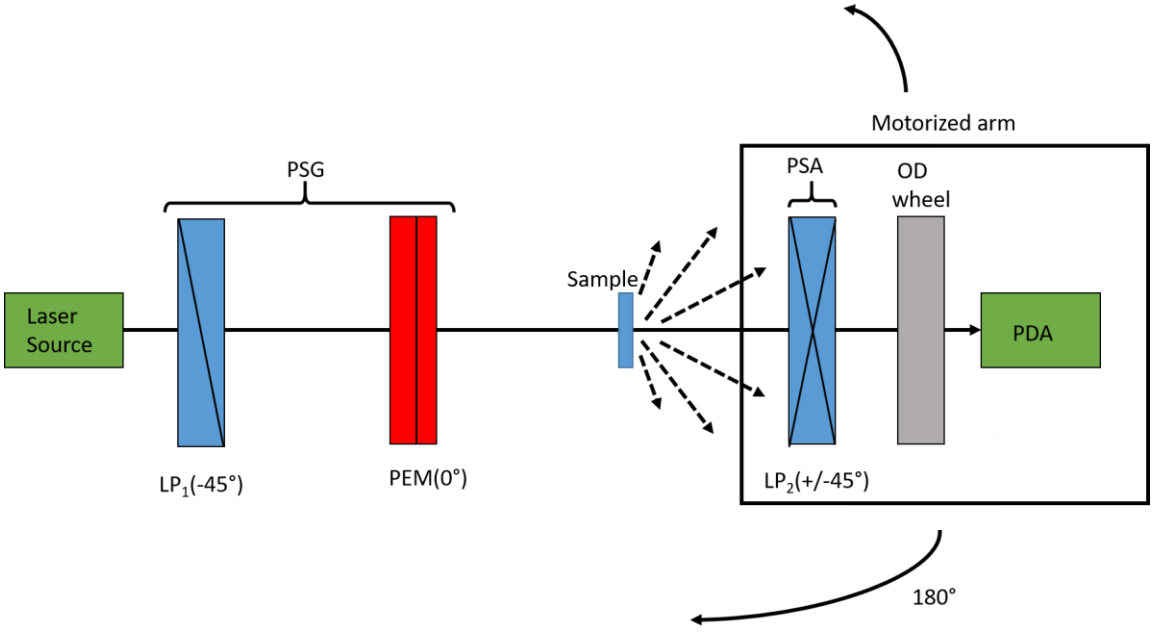

Figure 17 – The custom angular spectroscopic CIDS setup, as it was built during this work.

The sample is composed by a circular cuvette containing a water solution of the desired particles (microspheres, molecules, cells etc.).

2. Measurement procedure

The measurement is performed in three steps:

- Offset
- Air measurement
- Sample measurement

In the first step, the light source is covered and a measure (with no angular movement) is conducted to obtain the base signal without the laser. This data is relative to the signal due to ambient light and base signal of the PMT and can be used to take into account the external light situation of the laboratory, as long as the situation doesn't change during the measurement, allowing to work in different light conditions. In the second step, the shutter is removed from the laser's path and a measurement for the signal at 0 degree is taken without the sample. This operation provides the baseline for signal without the sample and allows to prove the correct functioning of the setup by measuring the well-known and reproducible signature of air. In this way, the possible misalignment of optics and polarization elements inside the setup can be registered and taken into account.

Measurements are also taken with a cuvette filled with water but no sample inside. In this way, effects such as the scattering of the sample due to the water or the edge reflections in the cuvette can be taken into account. The cuvette should be cylindrical to avoid reflections as much as possible and avoid that the angles at which the signal is registered change due to the relative angles of the surface of the cuvette relative to the scattered light. In fact, by consequence of the geometry and the refractive index mismatch between air, glass and water, a squared cuvette would cause problems of change in the scattering angle due to reflections.

Finally, the cuvette sample is positioned inside the holder and a measurement is started. The measurement process is completely automated. A labview routine controls the motorized parts of the setup, which are the rotation arm upon which the detection part is located and the rotating wheel containing the neutral densities utilized to scale the signal at different angles. In this way, during the measurement process the arm starts from -90° angle and moves by the amount set in the program, taking a measurement at every step. It also takes care of setting the correct ND for every angle. This parameter has also to be set by the operator and can differ depending on the sample and its scattering parameters: a strongly scattering sample may require higher NDs at higher angles than a lower scattering sample. In general, the effect of NDs is to uniformly reduce

the light intensity, without a dependence on wavelength or other parameters. The reduction is not linear, but follows the law:

$$\frac{I}{I_0} = 10^d; \tag{68}$$

Where I is the intensity of light after passing through the filter, I_0 the intensity before the filter and d is the Optical Density of the ND. Thus, if a measurement is made with a defined optical density, the value of intensity that would have been measured without the OD is:

$$I_0 = \frac{I}{10^d}; \tag{69}$$

Since the relationship between the OD and the measured light is logarithmic, we can obtain comparable measurements even for dynamical changes in Intensity much bigger than the ones that can be measured by the range of the detectors utilized.

Angle	OD value
0°	5.5
10°	3.6
20°	2
30°	2
40°	1
50°	1
60°	1
70°	0
80°	0
90°	0

Table 4 – Example of optical densities used for the angular CIDS measurement of microspheres in our setup. The negative angles (-10° to -90°) have the same ODs as the positive ones of the same absolute value.

In Table 4 an example of the ODs used for such a measurement (in this case of a sample of a water solution containing polypropylene microspheres). Since the Intensity is reduced in an exponential way, we can see how there is a difference of 5 orders of magnitude between direct transmission measurements and high angle ones.

The time needed for a measurement with this setup depends on the number of measurements taken, which depends on the angular step chosen by the operator. To make a measurement every 10° on a 180° total angle, the average time is about 15 minutes.

It's worth noting that the measurement order (offset, air and sample) is not a necessity and the order of execution of all three steps can be arbitrarily exchanged, as long as the external conditions do not change. The same offset and air measurements can be utilized for multiple consecutive experiments also in the same conditions.

3. Data treatment

To treat the data, a custom Mathematica program was utilized. From the error in the air matrix, the error in the measurement (coming from misalignment in the optics of the setup) can be deduced. If the error is particularly high, the setup needs to be realigned before proceeding with the measurement.

The extraction of Mueller coefficients needs to be made mathematically by utilizing the Fourier analysis of the intensity signal measured by the detector. The mathematical method implemented in this program has been explained in Chapter 1, Section 4 of this work. The setup there described corresponds to the one utilized here. As explained, this kind of setup allows the extraction some of the elements of the Mueller matrix: m_{00}, m_{02}, m_{03}, m_{22} and m_{23}.

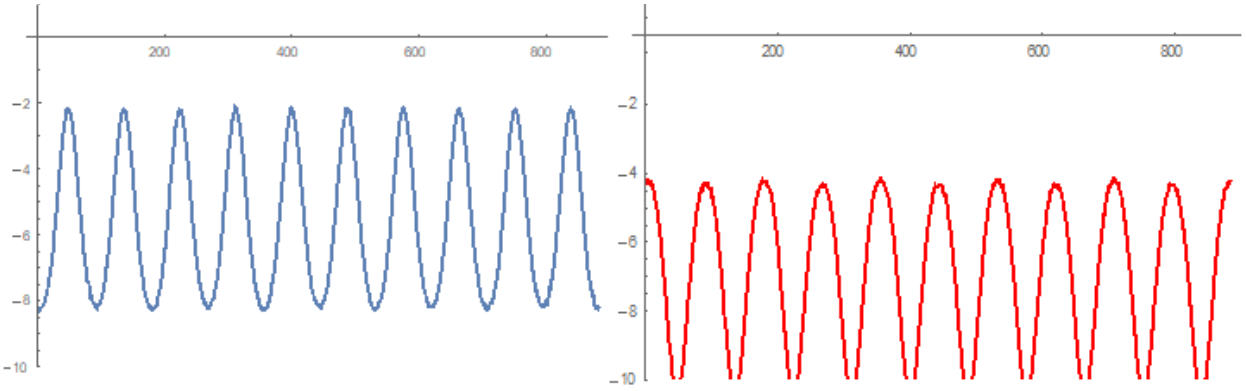

Figure 18 – The raw data for the air measurement in the angular CIDS setup.

The measurement time is long enough to include about 10 periods of the modulated intensity signal at the detector. This allows the measurement to be more precise by averaging over more periods and thus measurements. In Figure 18 we show this in a measurement for air, with 10 periods of the intensity present. This particular measurement resulted in the following calculated matrix (x elements are not measured in our setup):

$$M_{air} = \begin{bmatrix} 1 & x & 0.014 & -0.003 \\ x & x & x & x \\ x & x & 1 & -0.026 \\ x & x & x & x \end{bmatrix}$$

Whereas the expected Mueller matrix for air is

$$M_{air} = \begin{bmatrix} 1 & 0 & 0 & 0 \\ 0 & 1 & 0 & 0 \\ 0 & 0 & 1 & 0 \\ 0 & 0 & 0 & 1 \end{bmatrix}$$

The matrix is normalized, therefore the numbers correspond to the percentage of error in the measurement of every coefficient.

4. Calibration with Linear Polarizer

To characterize the performance of the setup, a linear polarizer was utilized as a sample. The LP was rotated and every 10° a measurement was taken with the setup. In Figure 19 an example of a measurement for the PSA linear polarizer at +45° and -45° respectively.

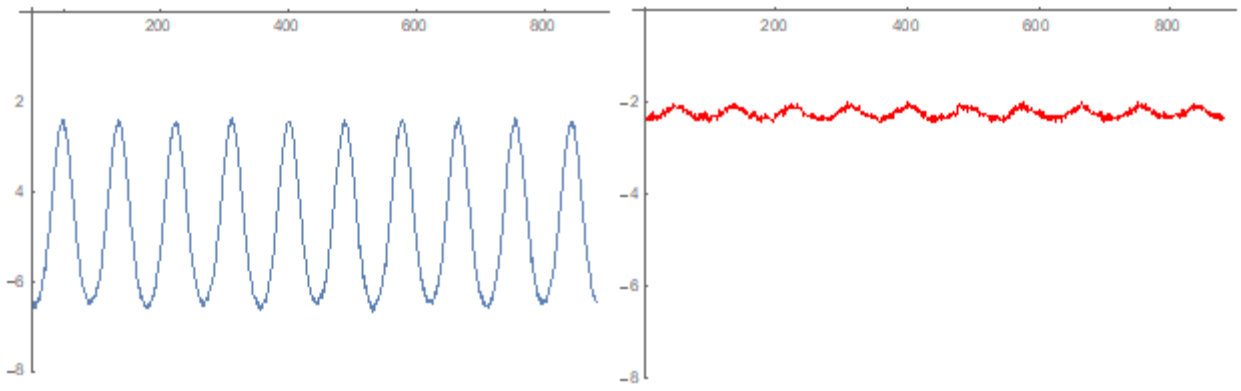

Figure 19 – The raw signal data as measured by the detector at 150° for the two orthogonal orientations of the linear polarizer in the PSA.

The measurement is taken at 150° of rotation from the initial position of the LP (not necessarily corresponding with a particular alignment relative to the optics of the setup). As with air, we have 10 period peaks in the measurement, as can be seen in the Fourier analysis made in Figure 20, where signal at peaks located at multiples of 10 is seen (up to the second harmonic, after which signal is too low to measure).

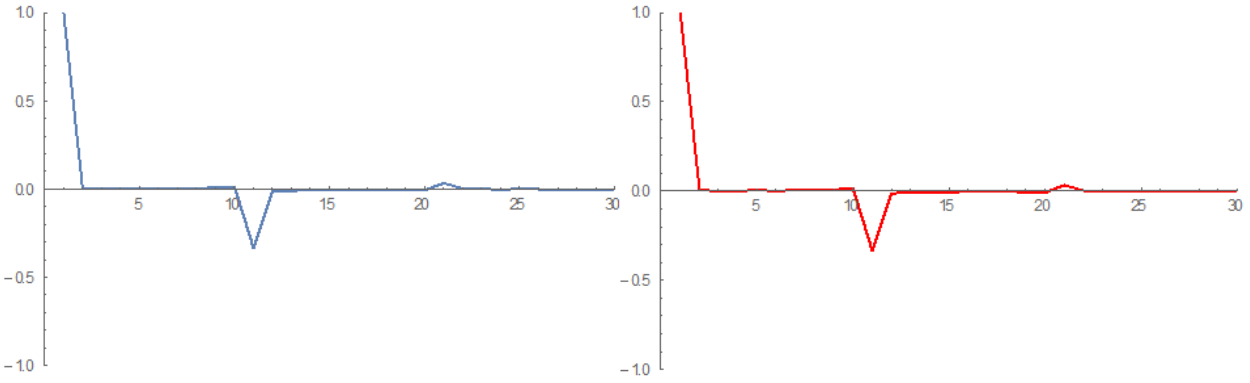

Figure 20 – The peaks relative to the Fourier transform of the signal in Figure 19.

From here, the signal extraction is executed with the methodology and calculations explained in chapter 1.

The theoretical response of the LP is calculated by simulation of the Mueller setup in the Mathematica program and compared with the experimental results. This is shown in Figure 21, demonstrating the good degree of accordance between theory and empiric measurement, especially for the m_{03} element, corresponding to CIDS. The average value of m_{03} is 0,004, with a standard deviation of only 0,014. Since the a linear polarizer is an optical object especially constructed to only present linear dichroism, its expected circular dichroism is 0 and thus the expected value of m_{03} is also 0, which is in accordance with the obtained measured value.

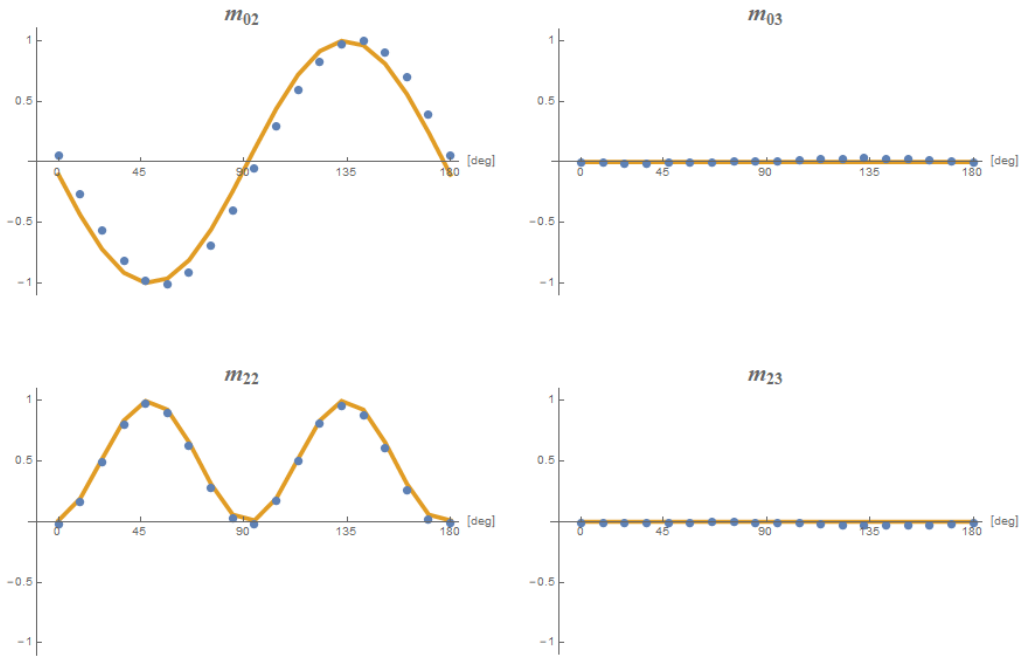

Figure 21 – The m_{02}, m_{03}, m_{22} and m_{23} elements of the Mueller matrix in direct transmission on the angular CIDS setup for linear polarizer in function of the angle of rotation. Blue dots represent measurements, while the orange lines represent the theoretical values.

5. Angular CIDS on arabinose

Arabinose is a molecule belonging to the family of saccharides. In particular, it's an aldopenthose, a monosaccharide which contains a CHO (aldehyde) group. It is a chiral molecule and can be found in two configurations, L-Arabinose and D-Arabinose, shown in Figure 22.

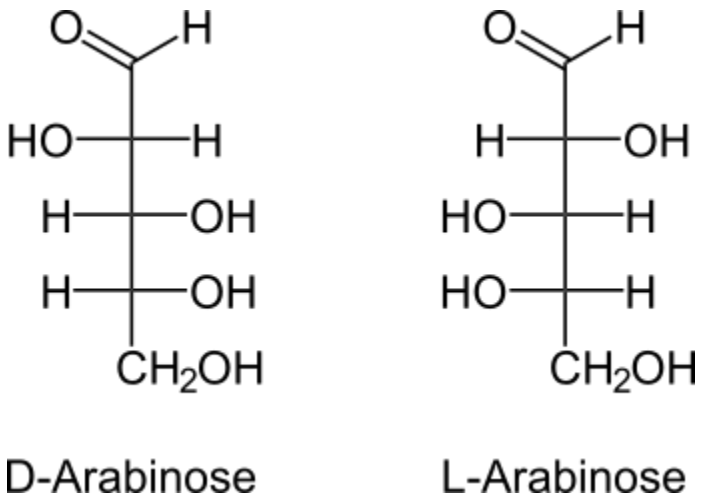

Figure 22 – Arabinose structure for the chiral forms D-Arabinose (left) and L-Arabinose (right).

Arabinose is known to present circular dichroism signal, owing to its chiral structure. For this reason, it's an ideal sample to test the sensing capabilities of our setup. Thus, solutions of D-arabinose were produced by simply dissolving the powder form of D-arabinose in water at the desired concentration and putting the resulting solution inside a cuvette. The process was repeated for all concentrations needed. Knowing that the brute formula of arabinose is $C_5H_{10}O_5$, it follows that the molecular weight is 150.13 g/mol. To create a 1M solution then, this quantity of arabinose needs to be dissolved in water until the final solution has a volume of 1 liter. I prepared and measured the angular CIDS signal of solutions at different concentrations of D-Arabinose. This level of concentration is very high, but was used in this work simply to obtain a strong scattering signal to validate our approach in a clear and easy way. I also prepared a solution of polystyrene microspheres (10^5/L concentration) that was utilized as a control sample.

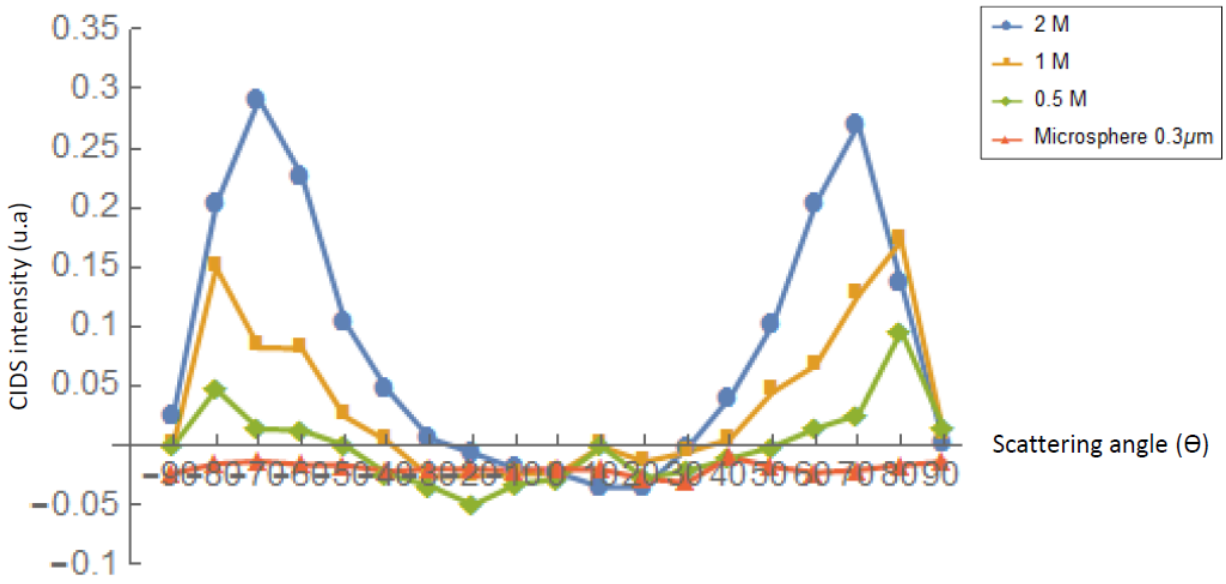

Figure 23 – Measurement of the angular CIDS signal for different water solutions: 0.3 μm polystyrene microspheres (red), and D-Arabinose in 0.5M (green), 1M (yellow) and 2M (blue) concentratons.

The results for the various samples can be seen in Figure 23. It can be noticed that the microspheres sample doesn't present any features in the CIDS signal depending on the angle, presenting instead a homogeneous small signal corresponding to the baseline of the measurement. This value can be simply used to subtract the baseline from other measurements and find the real zero of the setup. It arises from small internal misalignments within the optics and can be recognized by its lack of angular features. This same baseline is found in the arabinose samples at angles close to 0° of scattering. Peaked features can be found for the D-Arabinose

samples at angles higher than +/- 30°. In particular, the intensity is dependent on the concentration, linearly increasing with it.

6. Angular CIDS signal in isolated nuclei

Measurements were also performed on isolated HEK cells nuclei. The nuclei were isolated by centrifugation and suspended in a water solution. The nuclei samples were compared once again to polystyrene microspheres samples. In this case, the microspheres represent a good control sample as they have a similar size to the nuclei (around 15 µm), with the marked differences of the shape and chromatin content, and thus the presence of chiral structures.

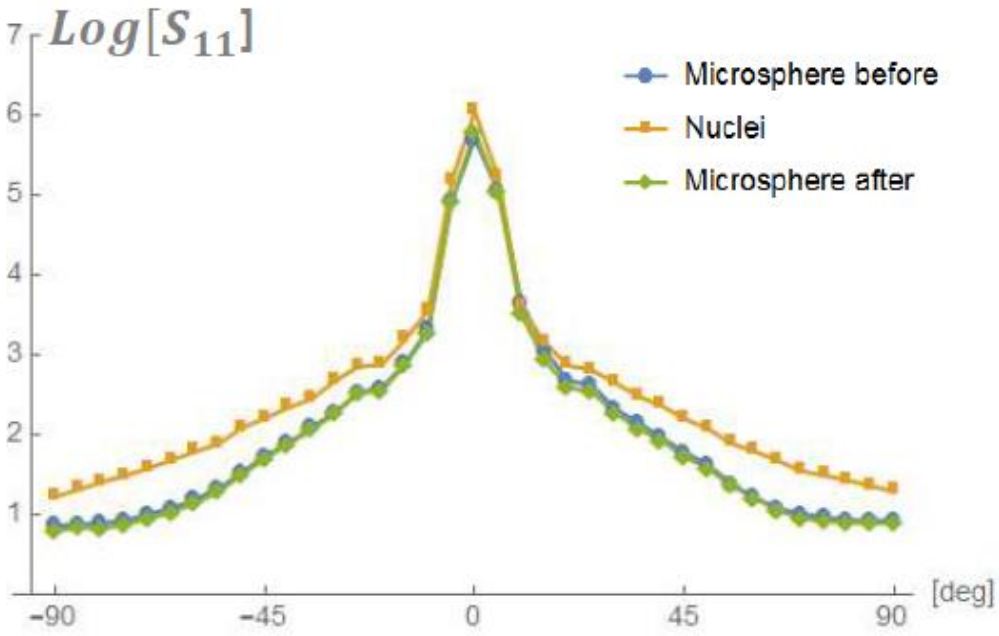

Figure 24 – m_{00} element of the Mueller matrix in function of the scattering angle as measured in our angular CIDS setup for nuclei (orange) and microspheres solutions before (blue) and after (green) the nuclei measurements.

In Figure 24 the m_{00} element of the Mueller matrix, corresponding to the total transmission is shown. As expected in the Mie scattering limit, the measured light intensity is maximum at lower scattering angles and decreases as the angle increases. Since the scale is logarithmic, the central peak is very strong and corresponds to the directly transmitted beam. The same microsphere sample has been measured before and after the Nuclei sample to demonstrate the stability of the setup. The difference in shape of the m_{00} element features can thus be attributed entirely to the different scattering power of the nuclei related to the microsphere samples.

Furthermore, in Figure 25 the results for the m_{03} element of the Mueller matrix, corresponding to CIDS signal, is shown. From this figure it is clear how the nuclei present a distinct signal in CIDS as opposed to the absence of signal in the microsphere samples. As previously explained, this is expected and attributed to the chiral structures of chromatin contained inside the nuclei and

absent in the microsphere sample. The measurements represent an average of 6 different experiments and thus provide a statistically relevant result.

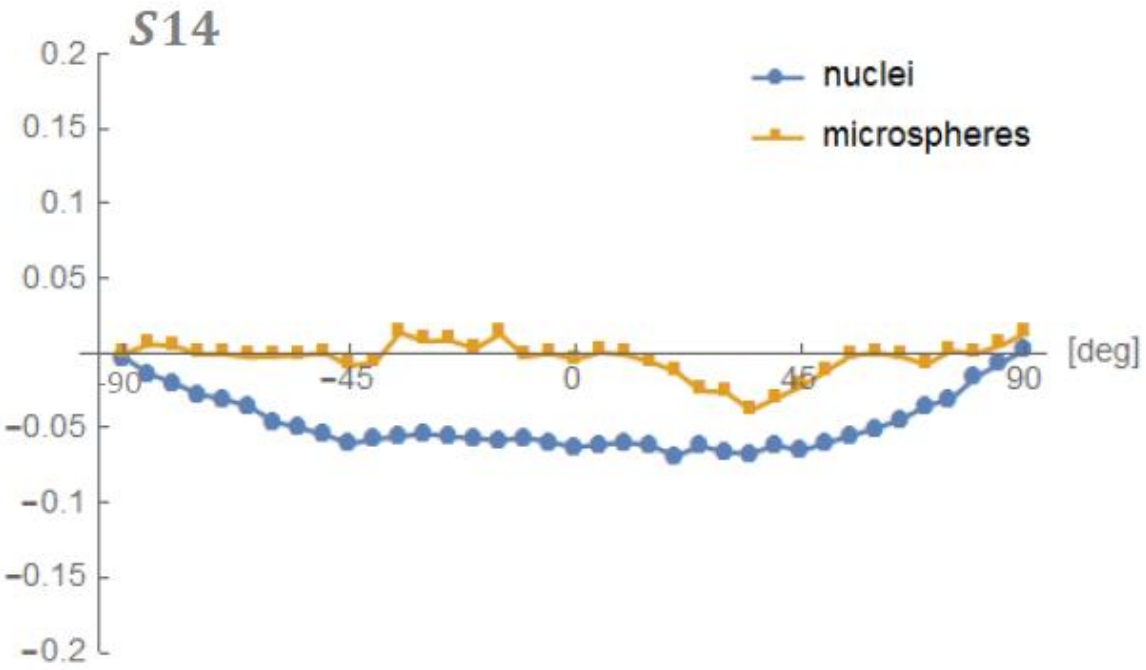

Figure 25 – m_{03} element of the Mueller matrix (corresponding to the CIDS signal) for a solution of nuclei (blue) and microspheres (orange).

Part 3: Light scattering microscope

1. Fourier Imaging

The CIDS measurement setup described in the previous section has the ability to give the angular information relative to the sample in a simple way, but the measurement speed is limited by the need for the physical movement of the detector with the motorized arm for a complete angular scan. This leads to measurements of the order of minutes, and while it could be optimized by utilizing the fastest possible speeds of rotation and a perfect synchronization between measurements and movement of the arm, the scanning would still require tens of seconds. Furthermore, this configuration required an optical densities wheel to obtain the information at all angles due to the drop in light intensity at higher angles. For this reason, we decided to adopt a new approach that would allow us to obtain angular information on the sample by utilizing the principle of Fourier imaging. Both the light that is directly transmitted through the sample and the scattered light are collected at two different planes of focus to obtain the real space and Fourier space images relative to the sample in question. Other setups of this type have already been utilized to study samples of microspheres [137] and more complex biological structures, such as chromosomes [86]. As shown in Figure 26, the image generated from such a system in the Fourier plane represents the θ and ϕ angular scattering distribution of the light intensity and thus the resolution will be expressed in degrees per pixel rather than nanometers or micrometers per pixel. Each pixel will then correspond to a certain angular acceptance depending on the angle of acceptance θ_{acc} of the condenser utilized to image the sample and the number of pixels of the camera used as detector.

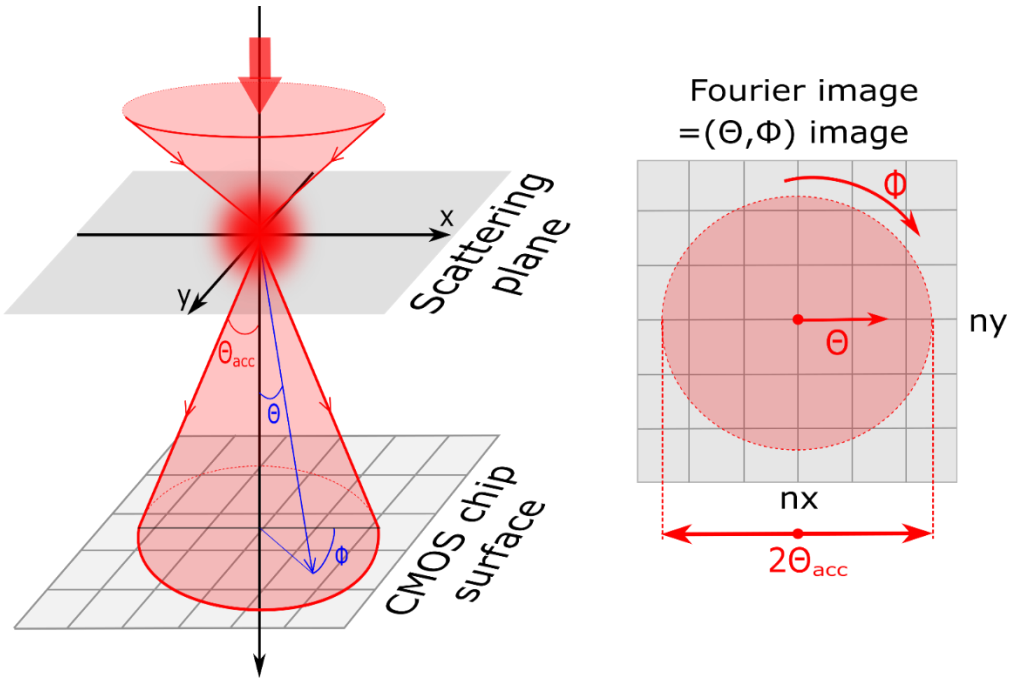

Figure 26 – The light scattered by the sample can be imaged in the Fourier plane by a camera, creating an angular image where the FOV corresponds to the acceptance angle of the objective.

2. The Light Scattering Microscope setup

The setup utilized for this kind of measurement is a completely custom microscope I have built and aligned. The setup is pictured in Figure 27.

The light source is a He-Ne laser that emits monochromatic light at 633nm. The light passes through a beam splitter and is sent by mirrors to a beam expander. This component is made by multiple lenses and has the role of expanding the laser beam. This passage is needed to fulfill the whole aperture in the objective placed after the sample as collector, so as to create a homogenous FOV in the instrument. Finally, the light reaches the sample, which is positioned on a stage that can be moved along the x, y and z axes. Here it interacts and is therefore divided in two rays, as shown in the schematics of Figure 28. In this picture we can see in green the path of the transmitted light, while in red we have the path of the scattered light resulting from interaction with the sample. The light then passes through a system of lenses that has the role of separating the transmitted light from the scattered light. A beam splitter then splits the beam in two parts, the first hitting a detector positioned at the real plane and thus recreating a real image, while the second is sent to another identical detector set in at a distance such that it will image the Fourier plane.

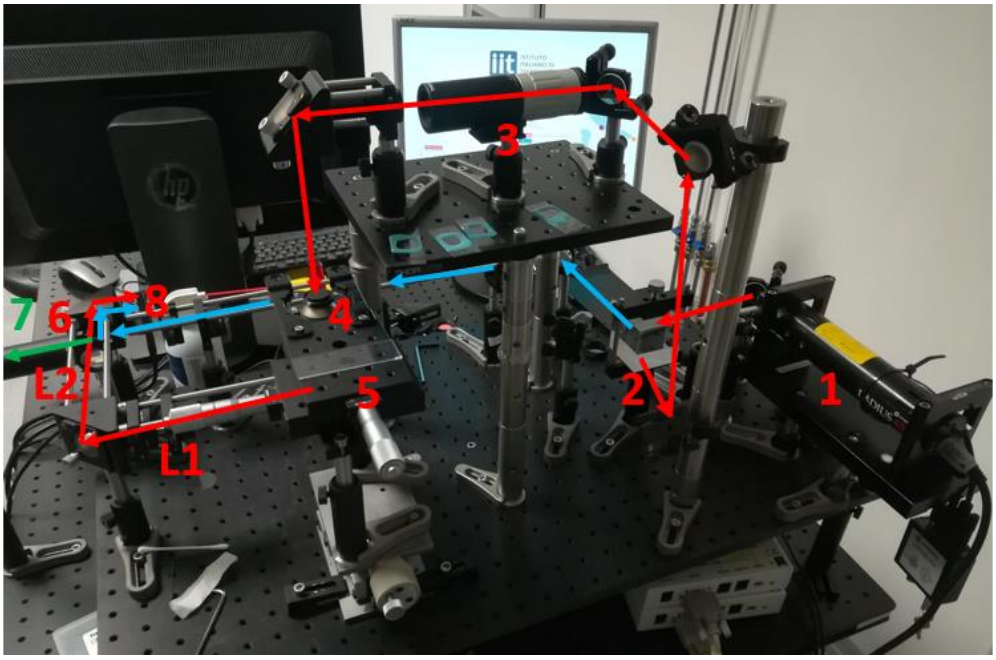

Figure 27 – Picture of the Fourier imaging setup. 1) He-Ne Laser; 2) Beam Splitter; 3) Beam Expander; 4) Sample holder and objective; 5) sample stage controls; 6) Beam Splitter; 7) and 8) CMOS cameras; L1) and L2) Lenses. Red arrows indicate the light path in the Fourier imaging setup, green for the real image, blue for the couple

In red the path of the illumination beam and Fourier image. In the green the real image (separating at the 6 beam splitter). In blue, an alternative light path to possibly implement other techniques in the future. The light beam from the diode laser source is expanded and shined in transmission on the sample (without focusing by any objective, simple collimated light), where it's collected by an objective (condenser). There are two lenses in the collection part of the setup (after the objective) as shown in the schematic below:

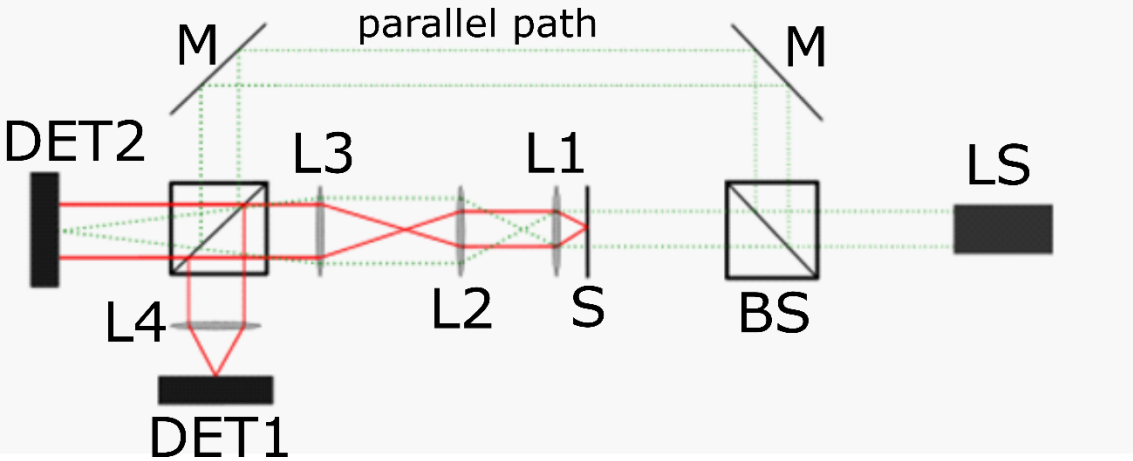

Figure 28 – Setup schematics for the Fourier imaging setup. LS: Light Source; BS: Beam Splitter; M: Mirror; LX: Lens X; DET1/2: Detector 1/2.

The green dashed lines represent unscattered light, while the red ones represent the scattered light from the sample. A pinhole can be added after L2 to select only a very small part of the field of view (depending on the size of the pinhole itself) and cutting some of the unscattered light, improving sensitivity to the desired signal. This allows for example to restrict the FOV to only one particle.

Polarization control can be implemented in a simple way by adding the same polarization optics of the angular setup in the light's path, meaning a linear polarizer and a photoelastic modulator in the PSG (before the sample) and two linear polarizers for analysis in the PSA after the sample. The mathematics relative to the extraction of the information relative to the CD/CIDS can be found in the previous chapter.

3. Calibration and data analysis

The simplest way to obtain an estimation of the angular resolution per pixel is by calculating it from the numerical aperture of the objective utilized, assuming the imaged area and the camera chip area correspond. In this case, by utilizing for example a 4X air Objective (0.10 NA), we will obtain:

$$2 * \theta_{\max} = \theta_{\mathrm{acc}} = 11.46° \tag{70}$$

Where θ_{acc} is the total angle of light collected by the objective and

$$\theta_{\max} = \mathrm{asin}\left(\frac{NA}{n_{obj}}\right); \tag{71}$$

Since the number nx of pixels in x of our cameras correspond to 1280px, the resulting pixel resolution in these conditions will be 0.00895°/px. This method assumes a good correspondence in the light beam size with the detector chip size. If this is not entirely true, another methodology can be utilized.

4. Calibration with grid samples

Figure 29 – Thorlabs R1L3S3P Grid Distortion Target, presenting 10, 50, 100 and 500 µm step grids.

A Thorlabs R1L3S3P - Grid Distortion Target (pictured in Figure 29) was utilized to calibrate the setup more accurately by using the values deriving from a known object with controlled features. In particular, the two 10 and 50 µm spacing square grids.

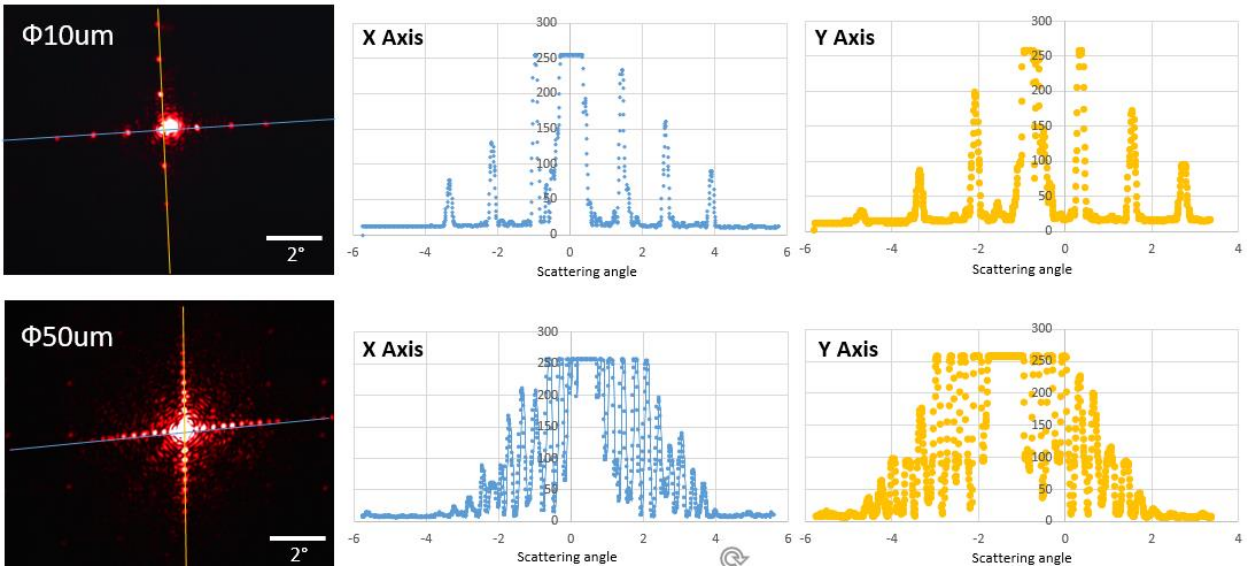

Figure 30 – (Left) The Fourier images of 10 and 50 µm spacing grids in the pLSS setup. (Right) The line profiles corresponding to the lines in the left pictures, to calculate resolution in the x and y axes. The central spot appears more undefined because it contains the transmitted unscattered beam.

In this case, Bragg's law can be utilized:

$$n\lambda = 2d\sin\theta; \quad (72)$$

Where λ is the wavelength (633nm in our case), d is the size of the steps (ex. 10 and 50 μm) and n is the distance between two different peaks in the image. To increase the precision of our system, we have taken multiple peaks and made an average of their distance to obtain a better estimation of their separation. Thus, an experimental calibration result can be taken by the formula:

$$\theta = \operatorname{asin}\left(\frac{m * \lambda}{d * 2}\right); \quad (73)$$

Where m is the number of orders taken. In our example, with the 50 μm grid, m=9 for 382 pixels, and thus θ=3.27° for 382 pixels, leading to a calibration value of 0.0086°/px

The results extracted like this can be utilized to calibrate the images for the same objective collector by inputting the angular value in imagej.

5. Microsphere results

A more interesting sample is composed by microspheres in a water solution. This sample is ideal to be modeled with Mie scattering and thus to be compared with theory easily. For these reasons, they're ideal to understand the setup and to use as a base for future comparisons with nuclei solutions.

As shown in Figure 31, the sample made of microspheres is hit by an incident light, which creates scattered light. The cone of scattered light leaving the sample contains concentric round shapes and in particular a central disk shape of luminosity called the Airy disk.

Depending on the concentration of microspheres, they can be easily isolated (at about 10^4 microspheres/mL) or we can obtain an image relative to multiple spheres (10^5/10^6 concentration). In the first case, to obtain a distinguishable enough signal to noise ratio, the FOV of the microscope needs to be artificially restricted with a pinhole at L2 to be only slightly bigger than the single microsphere. Measurement can happen in the full FOV for concentrated microspheres instead, which is the condition we utilized.

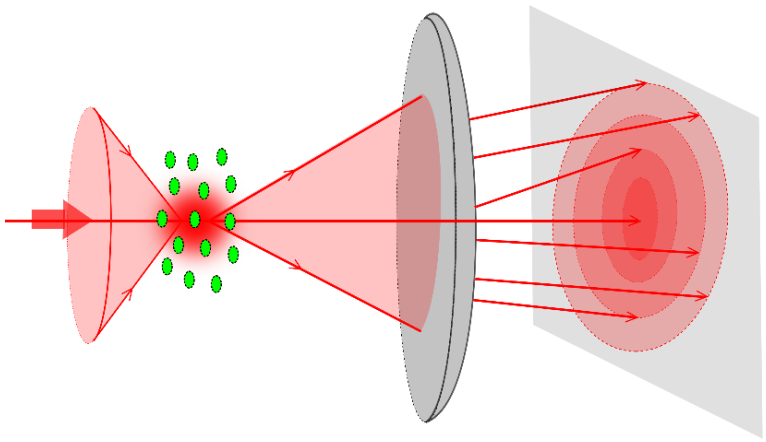

Figure 31 – Mie scattering phenomenon from a suspension of microspheres: a concentric organization of circles will appear, with a central concentration on intensity called Airy disk.

Figure 32 presents the results obtained for 15,45 µm polystyrene microspheres, 10^6/mL concentration, with a 20x 0.5NA air objective and 633nm light illumination. The results are compared with a theoretical simulation for the same kind of sample, utilizing Mie theory in Matlab. From the results of the comparison, visible in the bottom panel of the image via a line profile of the real (blue) and simulated (orange) image, it is visible a good accordance especially the closer we get to the zero angle. The first order peaks still present a good accordance, both in intensity and position, but the agreement breaks down the further we get from the central spot. This effect is at least partially due to (i) the noise in the measurement and (ii) the deviation from ideality of the spheres. In the top right of Figure 32 we can see the simulation of the mie scattering cross section for the sample. As expected, since the size of the particles is much bigger than the incident wavelength ($r>>\lambda$), we are in the mie approximation and the scattering is greatly skewed towards the forward direction.

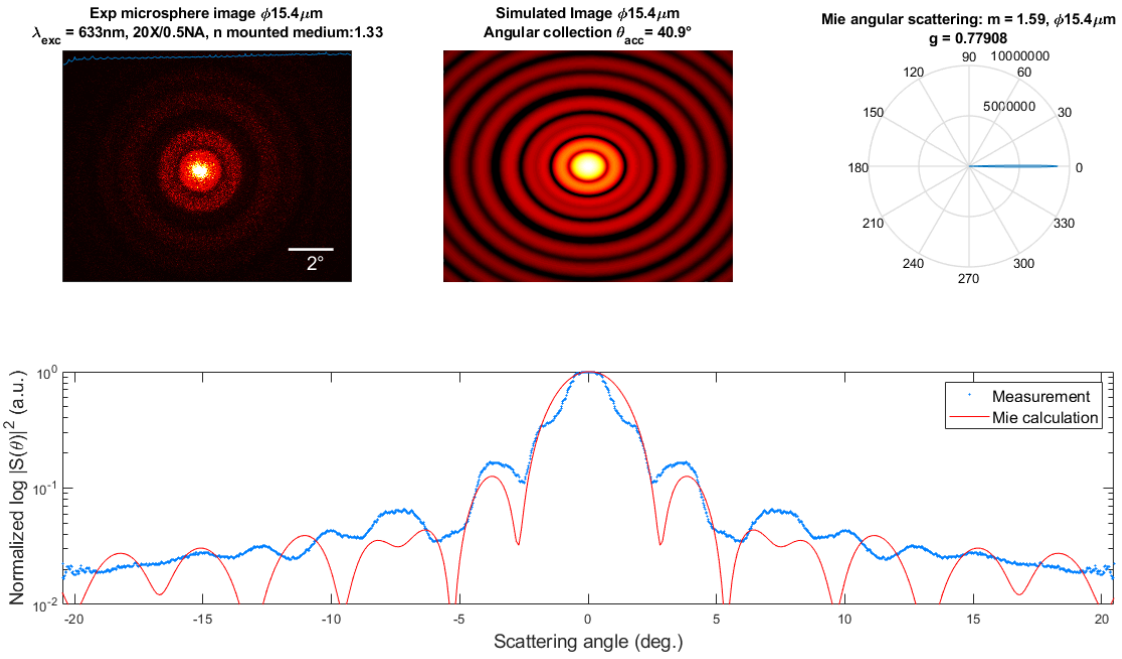

Figure 32 – Fourier image of a sample of 15.45 µm polystyrene microspheres in water solution, 10^6 µspheres/mL, λ=633nm, 20x/0.5NA objective (top left); a simulation utilizing mie theory calculations and the same parameters as the sample (top center); the Mie angular scattering simulation (top right); and the comparison between measurement in blue and simulation in red in a line profile around the horizontal like in the first two images (bottom).

The size of the central peak, corresponding to the Airy disk, is tied to the size of the scattering particles. This can be observed also in Figure 33, which contains the simulation of the same line profile in Figure 32 at different sizes of the scattering particles, from 1 µm to 20 µm with an objective 20X 0.5NA, the same used in the data above.

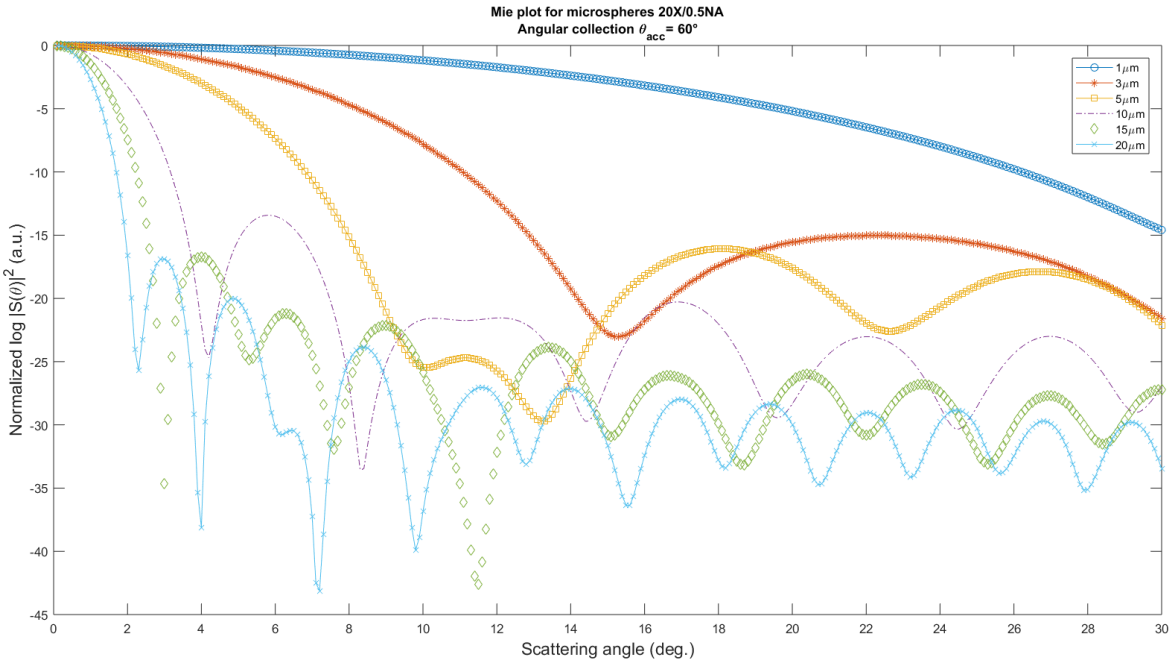

Figure 33 – Simulation of the line profile of the scattered light intensity in the Fourier plane of spherical particles of sizes varying from 1 to 20 µm.

It can be noticed that the central peak (corresponding to the Airy disk) becomes narrower as the size of the particles increases. The same can be seen in Figure 34, representing the simulations of the images relative to the profiles in Figure 33.

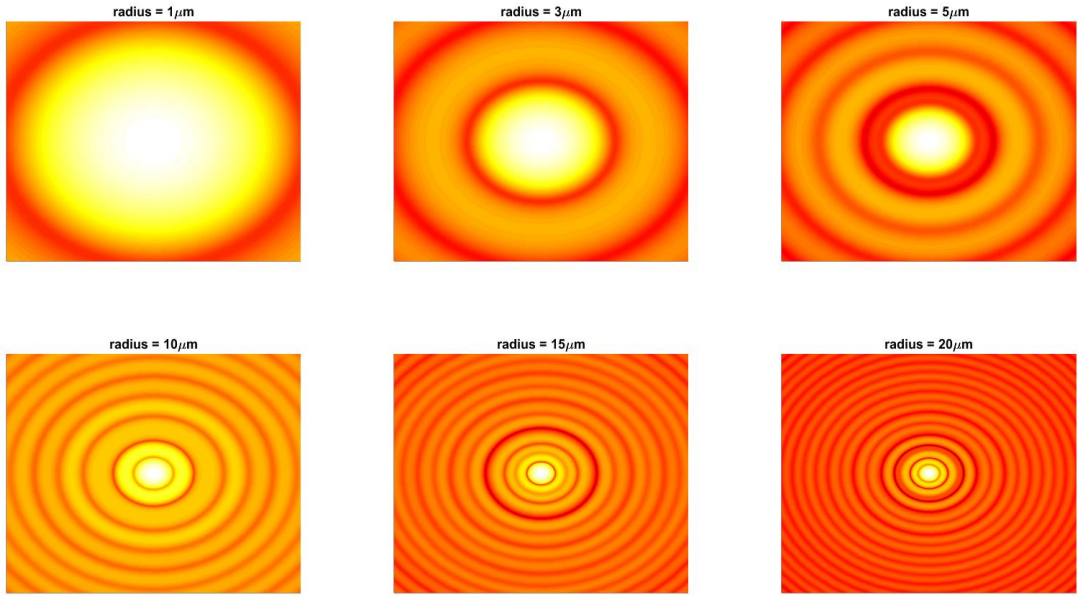

Figure 34 – Simulations of the images relative to the curves in Figure 33.

The measurement for the spheres in Figure 32 were repeated 15 times and the size of the Airy disk was estimated from the size of the central peak and averaged over all the images. This lead to the results in Figure 35. The nominal 15.45 µm spheres were measured by us to be 15.2 µm +/-0.6 µm, in complete accordance with expectations.

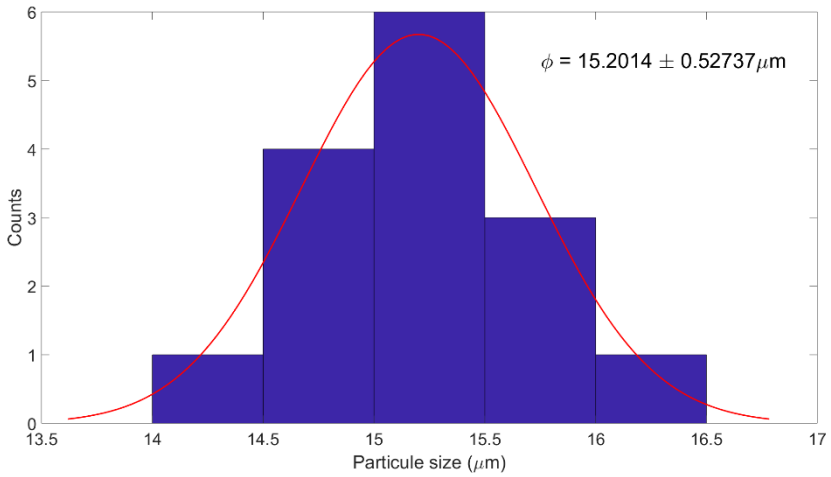

Figure 35 – The size of the microspheres as calculated by the estimated Airy Disk size in 15 samples (y axis: frequency of a certain diameter as measured within each bin). The distribution follows a bell distribution and allows us to calculate the standard deviation.

Conclusions

In this chapter we have introduced the phenomenon of scattering, its main regimens (Rayleigh at small particles sizes and Mie at higher particle sizes). We have shown the versatility of the technique and we have shown the literature demonstrating the role of chiral structures like the ones present in the super organization of chromatin inside the nucleus in creating differential scattering of the circularly left and right polarized light. This phenomenon is named CIDS and we have shown the literature with its numerous applications in all fields, including biology. We have also described some of the setup utilized to measure it, as well as our homemade angular CIDS spectroscopy setup. We have validated this setup with arabinose, a well-known chiral sample, and have demonstrated its sensibility to chromatin in samples of isolated nuclei when compared to simple polystyrene microspheres.

Finally, we described a different approach that we attempted at gaining the angular information by utilizing a Fourier imaging microscope to obtain the scattering information without moving parts, unlike the angular CIDS setup. The light scattering microscope is a promising avenue for our research that has up to now demonstrated its sound ability to measure microsphere sample and attribute the correct parameters to them when compared to theoretical Mie simulations. The setup will need to be outfitted with polarization optics to allow angular polarization imaging without moving parts and nuclei samples will be the first to be tested.

Chapter 3: CIDS Imaging on Chromatin Organization

Introduction

In the previous chapter we introduced Circular Intensity Differential Scattering (CIDS) spectroscopy as a technique to obtain information from a biological sample from its optical fingerprint. This technique measures the CIDS signal in a one-point mode, by scanning it across a 180° angle. CIDS corresponds to the scattering part of circular dichroism. In the following chapter, we will focus on the use of CIDS in imaging microscopy applications. The interest in CIDS imaging stems from the need for a label-free technique to study biological samples. The most utilized technique for imaging of biological samples is fluorescence microscopy, in which specific parts of the sample are marked with fluorescent molecules that absorb the incident light and emit in turn light at a higher wavelength. In this way, chromatic filters allow to separate the contribution of each fluorophore, allowing to image specific structures. Thanks to the elevated specificity, fluorescence imaging is the golden standard in biological imaging, as it is otherwise hard to resolve the different structures in the complex biological samples with simple light transmission or reflection. CIDS though has demonstrated its sensitivity to the chiral structures present in chromatin organization, and is a good candidate for a label-free imaging method for this biological system. The label-free methodology allows to avoid some of the problems with fluorescence imaging, namely (i) the need for specific fluorophores for each application and structure; (ii) the possibility of human error during the labeling phase; (iii) the possible change of conformation of the structures to analyze due to the presence of the labels; (iv) the high light dose required for fluorescence imaging, which can lead to problems such as photobleaching and damage of the sample.

A coarse division of the imaging techniques in the field of biophysics identifies two main modalities: widefield and scanning techniques. In the first group, the light is shined in the whole field of view and collected in a single shot by a camera. In the second, a laser is focused on a point (called the point spread function, PSF) on the sample and scanned to reproduce the image pixel by pixel. While slower than widefield microscopy, this technique allows for a variety of methods to increase the resolution and quality of the signal of fluorescence. For this reason, we implemented CIDS in a scanning configuration, demodulating the signal pixel by pixel thanks to the use of a lock-in amplifier. In this way, the technique can be coupled with others to obtain a clearer picture of the sample's structure and properties with different kinds of contrasts. Particular care needs to be put in coupling the CIDS signal with a scanning setup as the speed of the CIDS acquisition is limited by the speed of the generation of the polarization states. The use of a photoelastic modulator in the PSG allows for pixel dwell times of 40 μs, a timeframe compatible with scanning microscopy.

The first part of the chapter will be dedicated to discussing the theory of CIDS microscopy and its applications, with various setups that were used over the years and their differences. I will then present the hybrid confocal fluorescence/CIDS microscope that I have built, aligned and utilized in the course of this work.

In the second part of the chapter, the results relative to the CIDS microscopy of isolated HEK cell nuclei will be presented, showing the ability of our technique to image chromatin organization in this kind of sample. It will be shown also how more information can be extracted from the polarization data available through our microscope.

Finally, in the third and last part of the chapter, we will illustrate the novel implementation of expansion microscopy (ExM) with our CIDS imaging technique to obtain an approach that we have called ExCIDS. Expansion microscopy allows to increase the resolving power of a fluorescence microscope by encasing the sample in gel which is then digested, eliminating most biological matter, and expanded. This allows us to single out the nucleus and its chromatin in a more gentle way than the centrifugation process we previously utilized for isolation, possibly preserving the structure in a better way. It also allows us to probe the capability of our technique to be sensitive to the change in structure of the chiral conformations present in the nucleus due to the expansion and in particular of their radius and pitch.

Part 1: CIDS imaging and microscopy

1. CIDS imaging theory

CIDS imaging is the implementation of CIDS measurement on a microscopy apparatus, which allows the planar (xy) mapping of optical activity in a sample by the scanning of the microscope's Point Spread Function (PSF). This kind of application was first detailed by Keller et al. [138]. In this way, imaging of the optical activity of the sample is possible without the use of fluorescent markers. Structures that would be too small to be resolved by conventional optical microscopy can be revealed thanks to the sensitivity of CIDS to chiral structures of a size down to $1/20^{th}$ that of the incident wavelength. As we have shown in chapter 2, this makes the technique able to sense the chiral structures of chromatin, for example those relative to the 30nm fiber (about $1/20^{th}$ of the wavelength of visible light). The same considerations for one-point measurements are valid for the microscopy modality of CIDS: the signal is angularly and spectrally dependent.

In particular, in the microscopy configuration of CIDS there are two imaging modalities [139]:

- Bright Field imaging;
- Dark Field imaging.

These two modalities are presented schematically in Figure 36 for the configuration where the sample is imaged with a simple lens. In bright field imaging (a), the light wave with wave vector $\mathbf{k}_0(B)$ impinges on the sample and the detector is positioned directly behind the optical train, in the line of the direct transmission of light. In the dark field configuration (b), the detector is not directly aligned with the wave vector $\mathbf{k}_0(D)$ of the incident light, but is put at a certain angle θ. In this way the scattered light from the sample is registered by the detector. While the phenomena of absorption, scattering are both present in either modality, the bright field is dominated by the absorption effects while the dark field by the scattering ones [140]. It was shown in that the dark field regime is more sensitive to chiral groups of a bigger size, with dimensions comparable to the one of the incident light, while the bright field is preferable to study shorter range chiral order [140].

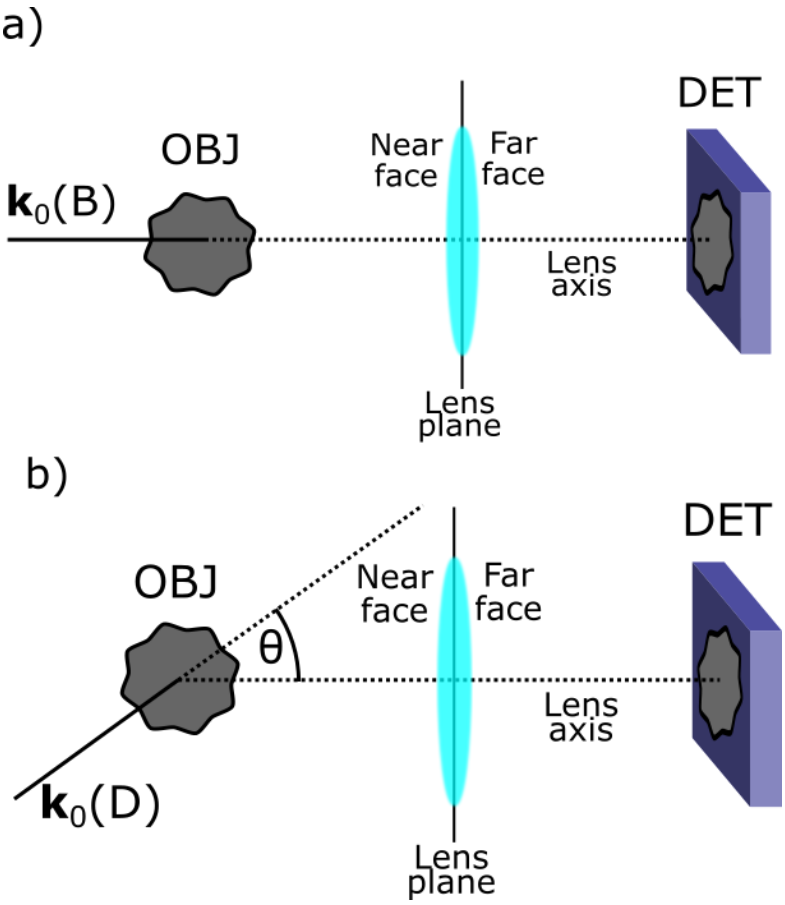

Figure 36 – Schematic representation of the a) bright field and b) dark field configurations of imaging with a simple lens. $\mathbf{k}_0$(B) and $\mathbf{k}_0$(D) are the wave vectosr of incident light for bright field and dark field imaging respectively; OBJ is the object that is studied; DET is the detector.

This kind of system was studied by Bustamante et al. first by utilizing the first Born approximation [140] [141] [142], where the internal electric field experienced by the polarizable groups is approximated by the incident electric field. As was explained in Chapter 2, this is not the most precise approximation, especially in the case regarding chromatin structures. Since the density of polarizable groups is high, there is a high chance of multiple scattering events and dipole-dipole coupling happens between different polarizable groups, each of which experiences an internal field that is a superposition of the incident electric field and the all the other fields generated at every other dipole inside the molecule. For this reason, they offered a deeper study that takes into consideration higher Born approximations [108]. With these deeper calculations the polarizability tensors that were used in the first Born approximation were replaced by effective polarizabilities, which included the effects of interactions between different polarizable groups.

It was shown that the thickness and anisotropy of the sample are strictly correlated with the circular dichroism signal [108], which makes the m_{03} and m_{23} elements of the Mueller matrix (the

ones connected with CIDS, see Chapter 1) the most interesting ones in such cases. It's worth noting that the effect of a cross interaction between different chiral groups does affect the signal pixel by pixel, creating artifacts in the PSF (Point Spread Function) and making optical sectioning like the one in confocal microscopy impossible [143]. Experiments studying the organization of chloroplasts have validated the theoretical studies proposed [144].

2. CIDS imaging setups

In Figure 37 the different optical microscopy configurations for pixel-by-pixel CIDS imaging have been summarized.

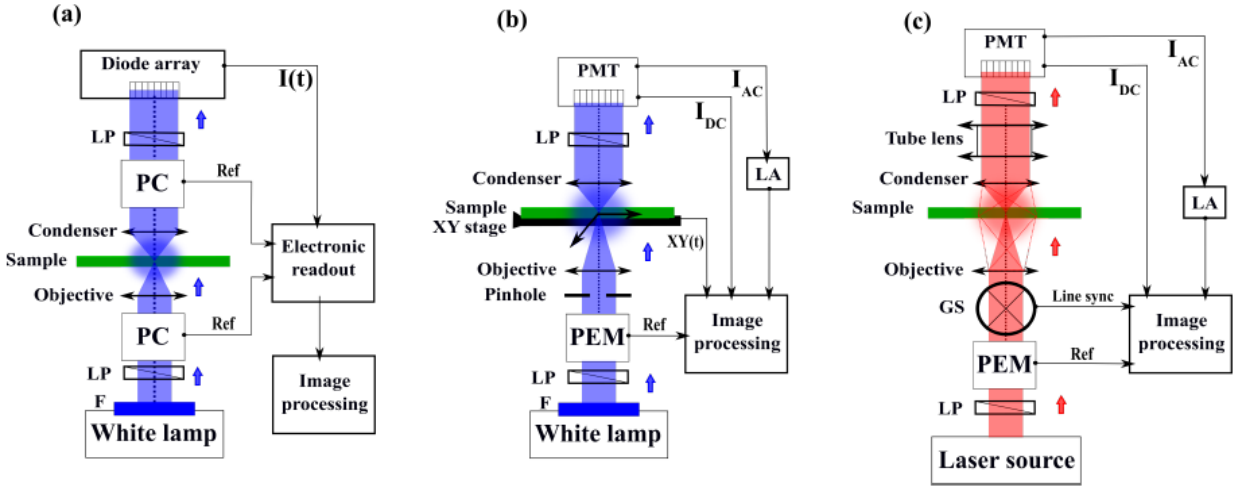

Figure 37 – The block diagram of various optical microscope architectures that allow the imaging of the CIDS signal pixel by pixel. (a) Optical microscope in wide-field configuration using two Pockels cells, inspired by [124,125]. (b) Optical microscope using one photoelastic modulator synchronized with a lock-in amplifier and an XY translating sample holder, inspired by [100,126,127]. (c) Optical scanning microscope using a photoelastic modulator synchronized with a lock-in amplifier, inspired by [128–130]. PC: Pockels Cell. PEM: Photoelastic Modulator. F: monochromatic filter. LP: Linear Polarizer. LA: Lock-in Amplifier. PMT: Photo-multiplier tube. GS: galvanometric scanner.Figure reproduced from [126].

A first example of an imaging setup for CD/CIDS appeared from Mickols et al. [145]. This setup was created by modifying an already functioning CD microspectrophotometer and utilizing its same monochromatic light source and the line-scanning detector made of a diode array. The main changes were the addition of two Pockels Cells in the light's path, one in the PSG and one in the PSA. The PCs were connected and synchronized to the diode array so that the image was integrated over a half period of the cells modulation cicle. In this way, there was no need for a lock-in amplifier as the signal was demodulated electronically. The setup was utilized to study red blood cells, their sickled form and Chinese hamster ovary cells. An evolution of this setup, closer to modern CIDS experimental configurations, was later proposed [146]. This approach made use of a lock-in amplifier in conjunction with a high efficiency photocathode, resulting in a

much better signal to noise ratio, reduction of the power required for a measurement and a faster response at 30 ms per pixel. This allowed to image individual sickled blood cells.

Similar setups that made use of the modulation and demodulation of circular polarization were proposed in the confocal imaging modality. This allowed for an increase in resolution typical of this technique. The use of a scanning stage in these setups had the drawback of slowing down the measurement due to the need to wait for the scanning of the sample. Thanks to these experimental configurations, DNA/RNA imaging was performed on different cell cycles and drosophila spermatocites [147] [148], as well as thylakoid membranes in chloroplasts [149] [129].

Finally, the latest iteration of CIDS imaging was the implementation of the technique in a scanning microscope [150] which allowed polarization imaging pixel by pixel at a faster rate (microseconds per pixel), resulting in a more robust and sensitive measurement. In this version of the setup, two PEMs are placed before and after the microscope body, which is composed by a tube lens, a galvanometric scanning head, the objective and the condenser. The signal is demodulated and then collected by a single point detector, which is in turn synchronized with the scanning head. This makes it possible to reconstruct the Fourier harmonics of the signal of the PEM for each pixel.

An important parameter for the scanning configuration is the pixel dwell time. This is the time that the scanned beam spends on each pixel. The faster the scanning of the beam, the faster the acquisition time (assuming the number of pixels is equal), and the lower will be the pixel dwell time. This is of particular interest in polarization imaging for time-domain approaches to polarization encoding, since the pixel dwell time needs to be large enough to allow the PSG to generate all the required polarization states and the PSA to analyze them.

Another thing to take into consideration in this kind of setup is the role of the sample thickness in the ability to obtain realistic images. Polarization, unlike confocal fluorescence microscopy, is not capable of optical sectioning. Therefore, the information will be averaged over the entire volume traversed by the light and muddled by multiple scattering effects. The contribution of a particular plane xy can’t be retrieved except for very specific cases, like a sample with very low density or thickness [151] or for very deterministic samples such as metamaterials and crystals [143].

Finally, one last effect to take into consideration is the effect of high numerical aperture objectives on the polarization control. By focusing the beam, the original polarization will be partially lost due to the 3D effect of changing the angles of the electric field relatively to the reference frame. This effect can be ignored for low NA objectives as the discrepancy is low, but the higher the NA, the more prominent it is [5].

3. CD/CIDS imaging applications

CD/CIDS imaging was used for biological applications to study sickle blood cell anemia to compare their structure to healthy blood cells [145] [152] [146]. This experiment demonstrated practically that the conformation and concentration of DNA causes a change in CIDS signal. Furthermore, CIDS imaging was utilized to study DNA/RNA organization at different cell cycles and in the case of transcription activation in spermatocites of the fly Drosophila [147] [148], as exemplified in Figure 38.

The technique was also applied to thylakoid membranes in plant chloroplasts [129] [153] (shown in Figure 39) where it was used to determine that the buffer in which the sample is encased plays a major role: depending on it the sign of the CIDS signal can be reversed. This could thus be a further source of error in CIDS imaging measurements as the long range chiral domains could superpose their signal, creating artifacts.

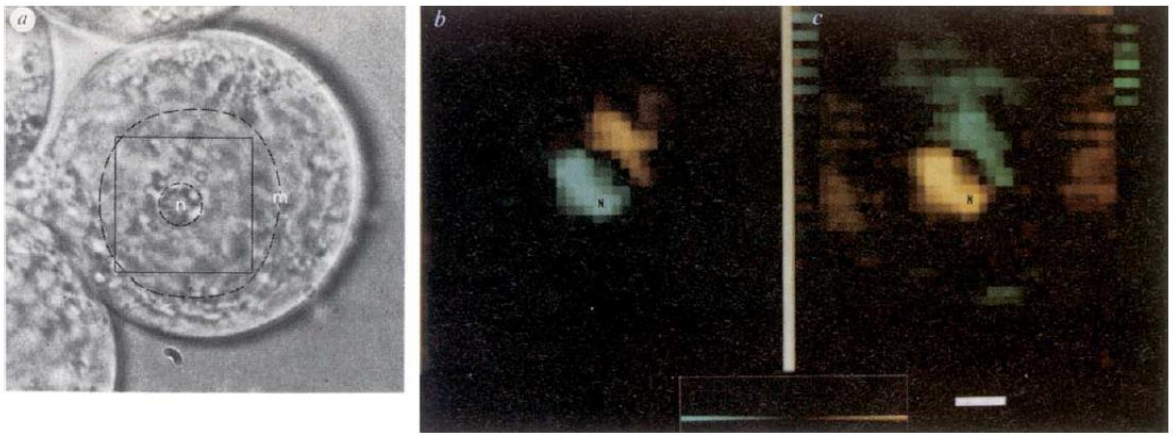

Figure 38 – Image relative to a spermatocyte. a) Intensity image; b) Circular Dichroism image; c) Linear Dichroism image. The square in a) represents the area imaged in b) and c). The big circle represents the nucleus and the small one a nucleoulus. [148]

Finally, it's worth noting that despite this work focusing on the application of CIDS to biological samples, the sensitivity to anisotropy and simplicity of the technique allowed it to be used as a label-free tool to study metamaterial organization [154] [155] [156] [157] [158] and to study chiral polymer organization in special conditions [159] [160] [161].

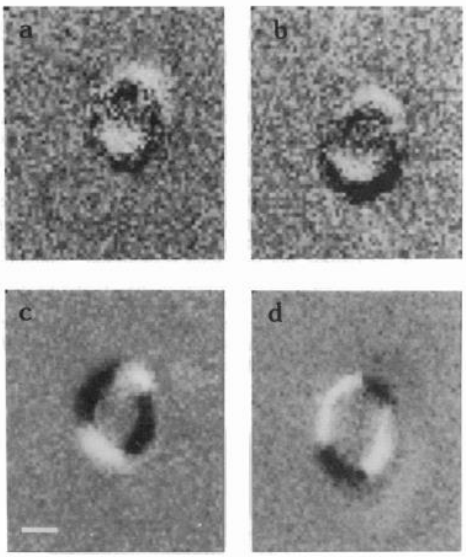

Figure 39 – Circular Dichroism (a, b) and Linear Dichroism (c, d) for a chloroplast. Images recorded at 670nm, scale bar 2 µm. Images from [129]

4. Our CIDS imaging setup

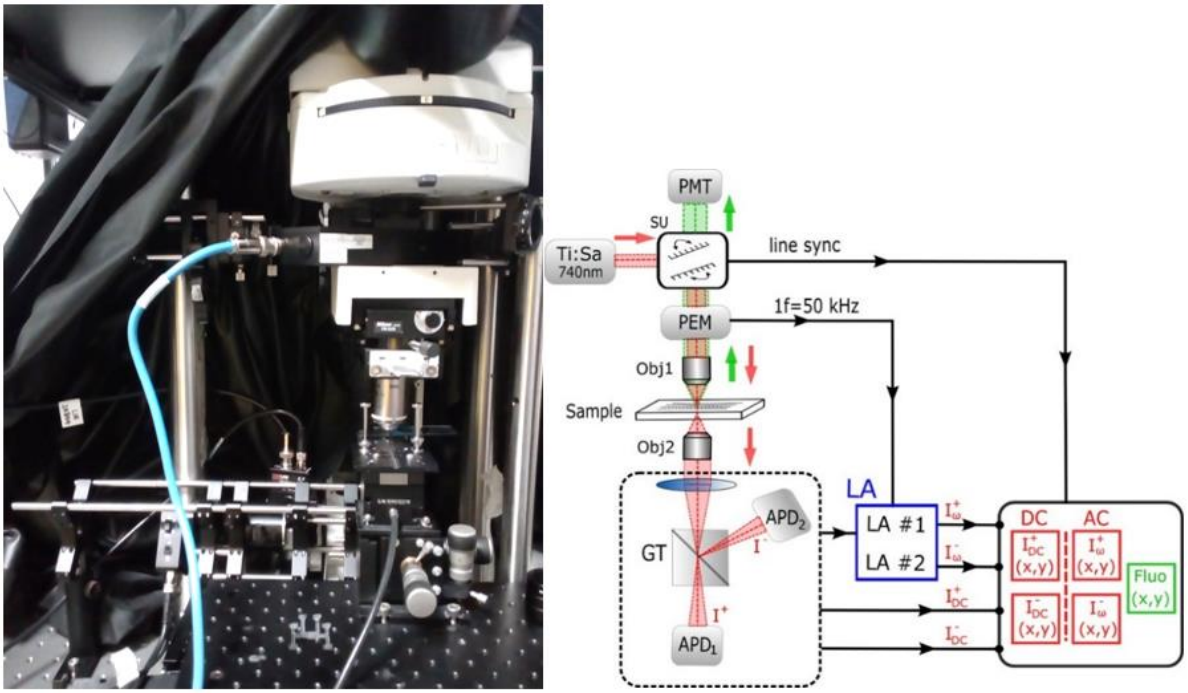

Figure 40 – Left: an image of the measurement part of the CIDS microscope. Right: schematics of the CIDS microscope. PMT: photomultiplier. PEM: Photoelastic modulator. LA: Lock-in Amplifier. APD: detectors. GT: Glan-Taylor prism.

I have assembled a hybrid CIDS/fluorescence microscope setup. A photograph of the setup is shown in Figure 40, as well as the schematics in the form of a block diagram describing its parts. The basis of the setup is a commercial Nikon scanning confocal fluorescence microscope, including a galvanometric scanning head and a control unit (C2 + , Nikon Instruments, Yokohama, JP). The light source utilized for illumination is a Ti:Sa femtosecond laser (Chameleon Ultra II Coherent Inc., Santa Clara, CA, USA), which was set to an operative wavelength of 740 nm, which rests outside the absorption band of biological samples and biopolymers like chromatin. The microscope can collect fluorescence in reflection by measuring the light intensity with a PMT positioned after an interchangeable dichroic filter that allows the selection of the wavelength corresponding to the desired fluorescence wavelength. Inside the optical path of the microscope, after the scanning head, all the components of the PSG and PSA were integrated, with the exception of a linear polarizer positioned before the scanning head itself for lack of space.

Thus, after passing through the scanning head, the light is shined directly into the PSG, which is composed by a PEM (PEM-100, Hinds Instruments Inc, Hillsboro, OR, USA) with an operating frequency of 50kHz. This is in fact a one PEM setup as described in the previous chapter. Immediately after, the light passes through an objective by which it is focused on the sample to analyze. In particular, we utilized a 100X 1.3NA objective from Nikon (Plan Fluor DIC H, Nikon Instruments, Yokohama, JP). This resulted in a diffraction-limited resolution of 300nm. The light is then transmitted through the sample, after which it's collected by another Nikon objective, this time a 40X 0.6NA Plan Fluor EL WD which acts as a condenser. After this, the light passes through a 50mm focal length lens which has the role of maximizing the field of view and the size of the light spots on the detectors

For the setup we chose a parallel approach to the PSA: a Glan-Taylor polarizer (GT10-A calcite polarizer, Thorlabs, Inc., USA) spatially separates the light beam in two orthogonal polarization states, which are each collected by a detector. The two detectors are the same model of Avalanche Photodiodes with tunable gain (PDA36A-EC, Thorlabs, Inc., USA). This feature is important in our setup because the "crossed-polarizer" configuration leads to the possibility of having very big differences of light intensity depending on the sample's optical properties and the condition, as well as big differences between both channels. For this reason, a way to be able to tune the gain of each channel independently and fastly is necessary in such a setup.

Finally, both detectors are connected to our Lock-In Amplifier (HF2LI Zurich Instruments AG, CH), which is also connected to the reference signal of the PEM in the PSG. This allows us to collect 4 different channels: one for each detector for the continuous component of the signal, integrated by the detectors over the measurement time, and one for the demodulated signal at the reference frequency. Each of the four channels is connected to the Nikon control unit which can acquire all channels simultaneously. The measurement is controlled by the Nikon Instruments imaging software NIS Elements.

The relationship of the angles between the optical elements is as described in the calculations of Chapter 2: The first linear polarizer is positioned at -45° compared to the reference angle; the

PEM is oriented at 0°; the Glan-Taylor polarizer in the PSA divides the light in two orthogonal linear polarizations at +45° and -45°. Thus, all relationships described in the previous chapter hold and, among others, the m03 element of the Mueller matrix, corresponding to CIDS, can be extracted from the measurements. Finally, for the analysis of the images, the software FIJI [162] was utilized.

I personally wrote a macro that starting from the raw images of each channel, performs the analysis as explained in chapter 1, page 29. In particular the steps of the macro are:

- Subtraction of the relative background image from each channel;
- Summation the two AC channels;
- Summation of the two DC channels;
- Divide the obtained image of the sum of AC by the image of the sum of the DC (this means that each pixel in the AC image is divided by the relative pixel in the DC image) to normalize;

The setup described allows us to obtain the CIDS and fluorescence signal pixel by pixel, reconstructing full images of up to 1024x1024 pixels. For data acquisition, I used the 512x512 resolution because of limits due to the pixel dwell time (the time spent by the setup to acquire signal from each pixel) and the time of measurement of the polarization signal. In particular, the maximum pixel dwell time at 1024x1024 was of 20µs, while the time needed to measure the polarization signal is 40µs. The limit in this case is the speed of the generation of polarization in the PEM in the PSG (50 kHz). This is more in line with the pixel dwell time achievable at 512x512 (about 44µs).

While the technique theoretically allows to acquire both modalities at the same time, technical limitations in our experimental configuration (a maximum of 4 channels could be taken at a time by our controller) lead to taking the fluorescence and CIDS signal separately. This is because one channel is needed for the fluorescence signal and 4 channels are needed for the polarization signal required to build the CIDS image, two for the direct DC signal from each detector (utilized for normalization) and two for the AC signal extracted by the lock-in (used for the calculation of the m_{03} element).

Considering that:

- The time required to take an image is of the order of half a minute;
- At the moment we have utilized only fixed samples;

We assume that there is no relevant movement of the sample in the time needed to take both modalities, which is also proven by the correspondence of CIDS and fluorescence data in the images taken. In the future, living samples could be imaged to obtain more information of

chromatin in vivo, in which case a higher number of acquisition channels to obtain all images at the same time will have to be implemented.

It's worth noting that a single measurement allows to have both the continuous and alternating intensity images for both channels in the polarization modality. The lock-in amplifier allows to choose a multiple of the reference frequency. By repeating the measurement another time both the signal at ω and 2ω can be obtained, allowing access to more elements of the Mueller matrix if needed.

5. Alignment

A correct alignment of the optical devices in the microscope is fundamental to obtain a correct CIDS measurement, as otherwise the mathematical relations described in previous chapters do not hold true anymore. For this reason, a Stokes detector is utilized to measure the polarization state of the light at the sample plane. The detector plots the measured polarization state in real time on a Poincaré sphere, allowing to precisely select the required polarization state without the need of complex measurements. The Poincaré sphere is a representation of the polarization state of light and is presented in Figure 41. The three elements of the stokes vector S_1, S_2 and S_3, corresponding to the light polarized at 0°/90°, +45°/-45° and circularly left/right are represented in the three dimensional axes on the sphere. Completely polarized light will present a signal on the surface of the sphere, while completely unpolarized light will present a signal at the very center of the sphere.

This process serves to align the polarizer in the PSG with the axis of the setup in a reproducible way. Once this operation has been completed successfully, the Glan-Taylor in the PSA can be aligned to be in accordance with the PSG's polarization orientation so that one of the axes is parallel and one is rotated by 90° relative to the PSG's polarizer. The transmitted light will be parallel and the reflected light will be rotated.

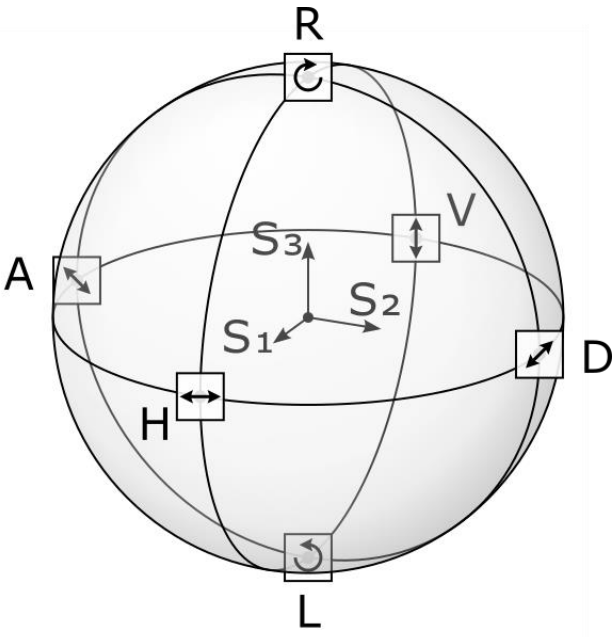

Figure 41 – The Poincaré sphere. Completely polarized light will fall on the surface of the sphere, while completely unpolarized light will be at the center of the sphere. The 0°/90° polarization, relative to the S_1 element of the Stokes vector, is represented by the H/V points, +45°-45° (S_2 element) by A/D and circular left and right (S_3 element) by L/R.

To characterize the polarization quality and the performance of the polarimeter, the following technique was utilized. The light is shined through the setup. A linear polarizer is put in place of the sample without the objective present.

The intensity data is measured by the detectors of each channel and the LP sample is rotated in steps of 10° while repeating the measure until a total of 180° has been covered. The PEM is turned off during this step as it will be aligned next. In this way, the sum of the two channels is expected to follow the Malus law. The Malus law is the law describing the intensity of total transmitted light through two linear polarizers, one of which is rotating. The Malus law is as follows:

$$I = I_0 \cos^2 \theta$$

where I_0 is the initial light intensity, after the first linear polarizer, and θ is the angle between the axes of the two polarizers. The result registered in our setup is illustrated in Figure 42, where the theoretical value just described is presented with the continuous orange line. The experimental values are taken in steps of 10° of rotation of the sample LP. The total light intensity is calculated by summing both channels of our setup. The scanning of the beam is stopped, making the measurement single point, to have the information of the alignment of the optics in a simple

way. Thus, the acquired images present a uniform value, which was averaged over all pixels. The channels are named DCT, where the T stands for transmission (the parallel channel), and DCR, where R stands for reflection (the perpendicular channel). The registered error is around 15% at most, deriving from some slight misalignment of the polarization optics.

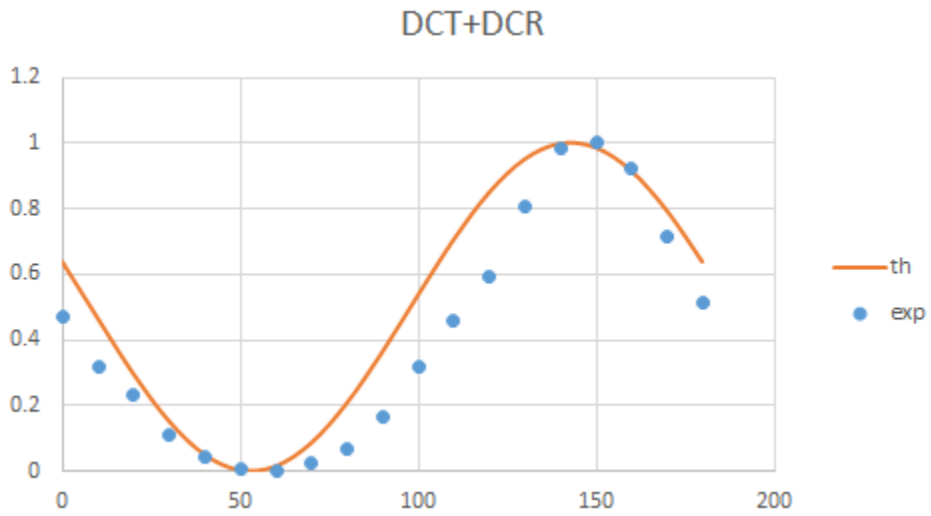

Figure 42 – Theoretical (orange) and experimental (blue) light intensity after normalization in the sum of the two channels in the CIDS microscope with the PEM off and a LP sample, rotated in steps of 10°.

At this point, the PEM can be turned on to make sure it is aligned as well. Both channels are measured and expected to follow a $\cos^2$ law, with a phase difference of 90°. The results of the measurements are shown in Figure 43, where both the DCT and DCR channels are given for the LP sample with the PEM on.

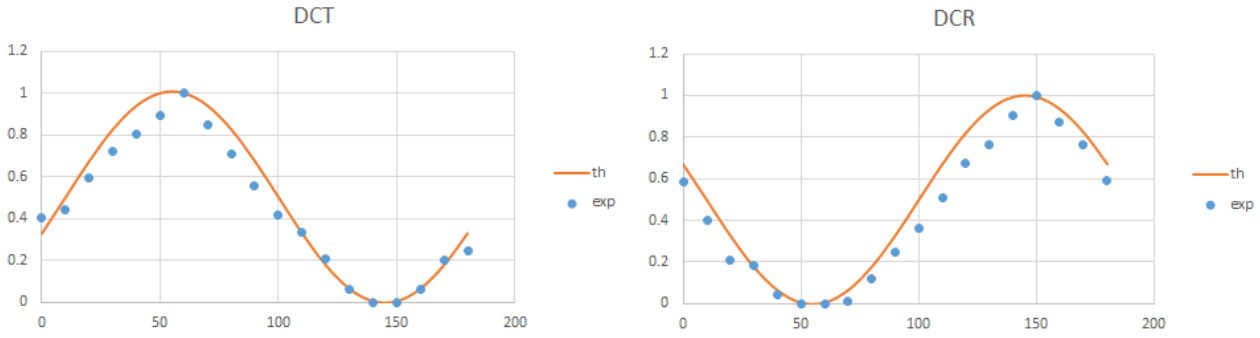

Figure 43 – Plot of the theoretical (orange) and experimental (blue) normalized light intensity relative to a linear polarizer sample rotated in 10° steps in the Transmitted (left) and Reflected (right) channel of the Glan-Taylor polarizer after aligning the PSA in the CIDS microscope. The PEM is turned on

In this case, the expected theoretical value (in orange) is corresponding to a $\cos^2$ law for each channel, with a difference of 90° in phase because the two channels are relative to orthogonal linear polarizers.

6. Image acquisition

Image acquisition for all of the images that will be presented in this chapter has been performed at 512x512 pixels. The pixel dwell time is dependent on the integration time of the lock-in amplifier and has been set to be equal to 40 µs. Each image is averaged temporally 4 times to improve the signal to noise ratio, leading to a total acquisition time for one full measurement of 20 seconds. For a complete CIDS and fluorescence measurement in our setup, two of these measurements in sequence are needed, as our acquisition board only supports 4 channels and we need 4 channels for the CIDS data and one for the fluorescence. As a consequence, the total measurement time including switching out cables takes about 1 minute, a time that is compatible with fixed samples like the ones used in this work. By decreasing the averages or resolution, the measurement times can be brought down to about 5 seconds.

Furthermore, a third measurement can be performed to acquire the signal at 2ω relative to the double of the frequency of the PEM, allowing to calculate even more elements of the Mueller matrix, in case more information is needed on the sample. This step is optional and not needed for CIDS imaging.

To take in consideration the differences between the two photodiode channels, an area of the sample where no biological matter is present is taken as representation of the background. Its intensity value is calculated as the average intensity of this area. The ratio between the two channels will be the rescale factor G, by which one channel will be rescaled in function of the other to obtain comparable data.

$$G = \frac{I_{BG}^{+}}{I_{BG}^{-}}; \tag{74}$$

One such calibration image is shown in Figure 44.

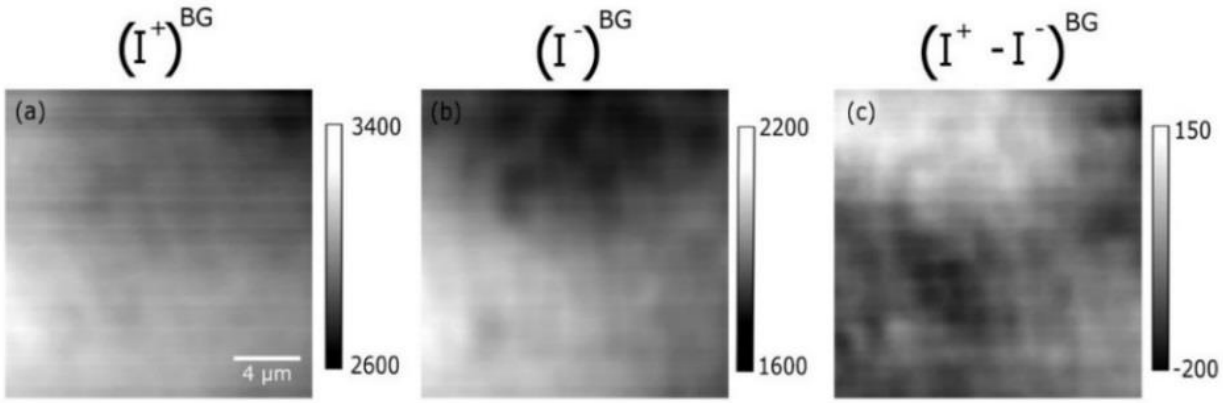

Figure 44 – Example of calibration image in the CIDS microscope sample. The background image for the first channel (a), the second channel (b) and the difference of the two (c). The resulting rescale factor in this case is 1.6.

The background relative to an image is shown, for both channels (panels (a) and (b)). In panel (c), the difference between both channels is shown. For the particular sample used here, the G factor was equal to 1.6, meaning the values of intensity registered in the second channel shown in (b) have to be multiplied by 1.6 times to obtain a result that is comparable with the intensities of the first channel.

Part 2: CIDS imaging of isolated nuclei

1. Extraction and isolation of HEK cell nuclei

The imaged nuclei are extracted from HEK 293 cells grown in a DMEM medium with the addition of 10% FBS, 1% penicillin-streptomycin and 1% glutamine. The isolation process was conducted by swelling the cells for 30 minutes in a hypotonic buffer containing 10 mM Hepes pH 7.5, $MgCl_2$ 2 mM, KCl 25 mM, PMSF 1 mM, DTT 1 mM and a Halt protease inhibitor cocktail by Thermo Fisher Scientific (Waltham, Massachussets, USA). Afterwards, the swelled cells were lysed with a glass Dounce pestle, clearance range of 0.025-0.076 mm (Tecnovetro s.r.l. Monza, Italy). Sucrose is added to the solution up to the final concentration of 250 mM while the lysis process is moniterod via a bright field microscope and the solution is then centrifuged at 1200 g for 10 minutes. The isolated nuclei, collected on a pellet, are then suspended in a nuclear buffer with the following components: 10 mM Hepes pH 7.5, 2 mM $MgCl_2$, 25 mM KCl, 250 mM sucrose and Halt protease inhibitor cocktail by Thermo Fisher Scientific. Another centrifugation takes place for 15 minutes at 800 g, after which the nuclei are resuspended in the nuclear buffer. The process is repeated a total of three times. At this point, a 10 minute incubation with Hoechst 33342 (Thermo Fisher Scientific) is performed with a dilution of 1:1000. As a final step, the nuclei so extracted are fixed in a solution of 3.2% Paraformaldehyde (PFA) and 0.1% Gluteraldehyde (GA) in PBS. The solution containing the labeled nuclei is deposited on 24 mm cover glass that has been treated with Poly-L-Lysine from Sigma-Aldrich at 37° C for 30 minutes. The sample is now ready for observation on the fluorescence and CIDS microscope.

2. CIDS imaging of HEK nuclei

The isolated nuclei samples on cover glass are put in the sample holder of the CIDS microscope and imaged with both CIDS and fluorescence modalities. The data is treated as explained in the previous subchapter according to CIDS treatment. In Figure 45 the results of the analysis performed on a single HEK nucleus are shown. Panel (a) illustrates the image relative to the normalized CIDS signal deriving by imaging a single isolated HEK 293 cell nucleus, while panel (b) is relative to the fluorescence image due to the chromatin marking with the Hoechst 33342 fuorescent probe. The two modalities are taken without moving the sample and are therefore relative to the same nucleus, in the same position. The two images have been merged in panel (c) to facilitate viewing the correspondence between both modalities. The golden arrow present in this panel is relative to the line profiles presented in panel (d), where the numerical value of both modalities are given for a more quantitative confrontation (CIDS in blue, fluorescence in green).

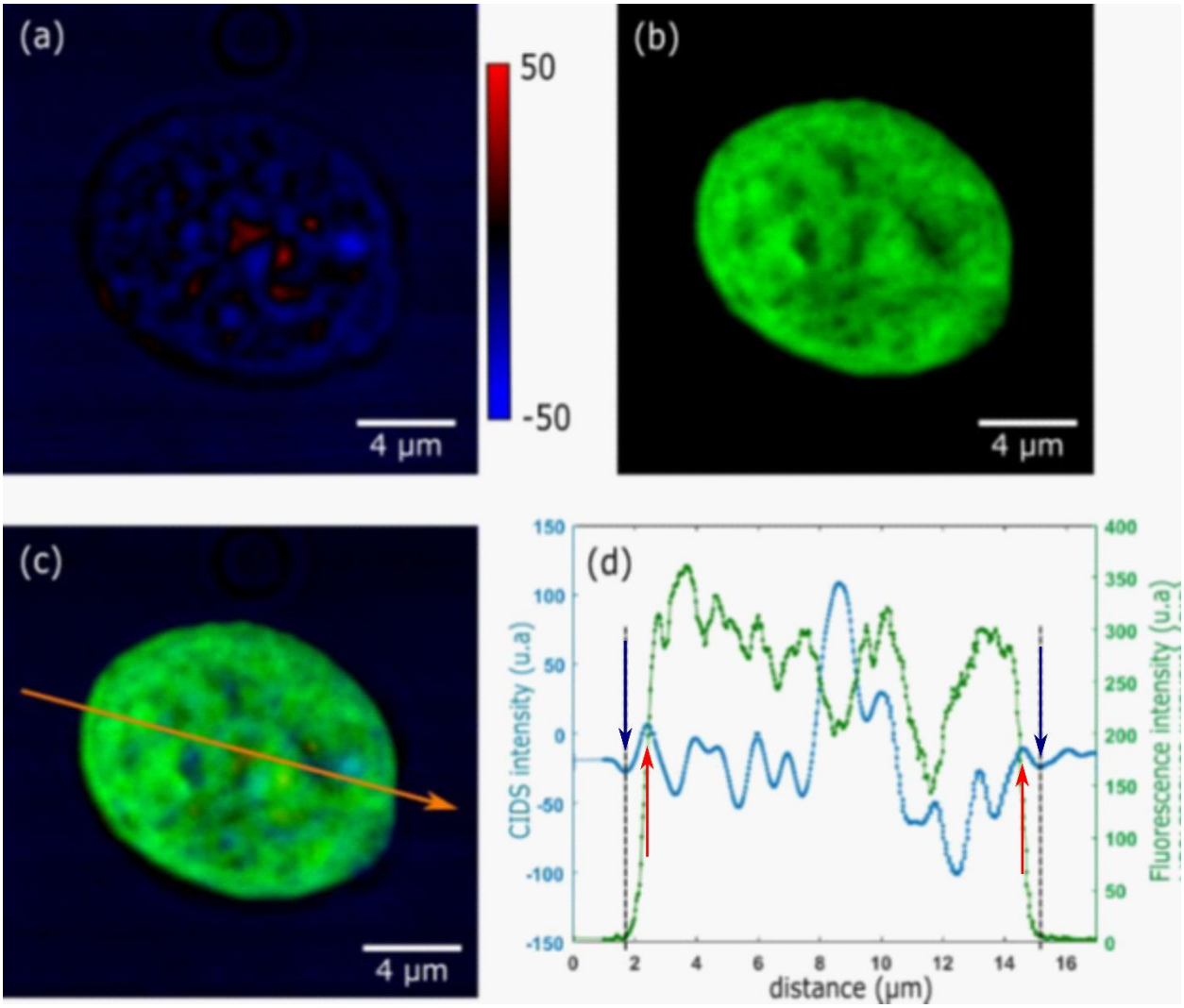

Figure 45 – (a) CIDS and (b) fluorescence imaging of an isolated HEK cell nucleus marked with Hoechst 33342. (c) Composite image of the CIDS and fluorescence signal. (d) Line profile of CIDS (blue) and fluorescence (green) signals relative to the golden arrow in (c), where the deduced area of the nucleus is highlighted by the vertical black bars.

Starting from panel (a), from the CIDS image the nucleus profile can clearly be discerned from the background with the polarization signal, as well as some internal structuring that we have attributed to the chromatin organization and compaction level. Proof of the correspondence between CIDS signal and chromatin presence can be found from the merged image with the fluorescence modality and the line profile traced there. In panel (d), the size and edges of the nucleus are estimated from the fluorescence signal, which is known to be deriving from the chromatin contained inside, and is marked by the two vertical dotted black lines. As can be seen, there is a very good correspondence between the start of the more dramatic changes in CIDS signal from the background level and the size of the nucleus, suggesting indeed a response from

the chiral structures deriving from chromatin, with a much higher dynamic range and contrast than the one present in the fluorescence signal. A discrepancy is registered between the dynamics of the CIDS peaks and the ones of the fluorescence and the correlation is not linear. This is due to various reasons. First of all, the resolution for both modalities, though close, is theoretically not the same. The resolution for the fluorescence image is proportional to the square of the light intensity I^2, while the CIDS resolution is limited by the Rayleigh criterion to a value of about $\lambda/2NA$, meaning that for a 1.3NA objective with 800nm light the resolution is about 300nm. Furthermore, the fluorescence phenomenon is not angularly dependent: the emission is isotropic and only correlated to the quantity of markers illuminated in the PSF volume of the microscope. In the case of CIDS, we have a highly angularly dependent signal that is correlated to chiral structures and in particular to:

- The intrinsic structural characteristics of the chiral groups, such as radius and pitch;
- The compaction of the chiral groups.

These parameters can change even the sign of the CIDS signal, making it inherently different in nature from the fluorescence one. Finally, while confocal fluorescence allows the optical sectioning of the sample, polarization imaging doesn't have this property, as the polarization state interacts with the whole thickness of the traversed sample without possibility of halting this process for thick and highly complex systems such as cells [151]. In this way, information relative to the whole thickness of the sample is yielded, while the fluorescence image relays information only on the focused plane.

For these reasons, differences are observed in the two modalities, which cannot be directly compared with a simple linear formula. What can be noted is the presence of a double peak structure in the CIDS signal at the periphery of the nucleus, with a negative peak just at the boundary (shown with blue arrows in Figure 45 d)) and a positive one (red arrows in Figure 45 d)) corresponding to the sharp increase in fluorescence signal. We have proposed to interpret the first external peak as the signal deriving from the presence of the nuclear membrane and its perturbing effect. The second, more internal peak in correspondence of the rise in fluorescence signal is attributed to the more compacted heterochromatin areas located at the edge of the nucleus.

3. More elements of the Mueller matrix

As explained in this thesis, the CIDS signal corresponds to the m_{03} element of the Mueller matrix, which is normalized by m_{00}, the total transmitted light intensity. The microscope we have built is an incomplete Mueller polarimeter, meaning not all elements of the matrix can be accessed from

the measurement. Still, more than just m_{03} can be calculated. The images relative to the following elements can be retrieved:

- m_{02}, carrying information on the linear dichroism of the sample;
- m_{22}, element on the diagonal of the matrix and therefore connected to the total transmitted light and its depolarization information;
- m_{23}, carrying information on the linear birefringence.

The images relative to these phenomena can be seen in Figure 46, where the data before normalization is shown for each element.

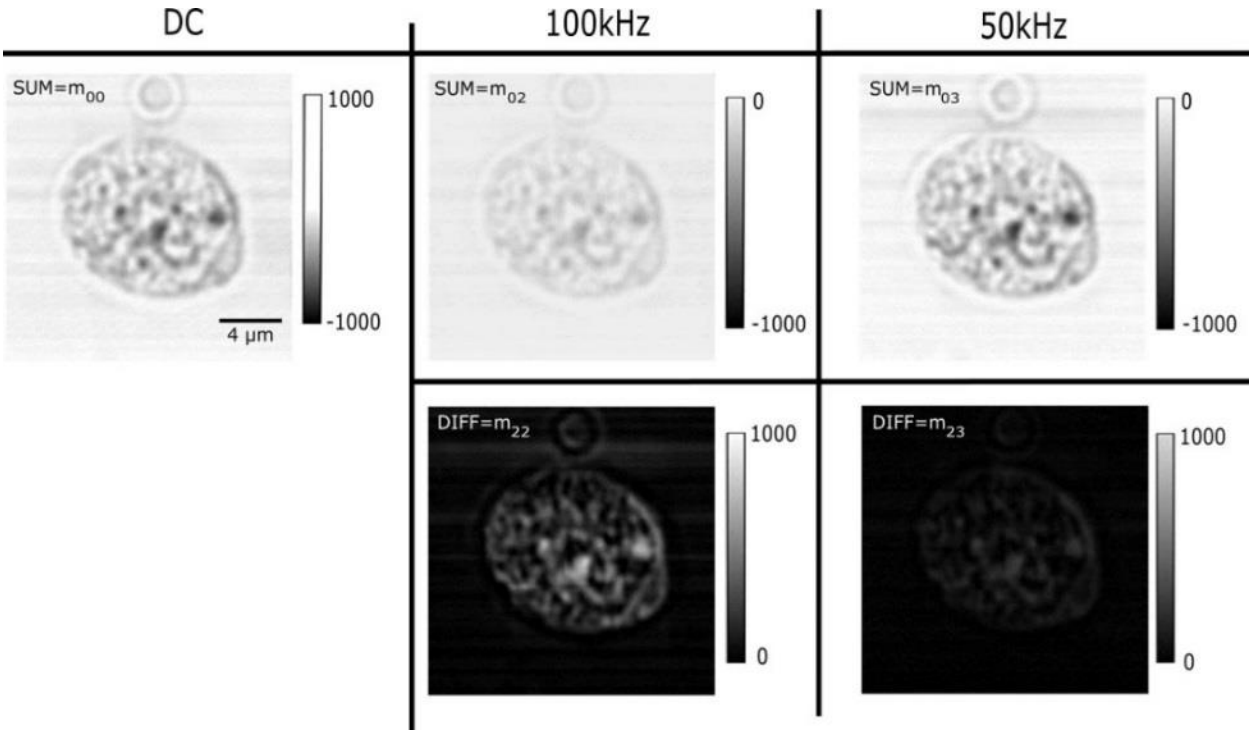

Figure 46 – Images relative to other elements of the Mueller matrix. From the top left: DC signal, corresponding to m

To obtain all of these elements, the data needs to be taken using the lock-in amplifier at both 50kHz (ω) and 100kHz (2ω) (see demonstration in Chapter 1, page 29). The elements can be found in the following way:

- m_{00}: by summation of the DC images, deriving directly from the detector;

- m_{02}: by summation of the 100kHz signal;
- m_{03}: by summation of the 50 kHz signal;
- m_{22}: by summation of the 100kHz signal;
- m_{23}: by summation of the 50 kHz signal;

In Figure 47, the four elements after normalization can be seen. Structuring inside the nucleus can be seen within each element, but with different intensities and signs for each. Of particular interest is noticing that some of the elements do not show the signal deriving from the nuclear membrane. This is partly due to the angular nature of the measurement: the membrane signal may be stronger at angular values that are bigger than those collected by the condenser, leading to the missed collection in our setup. This effect, as well as a deeper study of the properties intrinsically connected to each element could be helpful in better understanding and interpreting the label-free polarization signal, without need of fluorescence confrontation.

Since the focus of this thesis is the CIDS signal deriving from chromatin, a deeper analysis of these elements is beyond its scope, but these promising results invite further research in the future.

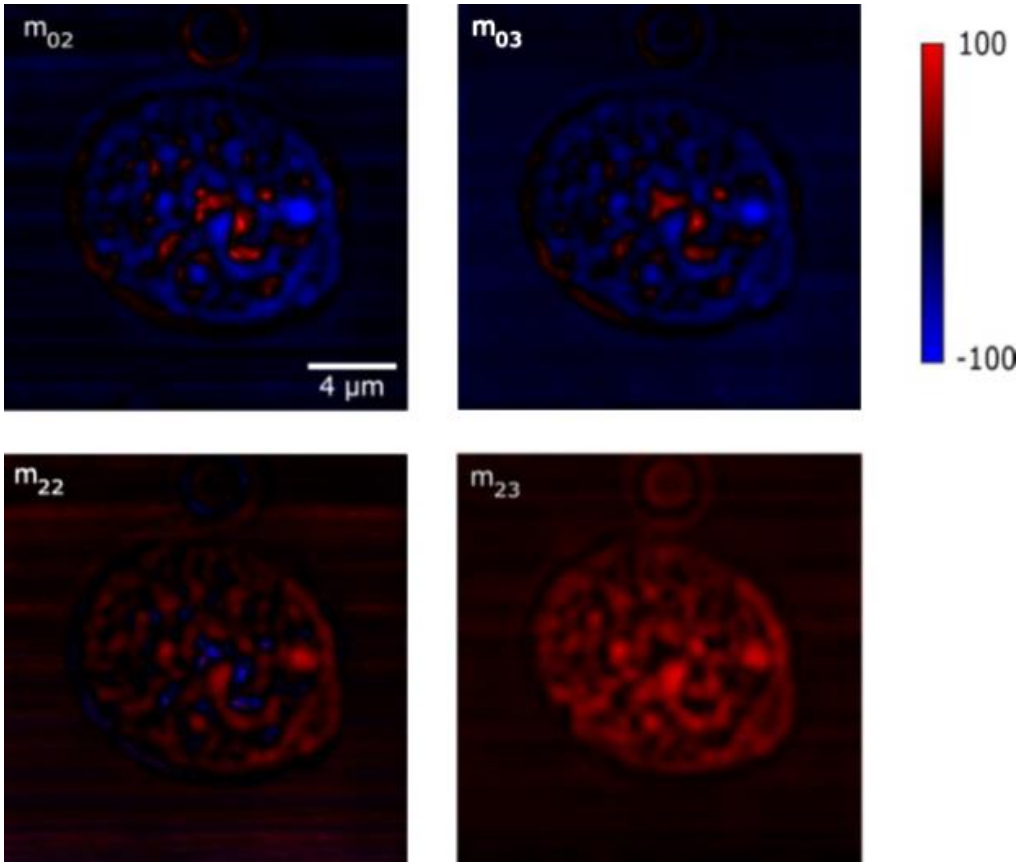

Figure 47 – the four elements of the Mueller matrix that can be extracted from the measurements in our CIDS microscope, after normalization by m_{00}: m_{02} (top left), m_{03} (top right), m_{22} (bottom left) and m_{23} (bottom right).

Part 3: Expansion Microscopy CIDS: ExCIDS

1. Expansion Microscopy (ExM)

Expansion Microscopy (ExM) is a technique which provides a method to obtain “super-resolved” fluorescence images. The technique is not properly a super-resolution methodology because the effective resolution of the microscopes utilized is not enhanced from the diffraction limit. Rather, the resulting increase in ability to resolve smaller structures is due to the physical expansion of the sample itself, and thus of the features of interest. The technique can also be utilized in conjunction with actual super-resolution microscopy techniques to increase the resolving abilities of the setups even more.

This effect is achieved by the use of a polyelectrolyte hydrogel, which is characterized by a high swelling force [163] [164]. The hydrogel links with the biological sample via specific anchors in a homogeneous way, allowing the hydrogel to expand the whole sample isotropically. If there are problems during this step, the linking will not be proper and the final result will produce an anisotropic expansion, resulting in deformations and artifcacts in the resulting image [163] [165]. If the process is properly executed, an expansion factor (EF) of 4-5 times the original size has been achieved with our conditions, allowing to resolve features that were previously impossible to separate due to the diffraction limit of a conventional microscope [166]. The process has been shown in the literature to allow an expansion of up to 20 times [167] [168]. By combining the expansion technique with super resolution microscopy techniques such as STED [166] [169] [170], STORM [171] and SIM [172] [173], the finer details of many biological structures have been revealed. EF is measured by the linear expansion rate of the sample as measured on the scale of the whole gel. An example of such a measurement for a gel at different EF is given in Figure 48.

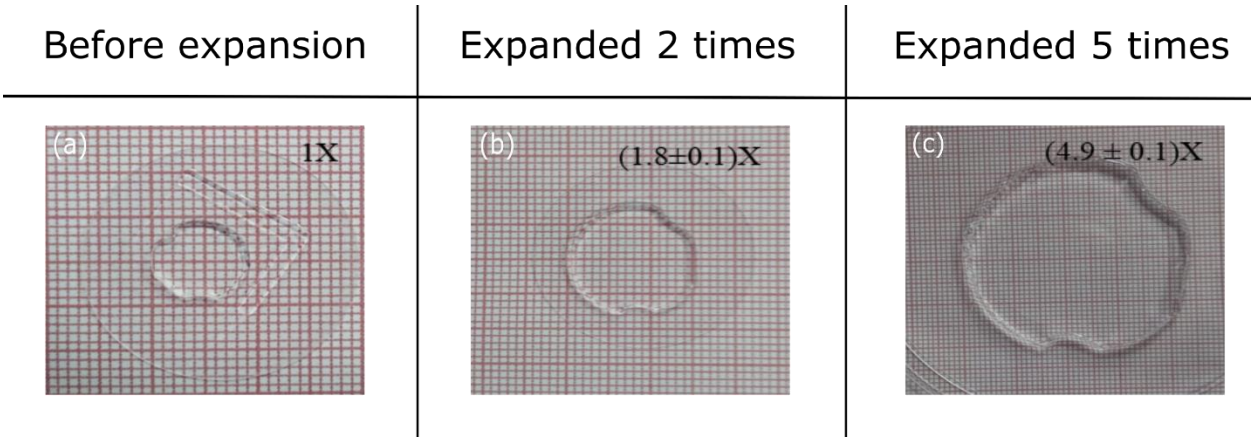

Figure 48 – EF measurement of a gel before expansion (left), at EF 2x (center) and EF 5x (right).

In particular, a very challenging and interesting part of chromatin study is preserving the original structure while studying it to be sure to observe the native conformation. The process of mechanical extraction presents strong stresses as previously explained, with centrifugation at high g values which could potentially change the conformation of the chromatin inside the nucleus. On the other hand, it has been shown that ExM allows to label the chromatin within the nucleus with fluorescent probes while preserving the DNA organization even after the processes of digestion of extra nuclear matter and expansion [165]. The stability and uniformity of ExM was also tested on other structures like the nuclear pore complex, a well known octagonal structure that was found to maintain its shape after expansion [174], a result demonstrated by the use of super resolution fluorescence microscopy.

2. ExM coupling with CIDS: ExCIDS

The ability of CIDS to probe the sample's organization via polarization has many interesting advantages, but unlike fluorescence it doesn't allow for optical sectioning. This means that extraneous matter outside the sample of interest in a different coordinate of the z plane will create an interference with possible spurious signal. The mechanical separation of the nucleus via centrifugation was the first technique we utilized to help us study this system [175]. Still, the high forces required for this process could potentially alter the original conformation of the chromatin inside the nucleus. For this reason, we have utilized expansion microscopy in conjunction with our CIDS microscope in a technique we have called ExCIDS [176].

Expansion microscopy presents a step of digestion where some of the lipids and proteins of the biological sample (for example the cell's external membrane) are eliminated. In this way, we can obtain the equivalent of an isolated nucleus with a much less mechanically stressing procedure than centrifugation. The process is shown in Figure 49. In panel (a), the cell digestion and expansion has not yet started. A stronger scattering component in the signal is registered due to

the additional biological matter that is not the chiral structures of interest in chromatin. This has the result of decreasing the signal to noise ratio (SNR) and muddling the resulting CIDS image. In panel (b) the situation after digestion and expansion: the spurious signal from outside biological matter is absent or at the very least heavily reduced and the resulting SNR and resolving power of the microscope is enhanced.

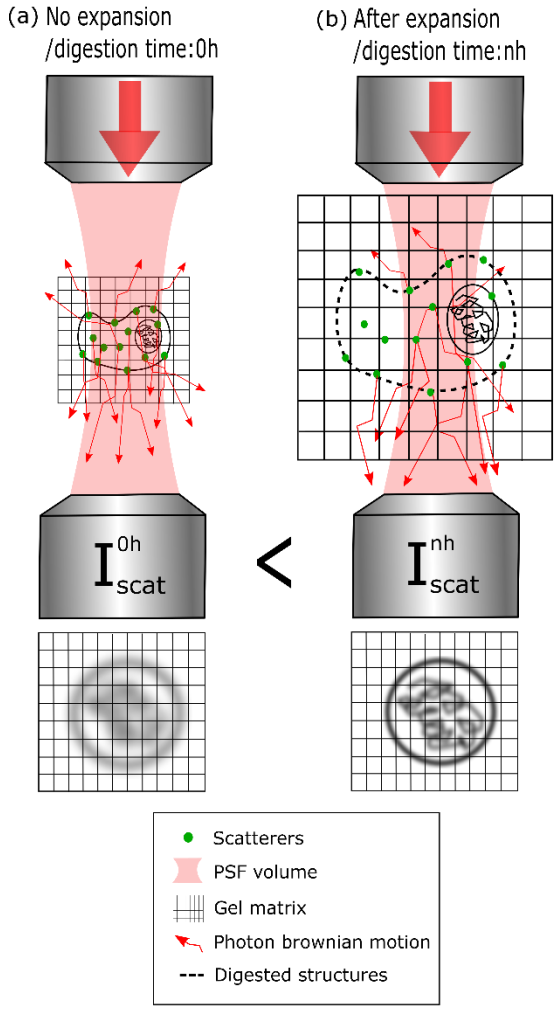

Figure 49 – Illustration of the effect of the process of digestion and expansion on a biological sample like a cell. Before expansion (a) the CIDS signal coming from the chiral structures of interest is masked by other structures, resulting in a lower SNR. After expansion (b) the spurious signal from other biological matter is much less reduced, resulting in better SNR and resolving ability.

Furthermore, the expansion itself provides an improvement in resolving power due to the increase in size, as the technique was originally meant to work even with just fluorescence imaging. That said, more effects need to be taken into account for the label free CIDS imaging technique. This is highlighted in Figure 50. In panel (a) the situation before expansion is shown, while in panel (b) the situation after expansion is presented. Before expansion, the chiral centers

present in chromatin are at their closest. The PSF of the microscope illuminates a good quantity of chiral centers at the same time. This produces a high enough level of signal to be clearly measured, well above the noise threshold, but it makes it harder to resolve some structures. The noise threshold depends greatly on the successful optical alignment of the setup, and as demonstrated previously is about 10% in our CIDS imaging setup. It can be brought down to lower values by improving the alignment, making sure all the optics are clean (as dust and other elements can induce light scattering and errors) and minimizing the sources of noise like vibrations.

Furthermore, by increasing the spacing between chiral structures via the expansion process, the result is that a smaller number of chiral structures are present within the microscope's PSF at a time, which leads to a better resolving power. Furthermore, the geometrical parameters of the chiral structures themselves, namely radius and pitch, are expected to change due to the expansion process. Since the CIDS signal is known to be dependent on them [136], there is further reason to expect an increase in contrast for the CIDS modality. Despite this, possible undesirable effects can arise with high degrees of expansion. If the number of chiral centers within the PSF is too low, the signal may become too close to the noise threshold and thus make it impossible to measure it.

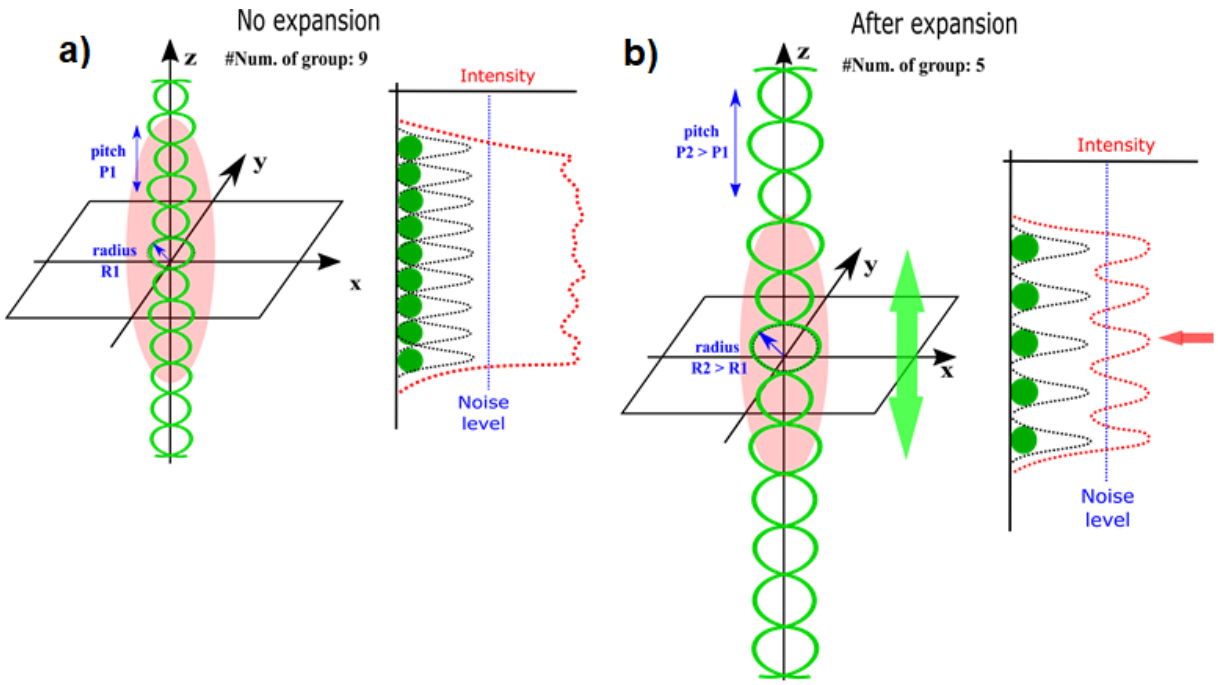

Figure 50 – The effect of expansion on CIDS signal. Before expansion (a) the chiral structures of chromatin are close and a good number of them is contained inside the PSF. After expansion (b) a smaller number is contained within the PSF, increasing resolving ability but also possibly leading to a SNR that is closer to the noise level the more expanded the sample is.

Finally, the increase in size also has an effect on the fluorescence modality: by having a lower density of fluorescent markers the dose of light illumination required to have a good signal increases.

To characterize the expansion process we can use the expansion factor (EF) and expansion time. EF corresponds to the factor of linear growth in the sample after expansion (e.g. 2x EF means each linear dimension of the sample has grown by 2 times), while expansion time is the time the sample is left to complete the expansion step.

3. ExM sample preparation

To demonstrate the results of our technique, we have utilized HEK cell samples, as a parallel to our previous experiments with centrifugation of the nuclei where the same kind of cells were used. As with the previous methodology, the chromatin inside the nuclei needs to be marked with fluorescent probes. For this purpose, we have utilized the ExM protocol variant proposed by Chozinsky et al. [164]. The HEK cells were cultured in DMEM with the addition of 10% Fetal Bovine Serum and 1% pen/strep and glutamine. To be able to image the sample in our setup, the cells were fixed with 4% PFA for a time of 10 minutes at room temperature. The sample is then incubated in a Hoechst solution at a dilution of 1:1000 for another 10 minutes. Functionalization of the sample is conducted via a solution of 25 nM Methacrylic acid N-Hydroxy Succinimidyl Ester (MA-NHS) for a time of 60 minutes at ambient temperature. After this step, the sample is incubated in the gelation solution composed of 2M NaCl, 2.5% acrylamide (wt/wt), 0,15% (wt/wt) N,N0-methylenebisacrylamide, 8,625% (wt/wt) Sodium Acrylate, 0,2% tetramethylene diamine (TEMED) and 0,2% (wt/wt) ammonium persulfate (APS) in deionized water. When the gelation step is over, the sample is incubated within the digestion buffer, composed of 1x TAE buffer, 0,5% Triton X-100, 0,8M guanidine HCl and 8 units/mL Proteinase K. This operation is performed for a different amount of time depending on the digestion time required by the sample, ranging from 4 hours to overnight for our experiments. The digestion step eliminates the lipids and proteins from the cellular membrane and allows us to obtain the equivalent of an isolated nucleus.

For some samples, the digestion step is skipped, to identify a base with which we can compare the results of the digestion and expansion of the nuclei.

4. ExCIDS on HEK cells: effect of the Expansion Factor

We have studied the effect of the Expansion Factor on samples of whole HEK cells. The results are shown in Figure 51, where the CIDS and fluorescence data for two different cells are shown at different EF. In particular, the first set of data on the left is relative to a cell before expansion (EF 1x), while the set on the right is relative to a post expansion sample with 5x EF, the maximum value we obtained with our protocol. Image a) and e) are relative to the respective CIDS signals, images b) and f) are relative to the fluorescence, c) and g) are the merged CIDS and fluorescence

image for each cell and d) and h) are the line profiles for CIDS (blue) and fluorescence (green) relative to the yellow line in c) and g).

The equivalent optical resolution due to expansion utilizing our 100x/1.3NA objective is 300nm before expansion and 60 nm at 5x EF ($R_{OBJ}/5$). It has to be noted that due to difficulties in finding the same cell in the setup after expansion, the images are relative to two different cells, but in the future it would be of great interest to repeat the experiments with the same cell if possible.

As can be seen by Figure 51 a) and c), before expansion there is a strong component in the CIDS signal outside the cell nucleus and the chromatin, as evidenced by the lack of correspondence between the CIDS signal and the fluorescence. The main feature highlighted in our previous work on centrifuged nuclei [175] can still be seen in the CIDS profile in panel d). It consists in the sharp peaked structures at the edge of the nucleus, in which we have attributed the first peak to the signal coming to the nuclear membrane, while the second one is attributed to the more compacted heterochromatin region that can be found at the edge of the nucleus [177]. For the undigested cell, we have an even higher peak signal externally, probably corresponding to the spurious signal due to the external cellular membrane. The membrane distortion is due to the edge effects relative to using a high NA objective in a polarimetric technique.

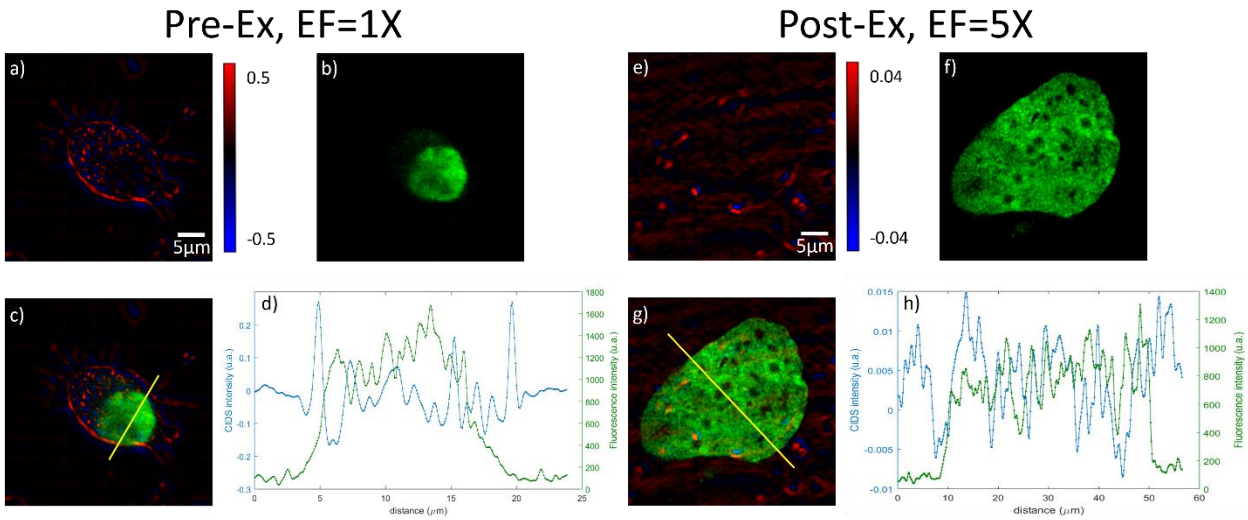

Figure 51 – The Normalized images of different HEK cells labeled with Hoechst for (a, b, c, d) the pre-expansion and (e, f, g, h) at the maximum expansion. More particularly, (a, e) are the CIDS images; (b, f) are the Hoechst images; (c, g) are the superposed CIDS and Hoechst images to better gauge the position of the nucleus; (d, h) are the line profiles corresponding to the yellow lines traced in (c) and (g) respectively.

In Figure 51 f) the effect of the expansion can be clearly seen. First of all the nucleus is much bigger than the unexpanded one. It is in fact bigger than the whole original cell, following the 5x EF. The fluorescence is relative only to the chromatin inside the nucleus and thus the signal is sure to

correspond to that. In Figure 51 e) we can see the effect that the expansion has had on the nucleus in the CIDS imaging modality. The CIDS signal is very low when compared to the background. The scale of the image is about one order of magnitude smaller than the scale of the pre-expansion image and the signal of the nucleus can barely be distinguished at points from the background signal. This is due to the increase in size reducing the density and possibly changing the geometrical parameters of the chiral structures, like radius and pitch, too much. This leads to a sharp decrease in signal to noise ratio. This can be seen also from the line profile in Figure 51 h). Here the dynamics of the CIDS signal are much more enhanced, but this is probably in good part due to the variance of the background noise, as the same signal can be found also outside the nucleus (delimited by the fluorescence signal) with the same intensity and dynamics as the internal one.

To obtain a more statistically relevant description of the process, we performed a different analysis considering the whole area of the nucleus. In Figure 52 the 3D histogram distribution relative to the CIDS and fluorescence combined signal is shown for both the pre expansion (red) and post expansion (blue) samples presented in Figure 51. The background contribution is removed by utilizing the fluorescence area as a mask for both fluorescence and CIDS to cut the images, to be sure to obtain data only coming from the chromatin area. In this way, the contribution of CIDS signal from outside the nucleus is eliminated, but it should be remembered that the 3D signal, deriving from the presence of biological matter above and below along the z axis cannot be removed with this polarization based technique. The histograms have then been normalized to make comparison easier. This means that a zero value in the CIDS signal signifies an absence of chiral centers, while 1 is the highest possible value.

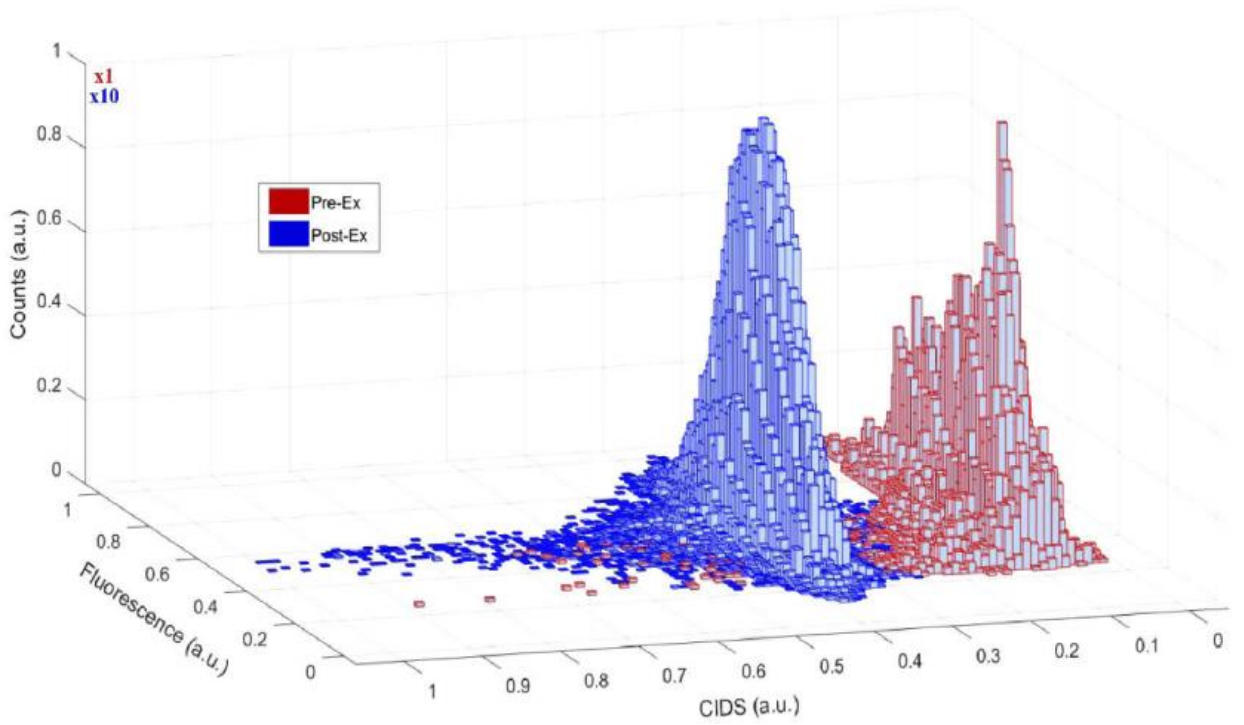

Figure 52 – Histogram of the normalized pixel intensity values for CIDS and fluorescence for the data relative to the pre (red) and post (blue) expansion samples from Figure 51.

The difference in values between the two expansion steps are marked. First of all, looking at the fluorescence, its distribution becomes Gaussian in the 5x EF sample, as opposed to the more erratic values of the pre expansion sample. This phenomenon is probably due to the contrast enhancement in chromatin as a consequence of the expansion process. Regarding CIDS signal, we can see that the distribution in the 5x EF image is much smoother, with less erratic features. This can be attributed to various effects. In the first place, a positive effect can be due to the decrease in spurious signal coming from the biological matter present in the pre-expansion sample. In this case though, with such a high EF, as previously explained the very low SNR and importance of the background signal could explain the lack of particular features.

The result of these measurements indicates that a 5x EF is too extreme for the CIDS modality. For this reason, further experiments were conducted at 2x EF, a value that we determined to be ideal to study cell nuclei with CIDS microscopy.

5. ExCIDS on HEK cells: effect of the digestion time

The effect of digestion time was studied on HEK cells marked with Hoechst fluorescent label and expanded at 2x EF for different times (except the first one, undigested and unexpanded). In particular, results for three different samples are shown in Figure 53. The first row, with panels a)

through d), is relative to the data for no digestion (undigested and unexpanded cell). The second row, panels e) through h), is relative to 4 hours of digestion. Finally, the last row, panels i) through l), is relative to an overnight digestion process. Panels a), e) and i) are relative to the CIDS signal, panels b), f) and j) are relative to the Hoechst fluorescence, panels c), g) and k) are the merged CIDS and fluorescence image while panels d), h) and l) are the line profiles for CIDS (blue) and fluorescence (green) relative to each sample's yellow line in the merged image.

First of all, it's worth noting that the undigested and unexpanded sample in the first row presents a very similar print when compared to the same kind of sample in the previous section of this work. In particular, from Figure 53 c), we can see how there is a big CIDS signal component coming from outside the nucleus, delimited by the fluorescence signal. This is due to the scattering and polarization interference caused by the biological matter surrounding the nucleus. Big CIDS peaks in correspondence of the cellular membrane make the interpretation of the CIDS signal harder. There is a clear improvement in the general signal features when observing the sample digested 4 hours. In Figure 53 g) in particular we can see how the nucleus and cell in general show a bigger size than the previous one, as expected from the 2x measured EF. CIDS signal from the whole cell is still present, but decidedly smaller in intensity when compared to the undigested sample. Furthermore, the bigger peaked structures in the line profile now correspond more to the fluorescence profile, signifying a closer accordance between CIDS and fluorescence and thus of CIDS signal coming predominantly from the chiral structures in the chromatin.

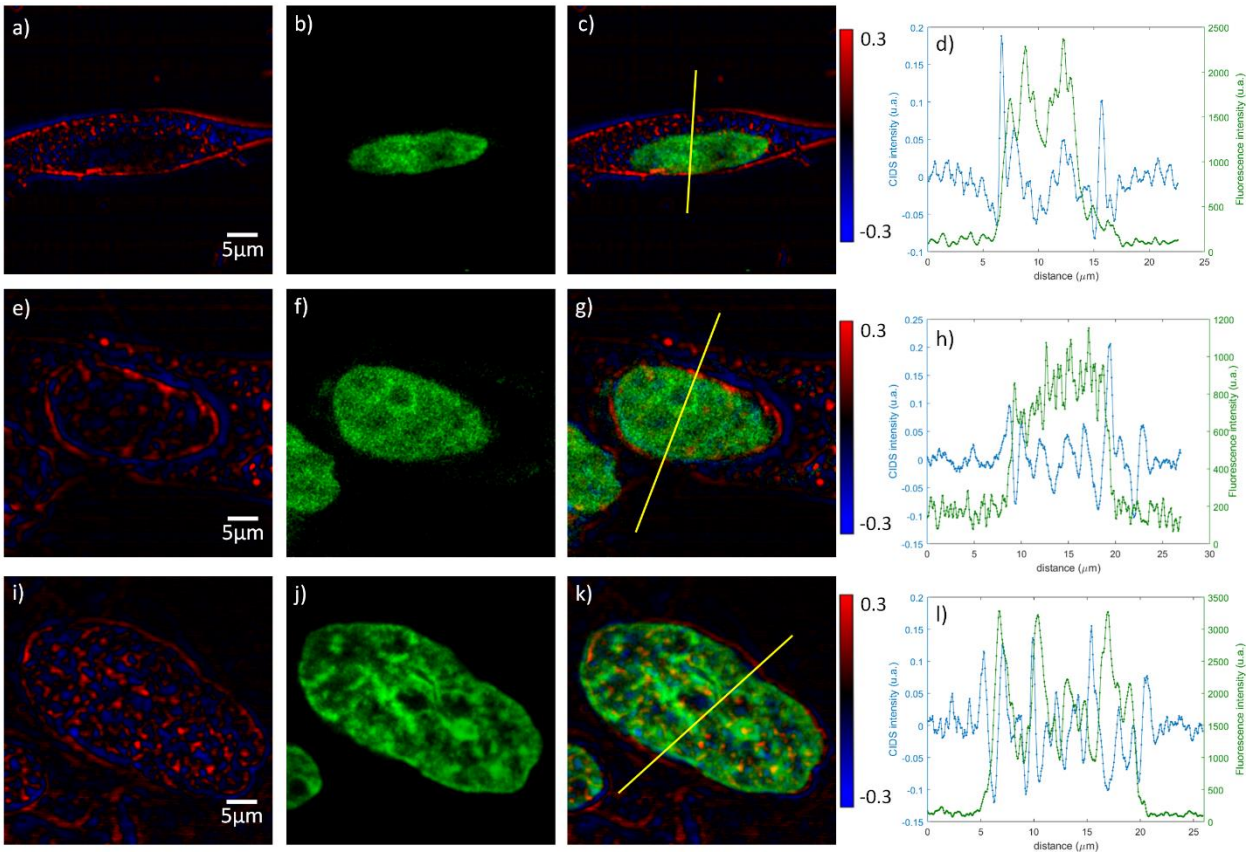

Figure 53 – Three HEK cells at different digestion times. a), b), c), d): no digestion, no expansion. e), f), g), h): 2x EF, 4 hours digestion. i), j), k), l): 2x EF, overnight digestion. For each row, the first image is relative to the CIDS, signal, the second to the fluorescence of the Hoechst marker, the third is the merge of the previous two modalities and the fourth is the line profile relative to the yellow line in the merged image.

Finally, in Figure 53 k) we can clearly see the effect of an overnight digestion in the HEK cell imaging. The correspondence between CIDS signal and fluorescence is much higher than in both previous steps, with almost no CIDS signal coming from outside the nucleus of this cell. When we focus our attention on the line profile in panel l), the peaked structures at the periphery of the nucleus are still present, as expected from our centrifuged nuclei experiments. As previously explained, the more external peak is attributed to the nuclear membrane signal due to distortion effects, while the more internal one is due to the more compacted heterochromatin area in the external region of the nucleus. Furthermore, when compared with the undigested and 4 hours digested samples, the overnight digested one clearly presents a higher level of dynamics in the CIDS signal inside the nucleus, possibly due to a higher degree of sensitivity due to the lack of confounding factors and spurious signal from the biological matter surrounding the nucleus.

The 3D histogram analysis was conducted on these three samples as well and is shown in Figure 54. The image shows the pixel distribution of the fluorescence in function of the CIDS signal. One of the main features that can be seen is that the fluorescence signal transitions towards a more

Gaussian profile when moving from the undigested sample to the 4 hours digested one. This effect is probably due to the expansion process. CIDS signal follows a similar pattern, this time due to the digestion eliminating part of the biological matter responsible for the scattering not coming from chromatin that disturbed the CIDS signal acquisition. The correlation between the two modalities is also stronger after digestion, signifying a better accordance. Since the confocal fluorescence signal is not perturbed by the presence of the cellular structure before digestion, but is only related to the actual chromatin conformation, the increase in accordance with CIDS is a good indicator of the increase in CIDS signal coming from chromatin only relative to the total registered CIDS signal.

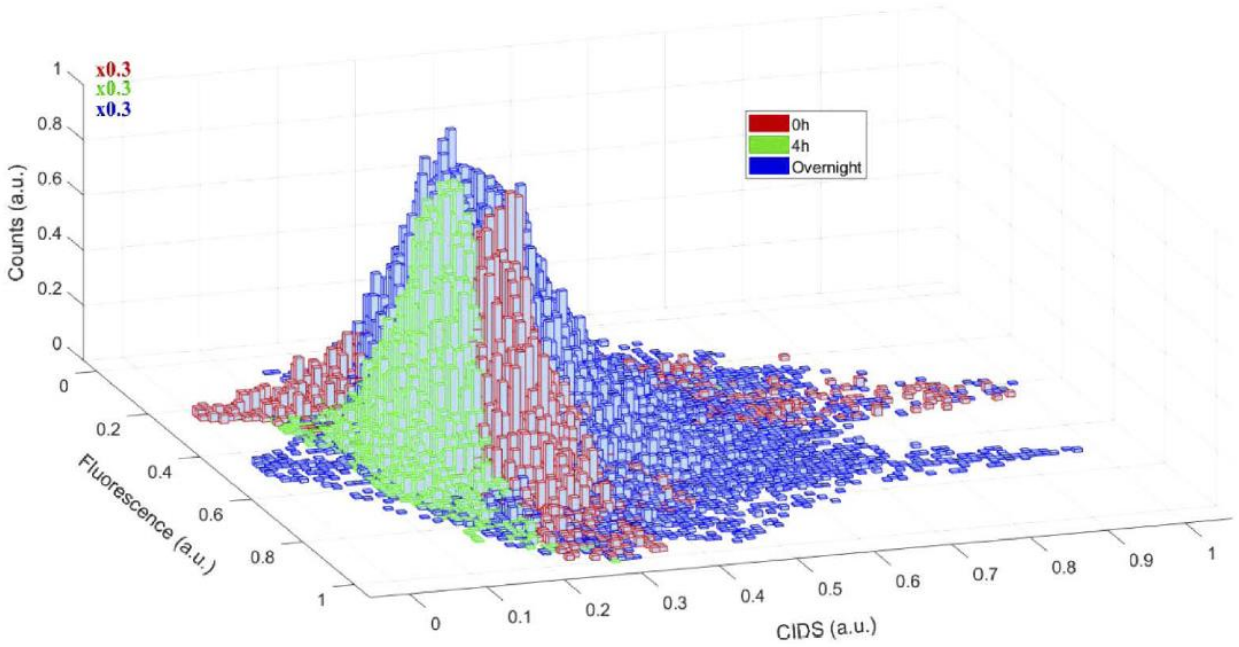

Figure 54 - Histogram of the normalized pixel intensity values for CIDS and fluorescence for the data relative to the undigested (red), 4 hours digestion (green) and overnight digestion (blue) expansion samples from Figure 53.

Finally, as expected the overnight sample presents the highest degree of correlation between the two modalities.

From this data it's clear how the digestion time is a fundamental factor in ExCIDS imaging and how an overnight digestion offers the best results, showing an almost complete elimination of external biological matter and thus of its interference in CIDS signal. The EF utilized for these experiments was 2x. Such an EF with overnight digestion seem to be the ideal conditions to work with this kind of technique and samples.

Conclusions

In this chapter the basics of CIDS microscopy and its results have been shown. An overview of the birth of CIDS imaging techniques and their first applications to cell and chromatin imaging has been reported. The techniques themselves and the most common experimental configurations have been explained, including some of their applications. After this, our confocal fluorescence/CIDS microscope has been presented, as well as the calibration process and all of its procedures.

Results of the study of HEK cells with the aforementioned microscope have been shown, highlighting the capability of CIDS to image chromatin conformation on extracted nuclei. In particular, the signal coming from the heterochromatin close to the edge of the nucleus can be distinguished. Furthermore, thanks to the information acquired by our microscope, the images relative to more elements of the Mueller matrix can be calculated, allowing the extraction of even more information from the sample.

Finally, the CIDS technique was combined with expansion microscopy (ExM) to obtain an approach that we have named ExCIDS. The motivation behind this choice is the need for CIDS to eliminate as much biological matter as possible outside the chromatin, while maintaining its original structure. For this reason the digestion process performed during expansion microscopy has been deemed more appropriate for our technique than the more violent centrifugation process previously utilized for nuclei isolation. The results have shown that expansion factor EF plays a fundamental role in our ability to see the cell with CIDS, making 2x EF the ideal EF for CIDS imaging. Digestion time is also a very important parameter: the longer the digestion, the less spurious signal from biological matter, obtaining the best results with overnight digestion over only 4 hours. ExCIDS at 2x EF overnight digestion is therefore a promising technique to study chromatin configuration in fixed cells.

General Conclusions

This thesis has been focused on the label-free study of chromatin organization via the use of the circular polarization states, and in particular the interpretation of Circular Intensity Differential Scattering (CIDS) signal. The CIDS signal was for the first time acquired in a laser scanning microscope, along with the confocal fluorescence signal. A photoelastic modulator was utilized to generate the needed circular left and right polarization states in a fast way (50 kHz frequency). A lock-in amplifier was synchronized with the reference frequency of the PEM to obtain the CIDS signal pixel by pixel in real time at the scanning speed (about 40 µs pixel dwell time). The sensitivity of the lock-in amplifier also allowed to obtain a better signal to noise ratio on the low intensity CIDS signal.

To analyze the data and model the setups, the Stokes/Mueller formalism for polarized light was utilized. This formalism has been used since the start of CIDS study and is of interest for various reasons. In the first place it allows to describe all possible polarization states of light and all possible polarization properties of a sample or object, including depolarization. In the second place, it's a formalism that is easy to utilize operationally as all measured quantities are relative to light intensities, one of the easiest measurements to make.

To do this, I built, aligned and calibrated three main setups:

- A spectroscopic one-point angular CIDS setup;
- A Fourier plane imaging setup;
- A CIDS/confocal-fluorescence microscope.

The spectroscopic angular setup is based on one of the first implementations of CIDS measurement, where solutions of the molecules/biological systems of interest were used as samples. The circular polarization states were generated by a resonant device (a Photoelastic Modulator) at a frequency of 50kHz. By utilizing Mueller calculus, the data relative to the m_{03} element of the Mueller matrix, corresponding to CIDS in the case where the wavelength of the laser utilized is outside the absorption band.

We executed the alignment of the setup thanks to a linear polarizer sample, which was measured as it was rotated and the results were compared with theoretical modeling. Afterwards, the setup was validated with water solutions of well-known chiral molecules (Arabinose), demonstrating its sensibility to chiral structures when compared to control samples and the expected dependency on the concentration. The main achievement of the setup was to measure the CIDS signal of isolated nuclei (chromatin chiral structures), clearly distinguishable from the control sample of polystyrene microspheres (no chiral structures). This is achieved on an automated setup controlled by a labview routine, with a measurement time of the order of minutes.

Since the main drawback in terms of measurement time for the angular CIDS setup is due to the motorized movement of the arm and sequential measurement at all angles, we proposed next to utilize Fourier imaging coupled with polarization control to obtain the angular information in a fast way and without the need of moving parts. By having a beam splitter and a detector positioned at the Fourier plane in one arm and at the real plane in the other, we can obtain both the real space image and the Fourier image of the sample at the same time. In the Fourier image, each pixel corresponds to a different scattering angle, with an angular FOV ranging from about 10° to about 120° depending on the angle of acceptance of the objective utilized. The setup was tested on microspheres and simulations of Mie scattering theory were compared with the experimental data, finding good accordance.

Finally, I implemented the same configurations utilized to generate and analyze the polarization in the one-point angular CIDS setup on a commercial confocal microscope. In this way I was able to obtain a multimodal confocal fluorescence/CIDS imaging microscope. Polarization control was fitted on a commercial confocal microscope to obtain CIDS contrast at the same time as the fluorescence. A lock-in amplifier was implemented in this setup to allow the real time extraction of the signal and to obtain a better signal to noise ratio for the naturally small CIDS signal. The reference frequency of the PEM utilized to generate the polarization states is fed into the lock-in, to allow to extract the AC part of the signal measured by the detectors. When united with the DC part, coming directly from the detectors, this allows to calculate the normalized CIDS signal pixel-by-pixel for any sample, while acquiring the confocal fluorescence signal at the same time. The interest in acquiring the fluorescence signal is the validation of the CIDS imaging technique and the correlation between both modalities, to find ways to interpret the CIDS signal so that in the future fluorescence may be unnecessary to interpret the data, leading to a mature and independent label-free technique.

This setup has allowed us to image isolated HEK cell nuclei. From the comparison of CIDS and fluorescence signal (chromatin marked), we were able to distinguish a clear double-peaked feature at the edge of the nuclear membrane in the CIDS signal, which was correlated with the increased fluorescence signal. We have attributed the external peak to the distortion due to the presence of the nuclear membrane, while the internal peak has been attributed to the more compacted area of heterochromatin present there, as confirmed by the intense fluorescence peak.

A development of CIDS imaging was the implementation of expansion microscopy (ExM) in a novel approach that we have named ExCIDS. ExCIDS allows to have a two main advantages from the combination of both techniques:

- Increase of the optical resolution due to expansion of the sample;
- Digestion of the external parts of the cell (cytoskeleton, cytoplasm), leading to an increase in CIDS signal to noise ratio.

The two main parameters in ExCIDS were proven to be the expansion factor (number of times each linear dimension of the sample is expanded) and the digestion time. We have shown that the ideal EF is 2x, as greater EFs (ex. 5x) lead to the loss of CIDS signal due to the sharp decrease in density of chiral structures. As for the expansion time, it was shown that an overnight digestion offers the ideal results, eliminating all the biological matter outside the nucleus and thus the spurious CIDS signal coming from the scattering of light with eternal structures.

CIDS has thus demonstrated its powerful applications in the study of biological samples in a label-free way, in particular on the structure of chromatin.

The future work regarding this technique, which is in its preliminary stages in the moment of this writing, is its implementation in a multimodal microscope. This kind of setup will continue the work I have put in implementing CIDS with fluorescence by adding more modalities, like ptychography, super resolution fluorescence techniques such as STED, or even a complete Mueller microscope to increase the polarization information. In this way, the sample of interest can be studied with the most appropriate technique and different kinds of information, only obtainable with one technique or the other, can be mixed and matched depending on the needs and the application.

The main object of study, at least at the start, will still be chromatin, but such a setup will have a great flexibility that will allow it to image any biological sample. A robust machine learning algorithm will be trained on each sample type and will drive the setup to utilize the most appropriate technique in each case, greatly increasing the speed of data acquisition and analysis.

This kind of setup will increase even further the understanding of the CIDS signal of chromatin, as its signal will be compared with that of numerous other techniques. This will both allow a better synergy of CIDS with the other techniques and a better understanding of the CIDS signal itself, eliminating the need for a fluorescence counterpart to the signal to extract information, thus creating a true, practical label-free approach to chromatin imaging without the need of fluoresce comparison.

Bibliography

[1] C. M. J., "VIII. A dynamical theory of the electromagnetic field," *Philos. Trans. R. Soc. London*, 1865, doi: 10.1098/rstl.1865.0008.

[2] R. Clark Jones, "A New Calculus for the Treatment of Optical Systems," *J. Opt. Soc. Am.*, 1941.

[3] C. Kilchoer, N. Abdollahi, U. Steiner, I. Gunkel, and B. D. Wilts, "Determining the complex Jones matrix elements of a chiral 3D optical metamaterial," *APL Photonics*, vol. 4, no. 12, p. 126107, 2019, doi: 10.1063/1.5127169.

[4] H. R. Lee *et al.*, "Digital histology with Mueller microscopy: how to mitigate an impact of tissue cut thickness fluctuations," *J. Biomed. Opt.*, vol. 24, no. 7, pp. 1–9, Jul. 2019, doi: 10.1117/1.JBO.24.7.076004.

[5] J. J. G. Perez and R. Ossikovski, *Polarized Light and the Mueller Matrix Approach*. Routledge, 2016.

[6] G. G. Stokes, "On The Composition And Resolution Of Streams Of Polarized Light From Different Sources," *Trans. Cambridge Philos. Soc.*, vol. IX, 1852.

[7] J. S. Tyo, D. L. Goldstein, D. B. Chenault, and J. A. Shaw, "Review of passive imaging polarimetry for remote sensing applications," *Appl. Opt.*, vol. 45, no. 22, pp. 5453–5469, 2006, doi: 10.1364/AO.45.005453.

[8] A. Diaspro, G. Radicchi, and C. Nicolini, "Polarized light scattering: a biophysical method for studying bacterial cells," *IEEE Trans. Biomed. Eng.*, vol. 42, no. 10, pp. 1038–1043, Oct. 1995, doi: 10.1109/10.464379.

[9] H. Mueller, "The Foundation of Optics," *J. Opt. Soc. Am.*, vol. 38, p. 661, 1949.

[10] S. Lu and R. A. Chipman, "Interpretation of Mueller matrices based on polar decomposition RETARDANCE : A REVIEW," vol. 13, no. 5, pp. 1106–1113, 1996.

[11] S. Kumar and R. Simon, "Characterization of Mueller matrices in polarization optics," vol. 88, pp. 464–470, 1992.

[12] S. Savenkov, R. Muttiah, E. Oberemok, and A. Klimov, "Incomplete active polarimetry: Measurement of the block-diagonal scattering matrix," *J. Quant. Spectrosc. Radiat. Transf.*, vol. 112, no. 11, pp. 1796–1802, 2011, doi: 10.1016/j.jqsrt.2011.02.017.

[13] J. W. Lewis, R. A. Goldbeck, D. S. Kliger, X. Xie, R. C. Dunn, and J. D. Simon, "Time-resolved circular dichroism spectroscopy: Experiment, theory, and applications to biological systems," *J. Phys. Chem.*, vol. 96, no. 13, pp. 5243–5254, 1992, doi: 10.1021/j100192a016.

[14] T. Dartigalongue and F. Hache, “Precise alignment of a longitudinal Pockels cell for time-resolved circular dichroism experiments,” *J. Opt. Soc. Am. B*, vol. 20, no. 8, p. 1780, 2003, doi: 10.1364/josab.20.001780.

[15] T. C. Oakberg, “Modulators With Lasers,” vol. 34, no. 6, pp. 1545–1550, 2014.

[16] Y. Shindo and Y. Ohmi, “Problems of CD Spectrometers. 3. Critical Comments on Liquid Crystal Induced Circular Dichroism,” *J. Am. Chem. Soc.*, vol. 107, no. 1, pp. 91–97, 1985, doi: 10.1021/ja00287a017.

[17] A. J. Hunt and D. R. Huffman, “A new polarization-modulated light scattering instrument,” *Rev. Sci. Instrum.*, vol. 44, no. 12, pp. 1753–1762, 1973, doi: 10.1063/1.1686049.

[18] KEMP JC, “Piezo-Optical Birefringence Modulators. New Use for a Long- Known Effect,” *J Opt Soc Amer*, vol. 59, no. 8 pt 1, pp. 950–954, 1969, doi: 10.1364/josa.59.000950.

[19] R. M. A. Azzam, “Propagation of partially polarized light through anisotropic media with or without depolarization: A differential 4x4 matrix calculus,” *J Opt Soc Am*, vol. 68, no. 12, pp. 1756–1767, 1978, doi: 10.1364/JOSA.68.001756.

[20] J. Schellman and H. P. Jensen, “Optical Spectroscopy of Oriented Molecules,” *Chem. Rev.*, vol. 87, no. 6, pp. 1359–1399, 1987, doi: 10.1021/cr00082a004.

[21] L. A. Nafie, “Dual polarization modulation: a real-time, spectral-multiplex separation of circular dichroism from linear birefringence spectral intensities,” *Appl. Spectrosc.*, vol. 54, no. 11, pp. 1634–1645, 2000, doi: 10.1366/0003702001948664.

[22] R. C. Thompson, J. R. Bottiger, and E. S. Fry, “Measurement of polarized light interactions via the Mueller matrix: errata,” *Appl. Opt.*, vol. 19, no. 16, p. 2657, 1980, doi: 10.1364/ao.19.002657.

[23] O. Arteaga, Z. El-Hachemi, and R. Ossikovski, “Snapshot circular dichroism measurements,” *Opt. Express*, vol. 27, no. 5, p. 6746, 2019, doi: 10.1364/oe.27.006746.

[24] S. Alali, A. Gribble, and I. Alex Vitkin, “Rapid wide-field Mueller matrix polarimetry imaging based on four photoelastic modulators with no moving parts,” *Opt. Lett.*, vol. 41, no. 5, p. 1038, 2016, doi: 10.1364/ol.41.001038.

[25] M. R. Shcherbakov *et al.*, “Ultrafast polarization shaping with fano plasmonic crystals,” *Phys. Rev. Lett.*, vol. 108, no. 25, pp. 1–5, 2012, doi: 10.1103/PhysRevLett.108.253903.

[26] T. Narushima and H. Okamoto, “Circular Dichroism Microscopy Free from Commingling Linear Dichroism via Discretely Modulated Circular Polarization,” *Sci. Rep.*, vol. 6, no. October, pp. 1–10, 2016, doi: 10.1038/srep35731.

[27] O. Arteaga, J. Freudenthal, B. Wang, and B. Kahr, “Mueller matrix polarimetry with four photoelastic modulators: Theory and calibration,” *Appl. Opt.*, vol. 51, no. 28, pp. 6805–6817, 2012, doi: 10.1364/AO.51.006805.

[28] M. F. Maestre and J. E. Katz, “A circular dichroism microspectrophotometer,” *Biopolymers*,

vol. 21, no. 9, pp. 1899–1908, 1982, doi: 10.1002/bip.360210916.

[29] A. S. Schneider, M. J. Schneider, and K. Rosenheck, “Optical activity of biological membranes: scattering effects and protein conformation.,” *Proc. Natl. Acad. Sci. U. S. A.*, vol. 66, no. 3, pp. 793–798, 1970, doi: 10.1073/pnas.66.3.793.

[30] C. Reich, M. F. Maestre, S. Edmondson, and D. M. Gray, “Circular Dichroism and Fluorescence-Detected Circular Dichroism of Deoxyribonucleic Acid and Poly[d(A-C)*d(G-T)] in Ethanolic Solutions: A New Method for Estimating Circular Intensity Differential Scattering,” *Biochemistry*, no. 19, pp. 5208–5213, 1980.

[31] R. M. A. Azzam, “Optimal beam-splitters for the division-of-amplitude photopolarimeter,” *Opt. Acta (Lond).*, vol. 32, no. 11, pp. 1407–1412, 1985, doi: 10.1080/713821665.

[32] R. M. A. Azzam, I. M. Elminyawi, and A. M. El-Saba, “General analysis and optimization of the four-detector photopolarimeter,” *J. Opt. Soc. Am. A*, vol. 5, no. 5, p. 681, 1988, doi: 10.1364/josaa.5.000681.

[33] J. L. Pezzaniti and D. B. Chenault, “A division of aperture MWIR imaging polarimeter,” *Polariz. Sci. Remote Sens. II*, vol. 5888, p. 58880V, 2005, doi: 10.1117/12.623543.

[34] O. Arteaga, “Mueller matrix polarimetry of anisotropic chiral media,” Universitat de Barcelona, 2010.

[35] F. Snik *et al.*, “An overview of polarimetric sensing techniques and technology with applications to different research fields,” *Polariz. Meas. Anal. Remote Sens. XI*, vol. 9099, p. 90990B, 2014, doi: 10.1117/12.2053245.

[36] N. J. Pust, J. A. Shaw, P. Full, S. Polarimetric, and A. Imagers, “Dual-field imaging polarimeter using liquid crystal variable retarders,” 2006.

[37] P. Deschamps *et al.*, “The POLDER Mission : Instrument Characteristics and Scientific Objectives,” vol. 32, no. 3, 1994.

[38] B. Cairns, E. E. Russell, J. D. LaVeigne, and P. M. W. Tennant, “Research scanning polarimeter and airborne usage for remote sensing of aerosols,” in *Polarization Science and Remote Sensing*, 2003, vol. 5158, pp. 33–44, doi: 10.1117/12.518320.

[39] R. J. Peralta *et al.*, “Aerosol Polarimetry Sensor for the Glory Mission,” vol. 6786, pp. 1–17, 2007, doi: 10.1117/12.783307.

[40] D. J. Diner *et al.*, “First results from a dual photoelastic-modulator-based polarimetric camera,” vol. 49, no. 15, 2010.

[41] G. Van Harten *et al.*, “Prototyping for the Spectropolarimeter for Planetary EXploration (SPEX): calibration and sky measurements,” vol. 8160, pp. 1–12, 2011, doi: 10.1117/12.893741.

[42] M. Rodenhuis, H. Canovas, S. V Jeffers, M. D. J. Ovelar, L. Homs, and M. Min, “The Extreme Polarimeter : Design , Performance , First Results & Upgrades,” vol. 8446, pp. 1–18, 2012,

doi: 10.1117/12.927203.

[43] F. Snik and C. U. Keller, “Astronomical Polarimetry: Polarized Views of Stars and Planets,” in *Planets, Stars and Stellar Systems: Volume 2: Astronomical Techniques, Software, and Data*, T. D. Oswalt and H. E. Bond, Eds. Dordrecht: Springer Netherlands, 2013, pp. 175–221.

[44] H. Schmid *et al.*, “Tests of the demodulating CCDs for the SPHERE / ZIMPOL imaging polarimeter,” vol. 8446, pp. 1–13, doi: 10.1117/12.925886.

[45] O. Kochukhov, V. Makaganiuk, and N. Piskunov, “Least-squares deconvolution of the stellar intensity and polarization spectra,” vol. 5, pp. 1–14, 2010.

[46] W. B. Sparks *et al.*, “Circular polarization in scattered light as a possible biomarker,” *J. Quant. Spectrosc. Radiat. Transf.*, vol. 110, no. 14–16, pp. 1771–1779, 2009, doi: 10.1016/j.jqsrt.2009.02.028.

[47] T. Novikova, A. Pierangelo, A. De Martino, A. Benali, and P. Validire, “Polarimetric imaging for cancer diagnosis and staging,” no. October, pp. 26–33, 2012.

[48] S. L. Jacques, “Optical properties of biological tissues: a review,” *Phys. Med. Biol.*, vol. 58, 2013, doi: 10.1088/0031-9155/58/14/5007.

[49] N. Ghosh and A. I. Vitkin, “Tissue polarimetry: concepts, challenges, applications, and outlook,” *J. Biomed. Opt.*, vol. 16, no. 11, pp. 1–30, 2011, doi: 10.1117/1.3652896.

[50] V. V. Tuchin, L. V. Wang, and D. A. Zimnyakov, *Optical Polarization in Biomedical Applications*. Springer, 2006.

[51] A. W. Dreher, K. Reiter, and R. N. Weinreb, “Spatially resolved birefringence of the retinal nerve fiber layer assessed with a retinal laser ellipsometer,” vol. 31, no. 19, pp. 0–5, 1992.

[52] S. Alali and A. Vitkin, “Polarized light imaging in biomedicine : emerging Mueller matrix methodologies for bulk tissue assessment Polarized light imaging in biomedicine : emerging Mueller matrix methodologies for,” *J. Biomed. Opt.*, vol. 20, no. 6, 2015, doi: 10.1117/1.JBO.20.6.061104.

[53] J. S. Baba, J. Chung, A. H. Delaughter, B. D. Cameron, and G. L. Cote, “Development and calibration of an automated Mueller matrix polarization imaging system,” vol. 7, no. 3, pp. 341–349, 2002, doi: 10.1117/1.1486248.

[54] A. Pierangelo *et al.*, “Polarimetric imaging of uterine cervix : a case study,” vol. 21, no. 12, pp. 281–289, 2013, doi: 10.1364/OE.21.014120.

[55] S. Manhas *et al.*, “Demonstration of full 4 × 4 Mueller polarimetry through an optical fiber for endoscopic applications,” vol. 23, no. 3, pp. 3038–3045, 2015, doi: 10.1364/OE.23.003047.

[56] K. M. Twietmeyer, R. A. Chipman, A. E. Elsner, Y. Zhao, and D. VanNasdale, “Mueller matrix retinal imager with optimized polarization conditions,” *Opt. Express*, vol. 16, no. 26, p.

21339, 2008, doi: 10.1364/oe.16.021339.

[57] L. A. Nafie, “Journal of MOLECULAR STRUCTURE ELSEVIER,” vol. 347, pp. 83–100, 1995.

[58] B. Ranjbar and P. Gill, “Circular Dichroism Techniques : Biomolecular and Nanostructural Analyses- A Review,” pp. 101–120, 2009, doi: 10.1111/j.1747-0285.2009.00847.x.

[59] O. Arteaga *et al.*, “Relation between 2D / 3D chirality and the appearance of chiroptical effects in real nanostructures Abstract :,” *Opt. Express*, vol. 24, no. 3, pp. 783–787, 2016, doi: 10.1364/OE.24.002242.

[60] C. Bustamante, “Circular Intensity Differential Scattering of Chiral Molecules,” *PhD Thesis*, 1980.

[61] L. A. Nguyen, H. He, and C. Pham-Huy, “Chiral Drugs: An Overview,” *Int. J. Biomed. Sci.*, vol. 2, no. 2, pp. 85–100, 2006.

[62] K. Maeshima, S. Ide, and M. Babokhov, “Dynamic chromatin organization without the 30-nm fiber,” *Curr. Opin. Cell Biol.*, vol. 58, pp. 95–104, 2019, doi: https://doi.org/10.1016/j.ceb.2019.02.003.

[63] B. van Steensel, “Chromatin: constructing the big picture,” *EMBO J.*, vol. 30, no. 10, pp. 1885–1895, May 2011, doi: 10.1038/emboj.2011.135.

[64] J. Gall, “Chromosome fibers from an interphase nucleus,” *Science (80-.).*, vol. 139, no. 3550, pp. 120–121, 1963, doi: 10.1126/science.139.3550.120.

[65] K. Van Holde and J. Zlatanova, “Chromatin higher order structure: Chasing a mirage?,” *J. Biol. Chem.*, vol. 270, no. 15, pp. 8373–8376, Apr. 1995, doi: 10.1074/jbc.270.15.8373.

[66] A. Jansen and K. J. Verstrepen, “Nucleosome Positioning in Saccharomyces cerevisiae,” *Microbiol. Mol. Biol. Rev.*, vol. 75, no. 2, pp. 301–320, 2011, doi: 10.1128/MMBR.00046-10.

[67] S. A. Grigoryev and C. L. Woodcock, “Chromatin organization — The 30nm fiber,” *Exp. Cell Res.*, vol. 318, no. 12, pp. 1448–1455, 2012, doi: https://doi.org/10.1016/j.yexcr.2012.02.014.

[68] Y. Nishino *et al.*, “Human mitotic chromosomes consist predominantly of irregularly folded nucleosome fibres without a 30-nm chromatin structure,” *EMBO J.*, vol. 31, no. 7, pp. 1644–1653, Apr. 2012, doi: https://doi.org/10.1038/emboj.2012.35.

[69] F. Thoma, K. Th., and A. Klug, “Involvement of histone H1 in the organization of the nucleosome and of the salt-dependent superstructures of chromatin,” *J. Cell Biol.*, vol. 83, no. 2 I, pp. 403–427, 1979, doi: 10.1083/jcb.83.2.403.

[70] G. Felsenfeld and M. Groudine, “Controlling the double helix,” *Nature*, vol. 421, no. 6921, pp. 448–453, 2003, doi: 10.1038/nature01411.

[71] P. F. Mullaney and P. N. Dean, “The Small-Angle Light Scattering of Biological Cells: Theoretical Considerations,” *Biophys. J.*, vol. 10, no. 8, pp. 764–772, 1970, doi:

https://doi.org/10.1016/S0006-3495(70)86334-2.

[72] P. Chýlek, V. Ramaswamy, and V. Srivastava, “Albedo of soot-contaminated snow,” *J. Geophys. Res. Ocean.*, vol. 88, no. C15, pp. 10837–10843, 1983, doi: https://doi.org/10.1029/JC088iC15p10837.

[73] C. Goddeeris, F. Cuppo, H. Reynaers, W. G. Bouwman, and G. Van den Mooter, “Light scattering measurements on microemulsions: Estimation of droplet sizes,” *Int. J. Pharm.*, vol. 312, no. 1, pp. 187–195, 2006, doi: https://doi.org/10.1016/j.ijpharm.2006.01.037.

[74] M. Schmitz, T. Rothe, and A. Kienle, “Comparison between spectral resolved scattering microscopy and collimated transmission measurements,” in *Advanced Microscopy Techniques II*, 2011, vol. 8086, pp. 110–115, doi: 10.1117/12.889644.

[75] T. Rothe, M. Schmitz, and A. Kienle, “Angular and spectrally resolved investigation of single particles by darkfield scattering microscopy,” *J. Biomed. Opt.*, vol. 17, no. 11, pp. 1–8, 2012, doi: 10.1117/1.JBO.17.11.117006.

[76] K. Fischer and M. Schmidt, “Pitfalls and novel applications of particle sizing by dynamic light scattering,” *Biomaterials*, vol. 98, pp. 79–91, 2016, doi: https://doi.org/10.1016/j.biomaterials.2016.05.003.

[77] N. C. Santos and M. A. Castanho, “Teaching light scattering spectroscopy: the dimension and shape of tobacco mosaic virus,” *Biophys. J.*, vol. 71, no. 3, pp. 1641–1650, 1996, doi: https://doi.org/10.1016/S0006-3495(96)79369-4.

[78] A. I. Konokhova, A. A. Gelash, M. A. Yurkin, A. V Chernyshev, and V. P. Maltsev, “High-precision characterization of individual E. coli cell morphology by scanning flow cytometry,” *Cytom. Part A*, vol. 83A, no. 6, pp. 568–575, 2013, doi: https://doi.org/10.1002/cyto.a.22294.

[79] Y. Jo *et al.*, “Angle-resolved light scattering of individual rod-shaped bacteria based on Fourier transform light scattering,” *Sci. Rep.*, vol. 4, no. 1, p. 5090, 2014, doi: 10.1038/srep05090.

[80] Y. Jo, J. Jung, M. Kim, H. Park, S.-J. Kang, and Y. Park, “Label-free identification of individual bacteria using Fourier transform light scattering,” *Opt. Express*, vol. 23, no. 12, pp. 15792–15805, Jun. 2015, doi: 10.1364/OE.23.015792.

[81] L. J. N. Lew, M. V Ting, and T. C. Preston, “Determining the size and refractive index of homogeneous spherical aerosol particles using Mie resonance spectroscopy,” *Appl. Opt.*, vol. 57, no. 16, pp. 4601–4609, Jun. 2018, doi: 10.1364/AO.57.004601.

[82] J. G. J. Peelen and R. Metselaar, “Light scattering by pores in polycrystalline materials: Transmission properties of alumina,” *J. Appl. Phys.*, vol. 45, no. 1, pp. 216–220, 1974, doi: 10.1063/1.1662961.

[83] F. A. Otero, G. L. Frontini, and G. E. Eliçabe, “Evaluation of light scattering models to characterize concentrated polymer particles embedded in a solid polymer matrix,” *J.*

Polym. Sci. Part B Polym. Phys., vol. 48, no. 9, pp. 958–963, 2010, doi: https://doi.org/10.1002/polb.21983.

[84] B. S. Luk'yanchuk, N. V Voshchinnikov, R. Paniagua-Domínguez, and A. I. Kuznetsov, "Optimum Forward Light Scattering by Spherical and Spheroidal Dielectric Nanoparticles with High Refractive Index," *ACS Photonics*, vol. 2, no. 7, pp. 993–999, Jul. 2015, doi: 10.1021/acsphotonics.5b00261.

[85] K. Rebner, E. Ostertag, and R. W. Kessler, "Hyperspectral backscatter imaging: a label-free approach to cytogenetics," *Anal. Bioanal. Chem.*, vol. 408, no. 21, pp. 5701–5709, 2016, doi: 10.1007/s00216-016-9670-1.

[86] D. Müller, D. Geiger, J. Stark, and A. Kienle, "Angle-resolved light scattering of single human chromosomes: experiments and simulations," *Phys. Med. Biol.*, vol. 64, no. 4, p. 45016, Feb. 2019, doi: 10.1088/1361-6560/aafd6f.

[87] W. S. Bickel and M. E. Stafford, "Polarized light scattering from biological systems: A technique for cell differentiation," *J. Biol. Phys.*, vol. 9, no. 2, pp. 53–66, 1981, doi: 10.1007/BF01987283.

[88] L. T. Perelman *et al.*, "Observation of Periodic Fine Structure in Reflectance from Biological Tissue: A New Technique for Measuring Nuclear Size Distribution," *Phys. Rev. Lett.*, vol. 80, no. 3, pp. 627–630, Jan. 1998, doi: 10.1103/PhysRevLett.80.627.

[89] A. Wax, C. Yang, V. Backman, M. Kalashnikov, R. R. Dasari, and M. S. Feld, "Determination of particle size by using the angular distribution of backscattered light as measured with low-coherence interferometry," *J. Opt. Soc. Am. A*, vol. 19, no. 4, pp. 737–744, Apr. 2002, doi: 10.1364/JOSAA.19.000737.

[90] R. A. Drezek *et al.*, "Light scattering from cervical cells throughout neoplastic progression: influence of nuclear morphology, DNA content, and chromatin texture," *J. Biomed. Opt.*, vol. 8, no. 1, pp. 7–16, 2003, doi: 10.1117/1.1528950.

[91] J. Stark, T. Rothe, S. Kieß, S. Simon, and A. Kienle, "Light scattering microscopy measurements of single nuclei compared with GPU-accelerated FDTD simulations," *Phys. Med. Biol.*, vol. 61, no. 7, pp. 2749–2761, 2016, doi: 10.1088/0031-9155/61/7/2749.

[92] H. Ding, Z. Wang, F. Nguyen, S. A. Boppart, and G. Popescu, "Fourier Transform Light Scattering of Inhomogeneous and Dynamic Structures," *Phys. Rev. Lett.*, vol. 101, no. 23, p. 238102, Dec. 2008, doi: 10.1103/PhysRevLett.101.238102.

[93] B. P. Dorman and M. F. Maestre, "Experimental Differential Light-Scattering Correction to the Circular Dichroism of Light-Scattering Dichroism of Bacteriophage T2," *Proc. Natl. Acad. Sci.*, vol. 70, no. 1, pp. 255–259, 2014.

[94] C. Bustamante, I. Tinoco, and M. F. Maestre, "Circular differential scattering can be an important part of the circular dichroism of macromolecules.," *Proc. Natl. Acad. Sci. U. S. A.*, 1983, doi: 10.1073/pnas.80.12.3568.

[95] W. P. Van De Merwe, Z.-Z. Li, B. V. Bronk, and J. Czege, “Polarized Light Scattering for Rapid Observation of Bacterial Size Changes,” *Biophys. J.*, vol. 73, no. July, pp. 500–506, 1997, doi: 10.1016/S0006-3495(97)78088-3.

[96] K. S. A. M. Wells, D. A. Beach, D. Keller, and W. E. T. Al, “An Analysis of Circular Intensity Differential Scattering Measurements : Studies on the Sperm Cell of Eledone cirrhosa,” *Biopolymers*, vol. 25, pp. 2043–2064, 1986.

[97] I. Tinoco, M. Maestre, C. Bustamante, and D. Keller, “Use of circularly polarized light to study biological macromolecules,” *Pure Appl. Chem.*, vol. 56, pp. 1423–1428, 1984.

[98] A. Diaspro, M. Bertolotto, L. Vergani, and C. Nicolini, “Polarized light scattering of nucleosomes and polynucleosomes-in situ and in vitro studies,” *IEEE Trans. Biomed. Eng.*, vol. 38, no. 7, pp. 670–678, Jul. 1991, doi: 10.1109/10.83568.

[99] K. C. Hadley and I. A. Vitkin, “Optical rotation and linear and circular depolarization rates in diffusively scattered light from chiral, racemic and achiral turbid media,” *J. Biomed. Opt.*, vol. 7, no. 3, pp. 291–299, 2002, doi: 10.1117/1.1483880.

[100] O. Arteaga *et al.*, “Flow Effects in Supramolecular Chirality,” *Isr. J. Chem.*, vol. 51, no. 10, pp. 1007–1016, 2011, doi: https://doi.org/10.1002/ijch.201100043.

[101] A. Sharma, A. Campbell, J. Leoni, Y. T. Cheng, M. Müllner, and G. Lakhwani, “Circular Intensity Differential Scattering Reveals the Internal Structure of Polymer Fibrils,” *J. Phys. Chem. Lett.*, vol. 10, no. 24, pp. 7547–7553, 2019, doi: 10.1021/acs.jpclett.9b02993.

[102] C. Bustamante, I. Tinoco, M. F. Maestre, C. Bustamante, I. Tinoco, and M. F. Maestre, “Circular intensity differential scattering of light . IV . Randomly oriented species,” vol. 3440, 1982, doi: 10.1063/1.443442.

[103] H. Devoe, “Optical Properties of Molecular Aggregates. II. Classical Theory of the Refraction, Absorption, and Optical Activity of Solutions and Crystals,” vol. 3199, 1965, doi: 10.1063/1.1697294.

[104] M. F. Maestre, C. J. Bustamante, P. A. Snyder, E. M. Rowe, and R. W. C. Hansen, “Circular intensity differential scattering measurements in the soft x-ray region of the spectrum (~16 EV to 500 EV),” in *Production and Analysis of Polarized X Rays*, 1991, vol. 1548, pp. 179–187, doi: 10.1117/12.50583.

[105] D. B. Shapiro, M. F. Maestre, W. M. Mcclain, P. G. Hull, and Y. Shi, “Determination of the average orientation of DNA in the octopus sperm Eledone cirrhossa through polarized light scattering,” vol. 33, no. 24, pp. 5733–5744, 1994.

[106] C. Bustamante, M. F. Maestre, D. Keller, I. T. Jr, C. Bustamante, and M. F. Maestre, “Differential scattering (CIDS) of circularly polarized light by dense particles,” vol. 4817, no. 1984, 1996, doi: 10.1063/1.446502.

[107] A. S. Belmont, “Differential Scattering of Circularly Polarized Light by Chromatin Modeled as a Helical Array of Dielectric Ellipsoids within the Born Approximation,” vol. 24, 1985.

[108] M. Kim and C. Bustamante, “Differential polarization imaging IV. Images In higher Born approximations,” vol. 59, no. June, pp. 1171–1182, 1991.

[109] A. S. Belmont, S. Zietz, and C. Nicolini, “Differential scattering of circularly polarized light by chromatin modeled as a helical array of dielectric ellipsoids within the born approximation,” *Biopolymers*, vol. 24, no. 7, pp. 1301–1321, 1985, doi: https://doi.org/10.1002/bip.360240716.

[110] A. Kaczmarczyk, H. Meng1, O. Ordu, J. van Noort, and N. H. Dekker, “Chromatin fibers stabilize nucleosomes under torsional stress,” *Nat. Commun.*, vol. 11, no. 126, pp. 1–12, 2020, doi: 10.1038/s41467-019-13891-y.

[111] B. T. Draine and P. J. Flatau, “Discrete-Dipole Approximation For Scattering Calculations,” *J. Opt. Soc. Am. A*, vol. 11, no. 4, pp. 1491–1499, Apr. 1994, doi: 10.1364/JOSAA.11.001491.

[112] M. A. Yurkin and A. G. Hoekstra, “The discrete dipole approximation: An overview and recent developments,” *J. Quant. Spectrosc. Radiat. Transf.*, vol. 106, no. 1, pp. 558–589, 2007, doi: https://doi.org/10.1016/j.jqsrt.2007.01.034.

[113] R. Schuh, “Arbitrary particle shape modeling in ddscat and validation of simulation results,” in *Proceedings of the DDA-Workshop*, 2007, pp. 22–24.

[114] M. A. Yurkin and A. G. Hoekstra, “The discrete-dipole-approximation code ADDA: Capabilities and known limitations,” *J. Quant. Spectrosc. Radiat. Transf.*, vol. 112, no. 13, pp. 2234–2247, 2011, doi: https://doi.org/10.1016/j.jqsrt.2011.01.031.

[115] A. Fritz and C. Bustamante, *Applications of Circularly Polarized Radiation Using Synchrotron and Ordinary Sources*. Springer, 1985.

[116] C. F. Bohren and D. R. Huffman, *Absorption and scattering of light by small particles*. Wiley Interscience, 1983.

[117] A. Penttilä *et al.*, “Comparison between discrete dipole implementations and exact techniques,” *J. Quant. Spectrosc. Radiat. Transf.*, vol. 106, no. 1, pp. 417–436, 2007, doi: https://doi.org/10.1016/j.jqsrt.2007.01.026.

[118] A. I. Konokhova *et al.*, “Light-scattering flow cytometry for identification and characterization of blood microparticles,” *J. Biomed. Opt.*, vol. 17, no. 5, pp. 1–9, 2012, doi: 10.1117/1.JBO.17.5.057006.

[119] P. K. Jain, K. S. Lee, I. H. El-Sayed, and M. A. El-Sayed, “Calculated Absorption and Scattering Properties of Gold Nanoparticles of Different Size, Shape, and Composition: Applications in Biological Imaging and Biomedicine,” *J. Phys. Chem. B*, vol. 110, no. 14, pp. 7238–7248, 2006, doi: 10.1021/jp057170o.

[120] P. K. Jain and M. A. El-Sayed, “Plasmonic coupling in noble metal nanostructures,” *Chem. Phys. Lett.*, vol. 487, no. 4, pp. 153–164, 2010, doi: https://doi.org/10.1016/j.cplett.2010.01.062.

[121] S. Yoo and Q.-H. Park, “Enhancement of Chiroptical Signals by Circular Differential Mie Scattering of Nanoparticles,” *Sci. Rep.*, vol. 5, no. 1, p. 14463, 2015, doi: 10.1038/srep14463.

[122] M. Maestre, G. Salzman, R. Tobey, and C. Bustamante, “Circular Dichroism Studies on Single Chinese Hamster Cells,” *Biochemistry*, vol. 24, no. 19, pp. 5152–5157, Sep. 1985, doi: 10.1021/bi00340a600.

[123] A. S. Schneider, M. J. Schneider, and K. Rosenheck, “Optical activity of biological membranes: scattering effects and protein conformation,” *Proc. Natl. Acad. Sci. U. S. A.*, vol. 66, no. 3, pp. 793–798, Jul. 1970, doi: 10.1073/pnas.66.3.793.

[124] C. Reich, M. F. Maestre, S. Edmondson, and D. M. Gray, “Circular dichroism and fluorescence-detected circular dichroism of deoxyribonucleic acid and poly[d(A-C).cntdot.d(G-T)] in ethanolic solutions: a new method for estimating circular intensity differential scattering,” *Biochemistry*, vol. 19, no. 23, pp. 5208–5213, Nov. 1980, doi: 10.1021/bi00564a009.

[125] P. H. Schippers and H. P. J. M. Dekkers, “Direct determination of absolute circular dichroism data and calibration of commercial instruments,” *Anal. Chem.*, vol. 53, no. 6, pp. 778–782, May 1981, doi: 10.1021/ac00229a008.

[126] A. Le Gratiet, R. Marongiu, and A. Diaspro, “Circular Intensity Differential Scattering for Label-Free Chromatin Characterization: A Review for Optical Microscopy,” *Polymers (Basel).*, vol. 12, no. 10, 2020, doi: 10.3390/polym12102428.

[127] G. C. Salzman, J. K. Griffith, and C. T. Gregg, “Rapid identification of microorganisms by circular-intensity differential scattering.,” *Appl. Environ. Microbiol.*, vol. 44, no. 5, pp. 1081–1085, 1982, [Online]. Available: https://aem.asm.org/content/44/5/1081.

[128] B. V Bronk, D. Stephen, J. Czege, and W. P. Van, “Measuring Diameters of Rod-Shaped Bacteria in Vivo with Polarized Light Scattering,” *Biophys. J.*, vol. 69, no. September, pp. 1170–1177, 1995, doi: 10.1016/S0006-3495(95)79991-X.

[129] L. Finzi, C. Bustamante, G. Garab, and C.-B. Juang, “Direct Observation of Large Chiral Domains in Chloroplast Thylakoid Membranes by Differential Polarization Microscopy,” *Proc. Natl. Acad. Sci. U. S. A.*, vol. 86, no. 22, pp. 8748–8752, 1989, [Online]. Available: http://www.jstor.org/stable/34955.

[130] D. Keller and C. Bustamante, “Theory of the interaction of light with large inhomogeneous molecular aggregates . II . Psitype circular dichroism,” *J. Chem. Phys.*, vol. 84, no. 6, pp. 2972–2980, 1986, doi: 10.1063/1.450278.

[131] M. Kim, L. Ulibarri, D. Keller, M. F. Maestre, and C. Bustamante, “The psi-type circular dichroism of large molecular aggregates. III. Calculations,” *J. Chem. Phys.*, vol. 84, no. 6, pp. 2981–2989, Mar. 1986, doi: 10.1063/1.450279.

[132] G. Garab, S. Wells, L. Finzi, and C. Bustamante, “Helically organized macroaggregates of pigment-protein complexes in chloroplasts: evidence from circular intensity differential

scattering," *Biochemistry*, vol. 27, no. 16, pp. 5839–5843, Aug. 1988, doi: 10.1021/bi00416a003.

[133] C. H. L. Patty *et al.*, "Circular Spectropolarimetric Sensing of Vegetation in the Field: Possibilities for the Remote Detection of Extraterrestrial Life," *Astrobiology*, vol. 19, no. 10, pp. 1221–1229, Aug. 2019, doi: 10.1089/ast.2019.2050.

[134] F. Livolant and A. Leforestier, "Condensed phases of DNA: Structures and phase transitions," *Prog. Polym. Sci.*, vol. 21, no. 6, pp. 1115–1164, 1996, doi: https://doi.org/10.1016/S0079-6700(96)00016-0.

[135] C. Nicolini, L. Vergani, A. Diaspro, and P. Scelza, "Native chromatin and damage induced by nuclease," *Biochem. Biophys. Res. Commun.*, vol. 155, no. 3, pp. 1396–1403, 1988, doi: https://doi.org/10.1016/S0006-291X(88)81296-8.

[136] A. Diaspro and C. A. Nicolini, "Circular intensity differential scattering and chromatin-DNA structure," *Cell Biophys.*, vol. 10, no. 1, pp. 45–60, 1987, doi: 10.1007/BF02797073.

[137] Y. L. Kim *et al.*, "Comprehensive description of light scattering by simultaneous measurement of angular, spectral, and polarization dependence for characterization of tissue macroachitecture in normal and precancerous states," in *Diagnostic Optical Spectroscopy in Biomedicine II*, 2003, vol. 5141, pp. 95–105, doi: 10.1117/12.500880.

[138] D. Keller, C. Bustamante, M. F. Maestre, and I. Tinoco, "Imaging of optically active biological structures by use of circularly polarized light," *Proc. Natl. Acad. Sci.*, vol. 82, no. 2, pp. 401–405, 1985, doi: 10.1073/pnas.82.2.401.

[139] M. Kim, D. Keller, and C. Bustamante, "DIFFERENTIAL POLARIZATION IMAGING I . Theory," *Biophys. J.*, vol. 52, no. 6, pp. 911–927, doi: 10.1016/S0006-3495(87)83285-X.

[140] M. Kim, C. Keller, and C. Bustamante, *Differential Polarization Imaging I: Theory and Applications*. 1987.

[141] M. Kim, L. Ulibarri, and C. Bustamante, "Differential Polarization Imaging. II. Symmetry Properties and Calculations," *Biophys. J.*, vol. 52, pp. 929–946, 1987.

[142] D. A. Beach, C. Bustamante, K. S. A. M. Wells, and K. M. Foucar, "DIFFERENTIAL POLARIZATION IMAGING III . Theory Confirmation . Patterns of Polymerization of Hemoglobin S in Red Blood Sickle Cells," *Biophys. J.*, vol. 53, no. 3, pp. 449–456, 1988, doi: 10.1016/S0006-3495(88)83121-7.

[143] R. Oldenbourg and P. Török, "Point-spread functions of a polarizing microscope equipped with high-numerical-aperture lenses," *Appl. Opt.*, vol. 39, no. 34, pp. 6325–6331, Dec. 2000, doi: 10.1364/AO.39.006325.

[144] L. Finzi, L. Ulibarri, and C. Bustamante, "Differential polarization imaging V. Numerical aperture effects and the contribution of preferential scattering and absorption to the circular dichroism images," vol. 59, no. June, pp. 1183–1193, 1991.

[145] W. C. Mickols, C. Bustamante, M. F. Maestre, I. Tinoco, and S. H. Embury, "Differential

Polarization Microscopy: A New Imaging Technique," *Bio/Technology*, vol. 3, no. 8, pp. 711–714, 1985, doi: 10.1038/nbt0885-711.

[146] D. A. Beach, K. S. Wells, F. Husher, and C. Bustamante, "Differential polarization microscope using an image dissector camera and phase-lock detection," *Rev. Sci. Instrum.*, vol. 58, no. 11, pp. 1987–1995, Nov. 1987, doi: 10.1063/1.1139505.

[147] W. Mickols and M. F. Maestre, "Scanning differential polarization microscope: Its use to image linear and circular differential scattering," *Rev. Sci. Instrum.*, vol. 59, no. 6, pp. 867–872, Jun. 1988, doi: 10.1063/1.1139795.

[148] W. Mickols, M. F. Maestre, and I. Tinoco, "Differential polarization microscopy of changes in structure in spermatocyte nuclei," *Nature*, vol. 328, no. 6129, pp. 452–454, 1987, doi: 10.1038/328452a0.

[149] "Direct observation of large chiral domains in chloroplast thylakoid membranes by differential polarization microscopy," *Proc. Natl. Acad. Sci.*, vol. 87, no. 3, p. 1257, 1990, doi: 10.1073/pnas.87.3.1257a.

[150] V. K. Gupta and J. A. Kornfield, "Polarization modulation laser scanning microscopy: A powerful tool to image molecular orientation and order," *Rev. Sci. Instrum.*, vol. 65, no. 9, pp. 2823–2828, 1994, doi: 10.1063/1.1144622.

[151] M. Kim, L. Ulibarri, and C. Bustamante, "DIFFERENTIAL POLARIZATION IMAGING II . Symmetry Properties and Calculations," *Biophys. J.*, vol. 52, no. 6, pp. 929–946, doi: 10.1016/S0006-3495(87)83286-1.

[152] W. Mickols, M. F. Maestre, I. Tinoco Jr, and S. H. Embury, "Visualization of oriented hemoglobin S in individual erythrocytes by differential extinction of polarized light," *Proc. Natl. Acad. Sci. U. S. A.*, vol. 82, no. 19, pp. 6527–6531, Oct. 1985, doi: 10.1073/pnas.82.19.6527.

[153] C. Juang, L. Finzi, and C. J. Bustamante, "Design and application of a computer-controlled confocal scanning differential polarization microscope," *Rev. Sci. Instrum.*, vol. 59, no. 11, pp. 2399–2408, Nov. 1988, doi: 10.1063/1.1139918.

[154] T. Yamada, H. Onuki, M. Yuri, and S. Ishizaka, "Microscopic Imaging of Circular Dichroism Using a Polarizing Undulator," *Jpn. J. Appl. Phys.*, vol. 39, no. Part 1, No. 1, pp. 310–315, Jan. 2000, doi: 10.1143/jjap.39.310.

[155] J. C. Sutherland, "Simultaneous measurement of circular dichroism and fluorescence polarization anisotropy," in *Clinical Diagnostic Systems: Technologies and Instrumentation*, 2002, vol. 4625, pp. 126–136, doi: 10.1117/12.469782.

[156] G. Steinbach, I. Pomozi, O. Zsiros, A. Páy, G. V Horváth, and G. Garab, "Imaging fluorescence detected linear dichroism of plant cell walls in laser scanning confocal microscope," *Cytom. Part A*, vol. 73A, no. 3, pp. 202–208, 2008, doi: https://doi.org/10.1002/cyto.a.20517.

[157] S. B. Mehta, M. Shribak, and R. Oldenbourg, “Polarized light imaging of birefringence and diattenuation at high resolution and high sensitivity,” *J. Opt.*, vol. 15, no. 9, p. 94007, Sep. 2013, doi: 10.1088/2040-8978/15/9/094007.

[158] J. H. Freudenthal, E. Hollis, and B. Kahr, “Imaging chiroptical artifacts,” *Chirality*, vol. 21, no. 1E, pp. E20–E27, 2009, doi: https://doi.org/10.1002/chir.20768.

[159] G. Garab *et al.*, “Alignment of biological microparticles by a polarized laser beam,” *Eur. Biophys. J.*, vol. 34, no. 4, pp. 335–343, 2005, doi: 10.1007/s00249-004-0454-8.

[160] F. Tantussi *et al.*, “Linear and circular dichroism in porphyrin J-aggregates probed by polarization modulated scanning near-field optical microscopy,” *Nanoscale*, vol. 6, no. 18, pp. 10874–10878, 2014, doi: 10.1039/C4NR00918E.

[161] C. H. L. Patty *et al.*, “Imaging linear and circular polarization features in leaves with complete Mueller matrix polarimetry,” *Biochim. Biophys. Acta - Gen. Subj.*, vol. 1862, no. 6, pp. 1350–1363, 2018, doi: https://doi.org/10.1016/j.bbagen.2018.03.005.

[162] J. Schindelin *et al.*, “Fiji: an open-source platform for biological-image analysis,” *Nat. Methods*, vol. 9, no. 7, pp. 676–682, 2012, doi: 10.1038/nmeth.2019.

[163] F. Chen, P. W. Tillberg, and E. S. Boyden, “Expansion microscopy,” *Science (80-.).*, vol. 347, no. 6221, pp. 543–548, 2015, doi: 10.1126/science.1260088.

[164] T. J. Chozinski *et al.*, “Expansion microscopy with conventional antibodies and fluorescent proteins,” *Nat. Methods*, vol. 13, no. 6, pp. 485–488, 2016, doi: 10.1038/nmeth.3833.

[165] R. Gao, S. M. Asano, and E. S. Boyden, “Q&A: Expansion microscopy,” *BMC Biol.*, vol. 15, no. 1, p. 50, 2017, doi: 10.1186/s12915-017-0393-3.

[166] L. Pesce, M. Cozzolino, L. Lanzanò, A. Diaspro, and P. Bianchini, “Measuring expansion from macro- to nanoscale using NPC as intrinsic reporter,” *J. Biophotonics*, vol. 12, no. 8, p. e201900018, 2019, doi: https://doi.org/10.1002/jbio.201900018.

[167] J.-B. Chang *et al.*, “Iterative expansion microscopy,” *Nat. Methods*, vol. 14, no. 6, pp. 593–599, 2017, doi: 10.1038/nmeth.4261.

[168] D. Gambarotto *et al.*, “Imaging cellular ultrastructures using expansion microscopy (U-ExM),” *Nat. Methods*, vol. 16, no. 1, pp. 71–74, 2019, doi: 10.1038/s41592-018-0238-1.

[169] J. B. Bawley, *Handbook Of Biological Confocal Microscopy*. Springer, 2006.

[170] M. Gao *et al.*, “Expansion Stimulated Emission Depletion Microscopy (ExSTED),” *ACS Nano*, vol. 12, no. 5, pp. 4178–4185, 2018, doi: 10.1021/acsnano.8b00776.

[171] Z. Tong, P. Beuzer, Q. Ye, J. Axelrod, Z. Hong, and H. Cang, “Ex-STORM: Expansion Single Molecule Super-resolution Microscopy,” *bioRxiv*, 2016, doi: 10.1101/049403.

[172] A. R. Halpern, G. C. M. Alas, T. J. Chozinski, A. R. Paredez, and J. C. Vaughan, “Hybrid Structured Illumination Expansion Microscopy Reveals Microbial Cytoskeleton Organization,” *ACS Nano*, vol. 11, no. 12, pp. 12677–12686, Dec. 2017, doi:

10.1021/acsnano.7b07200.

[173] C. K. Cahoon *et al.*, “Superresolution expansion microscopy reveals the three-dimensional organization of the Drosophila synaptonemal complex,” *Proc. Natl. Acad. Sci.*, vol. 114, no. 33, pp. E6857--E6866, 2017, doi: 10.1073/pnas.1705623114.

[174] L. Pesce, M. Cozzolino, L. Lanzanò, A. Diaspro, and P. Bianchini, “Measuring expansion from macro- to nanoscale using NPC as intrinsic reporter,” no. January, pp. 1–9, 2019, doi: 10.1002/jbio.201900018.

[175] A. Le Gratiet *et al.*, “Circular intensity differential scattering (CIDS) scanning microscopy to image chromatin-DNA nuclear organization,” *OSA Contin.*, vol. 1, no. 3, pp. 1068–1078, Nov. 2018, doi: 10.1364/OSAC.1.001068.

[176] R. Marongiu, A. Le Gratiet, L. Pesce, P. Bianchini, and A. Diaspro, “ExCIDS: a combined approach coupling Expansion Microscopy (ExM) and Circular Intensity Differential Scattering (CIDS) for chromatin-DNA imaging,” *OSA Contin.*, vol. 3, no. 7, pp. 1770–1780, Jul. 2020, doi: 10.1364/OSAC.388868.

[177] J. Xu and Y. Liu, “A guide to visualizing the spatial epigenome with super-resolution microscopy,” *FEBS J.*, vol. 286, no. 16, pp. 3095–3109, 2019, doi: https://doi.org/10.1111/febs.14938.

Communications and Publications

1. Communications

- 63rd Biophysical Society Annual Meeting – Baltimore, Maryland (USA), 2-6 March 2019

  Poster: Label-free Chromatin-DNA imaging by circular polarized light scattering scanning microscopy, **R. Marongiu**, A. Le Gratiet, L. Pesce, M. Oneto, G. Zanini, P. Bianchini, A. Diaspro – **Poster Competition winner**

- 64th Biophysical Society Annual Meeting – San Diego, California (USA), 15-19 February 2020

  Poster: Polarization-Resolved Light Scattering Spectroscopy (pLSS) to study chromatin-DNA organization, **R. Marongiu**, A. Le Gratiet, M. W. Ashraf, A. Diaspro

- Italian Conference on Optics and Photonics (ICOP) 2020 – Online, 8-11 September 2020

  Oral: A Combined Expansion Microscopy And CIDS Approach To Chromatin DNA Study, **R. Marongiu**, A. Le Gratiet, L. Pesce, P. Bianchini, A. Diaspro

- 106° Congresso Nazionale della Società Italiana di Fisica (SIF) – Online, 14-18 September 2020

  Oral: ExCIDS: improvement of CIDS imaging of DNA organization by Expansion Microscopy coupling, **R. Marongiu**, A. Le Gratiet, L. Pesce, P. Bianchini, A. Diaspro

2. Publications

- "Circular intensity differential scattering (CIDS) scanning microscopy to image chromatin-DNA nuclear organization" - *A. Le Gratiet, L. Pesce, M. Oneto, **R. Marongiu**, G. Zanini, P. Bianchini and A. Diaspro, OSA Continuum (2018)*

- "Zebrafish Structural Development In Mueller-Matrix Scanning Microscopy" – *A. Le Gratiet, M. d'Amora, M. Duocastella, **R. Marongiu**, A. Bendandi, S. Giordani, P. Bianchini and A. Diaspro, Scientific Reports (2019)*

- "Excids: A Combined Approach Coupling Expansion Microscopy (ExM) And Circular Intensity Differential Scattering (CIDS) For Chromatin-DNA Imaging" – ***R. Marongiu****, A. Le Gratiet, L. Pesce, P. Bianchini and A. Diaspro, OSA Continuum (2020)*
- "Circular Intensity Differential Scattering (CIDS) for label-free chromatin-DNA characterization: a review for optical microscopy", *A. Le Gratiet,* ***R. Marongiu*** *and A. Diaspro, Polymers (2020)*
- "Combined approach using circular intensity differential scattering microscopy under phasor map data analysis", A. Mohebi, A. Le Gratiet, **R. Marongiu**, F. Callegari, P. Bianchini, and A. Diaspro*, Applied Optics (2021)*
- "Phasor approach of Mueller matrix optical scanning microscopy for label-free biological tissue orientation imaging", *A. Le Gratiet, L. Lanzano,* ***R. Marongiu****, A. Bendandi, P. Bianchini, C. Sheppard, A. Diaspro,* Under Review